

Quantitative Cloud Analysis using Meteorological Satellites

Arnout J. Feijt

UNIVERSITÄT
VERBODEN
VERBODEN

11108201, 28 96.

Stellingen

behorende bij het proefschrift
Quantitative Cloud Analysis using Meteorological Satellites
29 november 2000

..the most urgent scientific problems requiring attention to determine the rate and magnitude of climate change and sea-level rise are the factors controlling the distribution of clouds and their radiative characteristics, ... (International Panel on Climate Change, 1995)

Het gebruik van ongecorrigeerde model oppervlakte-temperaturen als drempelwaarde voor wolkendetektie in satellietbeelden resulteert in een vertekend beeld van de dagelijkse gang van bedekkingsgraad. (dit proefschrift).

Een combinatie van grond- en satellietmetingen levert een betere karakterisatie van een wolkenveld, dan ieder van de meetsystemen op zich. (dit proefschrift).

De optimale representatie van het variantie-spectrum van bewolking hangt af van de atmosferische omstandigheden. (dit proefschrift).

De metingen van de nieuwe generatie geostationaire meteorologische satellieten (MSG) zullen de operationele meteorologie aanzienlijk veranderen. (dit proefschrift).

Advanced Very High Resolution Radiometer is een goed voorbeeld van een naam met beperkte houdbaarheid.

Een goede onderzoeker is niet noodzakelijkerwijs gepromoveerd.

Een gepromoveerde wetenschapper is niet noodzakelijkerwijs een goed onderzoeker.

Een gezin is meer dan de som van de individuen.

Het veranderen van de financiering van onderzoek van de vaste (eerste) geldstroom, naar voorwaardelijke geldstromen uit programma's resulteert in een onwenselijke verzwakking van de rechtspositie van beginnende onderzoekers.

Niet kiezen is ook een keuze.

AWO8201, 2896.

**Quantitative Cloud Analysis using
Meteorological Satellites**

**Kwantitatieve Analyse van Wolken met
Meteorologische Satellieten**

Arnout J. Feijt

Promotor: Dr. A. A. M. Holtslag
Hoogleraar in de meteorologie en luchtkwaliteit

Co-promotor: Dr. A.C.A.P. van Lammeren
Senior onderzoeker K.N.M.I.

0108201, 7876

Quantitative Cloud Analysis using Meteorological Satellites

Arnout J. Feijt

Proefschrift

ter verkrijging van de graad van doctor

op gezag van de rector magnificus van Wageningen Universiteit,

dr. ir. L. Speelman,

in het openbaar te verdedigen

op woensdag 29 november 2000

des namiddags te 4 uur in de Aula.

15N 904 821

ISBN 90-5808-315-2

The research described in this thesis was done at and supported by the Royal Netherlands Meteorological Institute.

Voorwoord

In mijn curriculum vitae staat beschreven dat ik na de universiteit 6 jaar in de commerciële sector gewerkt heb, voordat ik in december 1991 terugkeerde naar de wetenschap. Promotie had ik nog nooit overwogen. In een commerciële omgeving is dat namelijk niet interessant en ook niet haalbaar. Bij het KNMI werd mij echter snel duidelijk dat er in de wetenschap veel waarde aan de doctorstitel wordt gehecht. Bovendien is het KNMI een uitermate stimulerende onderzoeksomgeving, waar het streven naar promotie ook daadwerkelijk gestimuleerd wordt. Het is opmerkelijk dat zo weinig mensen ervan op de hoogte zijn, dat er uitstekende onderzoeksfaciliteiten en onderzoekers zijn. Een aantal van mijn collega's is ook deeltijd hoogleraar. De wetenschappelijke sfeer en goede faciliteiten, gecombineerd met de kennis en ervaring van operationele meteorologie vormen een goede voedingsbodem voor onderzoek. In de loop van de jaren groeide mijn onderzoeksvaardigheid en werden de eerste interessante onderzoeksresultaten gepubliceerd. Vanaf 1997 heb ik informeel over promotie gesproken met mijn collega Bert Holtslag, die toen in deeltijd hoogleraar aan de Universiteit Utrecht was. Ook Aad van Ulden, mijn directe chef, stimuleerde mijn streven naar promotie, voornamelijk door mij alle vrijheid te laten om mijn onderzoeksvaardigheden verder te ontwikkelen in het vertrouwen dat het dan wel goed zou komen. Goed gezien Aad! Het streven kreeg in oktober 1999 vaste vorm toen ik afdoende serieuze publicaties naar tijdschriften verstuurd had. Het contact met Bert Holtslag, inmiddels hoogleraar in Wageningen werd intensiever en André van Lammeren werd aangezocht als co-promotor. En uiteindelijk is dit boekje tot stand gekomen.

In de afgelopen 9 jaar heb ik met veel mensen prettig samengewerkt. Binnen het KNMI vooral met de leden van de secties Atmosferisch Onderzoek en Satelliet Data. Buiten het KNMI was er vooral veel wisselwerking met het team van de CLARA meetcampagne.

Er zijn een aantal mensen die ik met name wil noemen. Vanaf het begin was de samenwerking met André van Lammeren uitstekend. Het enige dat echt mislukte was de gezamenlijke lancering van een radiosonde voor de zoemende camera's van het televisieprogramma "Noorderlicht" tijdens CLARA. We zijn nu een aantal publicaties en meetcampagnes verder en je bent dus uitstekend op de hoogte van mijn werk. Het is derhalve logisch dat je mijn co-promotor bent. Ook met Paul de Valk heb ik veel en met veel plezier samengewerkt. Tot nu toe staan er drie publicaties in internationale vaktijdschriften op onze

naam, en dat worden er hopelijk nog wel wat meer. Het is nooit saai met Frans Debie, basismeteoroloog in De Bilt. Frans, ik heb veel van jouw eigenzinnige kijk op satelliet meteorologie geleerd. Rose Dlhopsky heeft, als geboren Amerikaanse en physicus, een aantal van mijn artikelen van taalkundige blunders ontdaan. Ik was werkelijk trots, toen ik voor de eerste keer een artikel van jouw review terugkreeg, dat niet bedekt was met in rode inkt geschreven opmerkingen. Mijn Amerikaans is behoorlijk vooruitgegaan en de ergelijke discussies onder Nederlanders over formuleringen in het Engels zijn gelukkig door jou beslecht. Verder heb ik fijn samengewerkt met Robert Koelemeijer. Ik hoop dat er na je promotie weer wat meer ruimte voor gezamenlijke projecten zal zijn. Onvergetelijk zijn natuurlijk de CLARA campagnes. De meetvluchten in wolken (en er regelmatig ook net buiten) met Gerard Kos zou ik graag overdoen. Het is erg leerzaam wolken vanuit een vliegtuig te observeren en het zou een vast onderdeel van de studie meteorologie moeten zijn. Met Harm Jonker heb ik vele boeiende discussies gehad, die mij enig inzicht hebben gegeven in de wondere wereld van het schalingsgedrag van atmosferische processen.

Natuurlijk wil ik iedereen bedanken die verwachten mag bedankt te worden. En natuurlijk ook iedereen die ik vergeten ben. Bij deze.

En dan zijn er de mensen waardoor ik de afgelopen jaren een completer mens geworden ben. In de werkkring wil ik daarbij Joop Konings noemen. Ik begrijp je keuze om voor jezelf een internet bedrijf te beginnen, maar jammer vind ik wel dat je niet meer op de afdeling bent. Natuurlijk is mijn gezin het belangrijkste. Mijn Trees, Mark, Luuk en Milou. Zonder jullie was dit boekje wellicht eerder afgekomen, maar was ik veel minder mens geweest. En dat is toch echt het allerbelangrijkste.

Het is mij een genoegen om de leden van de promotiecommissie te noemen, die het manuscript gelezen en beoordeeld hebben en (soms ver) moeten reizen om oppositie te voeren in Wageningen:

Prof. Dr. S. de Jong van de Wageningen Universiteit

Dr. W. Rossow van Goddard Institute of Space Studies

Prof. Dr. C. Simmer van de Universeit van Bonn

Dr. A. van Ulden van het Koninklijk Nederlands Meteorologisch Instituut

I am pleased to list the members of the promotion committee who read and judged the thesis and who travel (in some cases far) for the opposition in Wageningen:

Prof. Dr. S. de Jong from Wageningen University

Dr. W. Rossow from Goddard Institute for Space Studies, New York

Prof. Dr. C. Simmer from University of Bonn

Dr. A. van Ulden from Royal Netherland Meteorological Institute

Contents

1. Introduction	1
1.1. Clouds	1
1.2. Atmospheric models	4
1.3. Observations of the current climate	5
1.4. This thesis	6
2. Radiative transfer in a cloudy atmosphere	11
2.1. Atmospheric radiative transfer	11
2.1.1 Shortwave radiation	11
2.1.2 Longwave radiation	14
2.2 Cloud-radiation interactions at $0.6\mu\text{m}$	15
2.2.1 Water clouds	15
2.2.2 Ice Clouds	21
2.3 Cloud-radiation interactions at $10.8\mu\text{m}$	24
3. The AVHRR analysis environment	31
3.1 The AVHRR instrument	31
3.2 Qualitative analysis of AVHRR radiances	32
3.3 Radiative transfer calculations	35
3.3.1 Modtran	35
3.3.2 DAK	36
3.4 AVHRR retrieval of cloud properties	37
3.4.1 Cloud detection	38
3.4.2 Cloud characterization	40
4. The Meteosat analysis environment data	49
4.1 The METEOSAT instrument	51
4.2 The use of NWP surface temperatures in cloud detection from satellite	55
4.2.1. Introduction	56
4.2.2. The difference between model surface temperature and satellite apparent brightness temperature	57

4.2.3.	Measurement method	59
4.2.3.1.	Collocation	59
4.2.3.2.	Detection criteria	61
4.2.4.	Impact of the difference between T_{nwp} and T_{sat} on the detection efficiency	62
4.2.5.	Equalizing the detection efficiency throughout the day	64
4.2.6.	Interpretation	65
4.2.7.	Application in an operational setting	67
4.2.8.	Conclusions	69
4.3.	Cloud detection using Meteosat imagery and Numerical Weather Prediction model data	71
4.3.1.	Introduction	72
4.3.2.	History of cloud detection from Meteosat data	73
4.3.3.	Description of Metclock	73
4.3.3.1.	The IR-test	74
4.3.3.2.	The VIS-test	78
4.3.3.3.	Additional tests	80
4.3.4.	Validation method	81
4.3.4.1.	Detection capability and detection efficiency	81
4.3.5.	Metclock results for 1997	84
4.3.5.1.	IR test	85
4.3.5.2.	VIS test	88
4.3.5.3.	Results of total of all tests	90
4.3.6.	Discussion and conclusions	93
5.	Cloud observations from the ground and satellite	101
5.1.	Ground-based and satellite observations of cloud fields in the Netherlands.	103
5.1.1.	Introduction	104
5.1.2.	Experimental setup	105
5.1.3.	Combining ground and satellite observations	106
5.1.4.	Discussion	116
5.2.	Validation of cloud parameter retrieval methods with objective ground based measurements	117
5.2.1.	Objective ground based measurements	118
5.2.1.1.	The KNMI Cloud Detection System	118

5.2.1.2.	Clouds and Radiation measurement campaigns	119
5.2.2.	Case study 1: APRIL 26, 1996: stratocumulus	120
5.2.2.1.	Comparison with CDS data	121
5.2.2.2.	Comparison with CLARA measurements	122
5.2.2.3.	Discussion and Conclusions	125
5.2.3.	Case study 2: April 17, 1996: cirrus	127
5.2.3.1.	Comparison with CLARA data	131
5.2.3.2.	Emissivity	131
5.2.3.3.	Cloud top temperature	135
5.2.3.4.	Conclusions	136
5.3.	Concluding remarks	137
 6.	 Comparison of scaling properties from spatial and temporal distributions of clouds	 141
6.1.	Comparison of scaling parameters from spatial and temporal distributions of cloud properties	143
6.1.1.	Introduction	144
6.1.2.	Comparison of scaling parameters from spatial and temporal distributions.	145
6.1.2.1	The CLARA data set	145
6.1.2.2	AVHRR analysis	146
6.1.2.3.	Spectral analysis	146
6.1.2.4.	April 26: Stratocumulus field	148
6.1.2.5.	September 2: Cumulus field	151
6.1.3.	Linking temporal and spatial scale parameters	153
6.1.4.	Discussion	157
6.1.5.	Conclusions	158
 7.	 Conclusions and perspective	 161
	Bibliography	165
	Acronyms	177
	List of journal papers and selected reports	179
	Summary	181
	Samenvatting	183
	Curriculum vitae	185

1. Introduction

This thesis is about observations of clouds from satellite and ground based instruments. The information on the horizontal and vertical distribution of clouds is a reference for atmospheric models to be employed in operational meteorology and in atmospheric research. In this thesis, methods are presented for the analysis of measurements from the European geostationary meteorological satellite, Meteosat, and the Advanced Very High Resolution Radiometer, AVHRR on board of the NOAA polar orbiters. For a number of cases cloud field properties as observed from the ground and satellite are used to understand the cloud processes. The work presented in this thesis has applications in operational meteorology and in climate research.

1.1 Clouds

A cloud is a collection of liquid or solid water particles. The particles are generated in cooling air. Warm air can contain more water vapor than cold air. Thus, if air cools, the relative humidity rises. If the relative humidity exceeds a certain threshold value, hygroscopic aerosols start to absorb water vapor. These aerosols act as cloud condensation nuclei (CCN). The threshold value depends on the aerosol type. If the air cools further, the relative humidity rises until the air gets (super)saturated. The excess water vapor condenses on the cloud particles that grow further.

Particles smaller than about $20\mu\text{m}$ move with the ambient air. Larger particles fall and contribute to precipitation. When the air temperature is above 0°C the cloud particles are typically liquid. This occurs in the mid-latitude summer atmosphere (MLS) below 4km height (McClatchey, 1972). When the air temperature is below -40°C (above 10km height) the excess water vapor transforms to ice crystals. This process requires the presence of ice cloud condensation nuclei, which occur in much lower concentrations than water CCN. In the temperature range from 0 to -40°C clouds may consist of supercooled liquid water particles, mixed phase particles or ice particles, depending on the aerosols available and the history of the air mass. Ice crystals grow faster than liquid water drops, due to their low surface tension. Therefore, their size may range from $10\mu\text{m}$ up to several mm or even larger. Above the tropopause, about 13km in MLS, only stratospheric polar clouds occur, occasionally.

Clouds are generated in cooling air. There are a number of atmospheric processes that can cause air to cool. Here a short list is presented:

- Convection
- Large scale lifting
- Radiative cooling

A source of energy that initiates convection over land is the warming of the surface due to insolation. The sun heats the surface that transforms the radiative energy into sensible and latent heat, which warms and humidifies air at the surface. The warm humid air has a lower specific mass than the air above and, according to the law of Archimedes, the humid warm air ascends. The air bubble expands due to the lower pressure at higher altitudes and undergoes adiabatic cooling. Subsequently the relative humidity rises, until it is sufficiently high to initiate condensation. Condensation generates heat and therefore warms the air bubble, which enhances the buoyancy. This is one of the positive feedbacks in cloud processes.

Large scale lifting occurs at the boundary of cold and warm air-masses. Cold air has a higher density and thus warm air is pushed upwards and cools, which induces cloud formation. This can be either warm air that is pushed against cold air (a warm front) or cold air that is pushed against warm air (a cold front).

Radiative cooling is one of the main mechanisms that generate fog and dew during the night. The surface radiates corresponding to its temperature and thus loses energy and cools. Part of the energy deficit is compensated by radiation from the atmosphere and heat transport from lower surface layers. However, especially in cloud free conditions, the surface cools considerably during the night. Sensible heat flow cools the air at the surface boundary, the relative humidity increases until water vapor condenses and fog is generated.

The above examples show that clouds are the result of the atmospheric conditions and thus can be used as indicators of these atmospheric conditions. In meteorological practice this is the main use of cloud observations. However, the role of clouds in atmospheric processes is more complicated, because clouds also influence the atmospheric conditions by the reflection

of sunlight, the absorption and emission of thermal radiation, and the transport of water, energy and trace gases.

Clouds influence the vertical distribution of energy, especially over land. In cloud free conditions during daytime in a mid-latitude summer, the earth surface absorbs sunlight, heats up and redistributes the energy by thermal radiation and sensible and latent heat transport. The top layer of the surface, that absorbs the solar energy, is the warmest part of the temperature profile in the afternoon. During a cloudy day part of the sunlight is reflected into space and thus the amount of solar energy available to the earth-atmosphere system is reduced. This changes the temperature profile. During nighttime, when the insolation is zero, the temperature is lower in cloud free conditions than if clouds are present, due to the larger radiative cooling. Thus the surface temperature is highly dependent on the cloud cover. The sensitivity of clouds to radiation and visa-versa can be illustrated with the life cycle of fog. Radiation fog is generated during a cloud free night when the surface cools down and subsequently the lower atmospheric layer is cooled. This radiation fog is not generated if there is a cloud present over the surface, which reduces the radiative cooling. Even a high thin cirrus layer that can hardly be observed during the night, may give enough downward radiation to prevent the generation of fog at the surface. So, to correctly predict the generation of fog during the night requires correct information on (even thin cirrus) clouds.

From the above it becomes clear that accurate information on the distribution of clouds, both horizontal and vertical, is required to understand the atmospheric conditions. The cloud-radiation interactions make the description of cloud processes a critical part of atmospheric models. However, the quality of the representation of clouds in atmospheric models is currently too low to accurately model the evolution of the weather on the scale of several days (Numerical Weather Prediction models) or the evolution of climate over tens of years (Climate models).

1.2 Atmospheric models

Even in state of the art atmospheric models the representation of clouds is poor. There are two main reasons for this. The first reason is that cloud processes are complicated and act on a wide range of scales. Large scale lifting adds potential gravitational energy to the warm air-mass over hundreds of kilometers, while the interaction of cloud particles and radiation acts on micrometer scale. It is not feasible to exactly calculate the state of each micro-scale volume, because it would require a massive amount of computer capacity. Therefore, the impact of processes at a scale smaller than the grid-size of the model (typically 50km) are estimated through sub-grid parameterizations. This is feasible, because the atmospheric processes at small (sub-grid) and large (super-grid) scales are linked (Stull, 1988). A limitation to sub-grid parametrizations is that the correlation between large scale and small scale processes may vary considerably. One of the methods to study the link between cloud processes at various scales is spectral analysis.

The poor representation of clouds in climate models results in a spread of the predictions of climate changes due to an increase of CO₂ in the atmosphere. The direct impact of doubling the concentration of this greenhouse gas in a global averaged atmosphere induces a 4W/m² heating. Results from global climate circulation model calculations show that this induces an increase in surface air temperature of 1.5 – 4.5K (IPCC, 1995). The large range of values is due to differences in the representation of clouds in the model (Gates et al., 1999; Cess et al., 1986; 1990; 1996) and the uncertainty in how the distribution of clouds will evolve (cloud feedback). The sensitivity of climate model results to changes in cloud cover can be understood from the impact of clouds on the radiation budget. If doubling of CO₂ increases the amount of thick stratocumulus over ocean in a climate model, this increases the reflection of sunlight and thus the temperature increase is reduced. This is a negative feedback that stabilizes climate. However, if doubling of CO₂ induces more cirrus in the model, this reduces the radiative cooling of the earth further and thus enhances the temperature increase. This is a positive feedback.

The climate models differ in the representation of clouds and yield different estimates of future climate. In order to reduce the range of estimated global warming the representation of cloud processes should be improved. However, there is a lack of knowledge. As stated by the International Panel on Climate Change (1995): “the most urgent scientific problems requiring attention to determine the rate and magnitude of climate change and sea-level rise are the

factors controlling the distribution of clouds and their radiative characteristics ...” Therefore a number of experimental projects have been executed and are planned, that focus on providing atmospheric modelers with appropriate measurements to improve the models.

1.3 Observations of the current climate

On a global scale, the driving forces of the circulation in the earth’s atmosphere are the distribution of absorbed solar energy and rotational energy of the earth. The solar irradiance perpendicular to the solar beam at the top of the atmosphere (TOA) is about 1372W/m^2 (Fröhlich and Lean, 1998). As the surface of the earth is 4 times its projected area 343W/m^2 is available on average at the TOA. About 70% is absorbed and 30% is reflected into space; the larger part (67%) by clouds (Figure 1.1). On a global scale the incoming radiation is balanced by the emission of thermal radiation. Clearly, clouds modify the earth’s radiation budget, because relative to the earth’s surface clouds are cold and reflect sunlight brightly. Furthermore, clouds occur frequently.

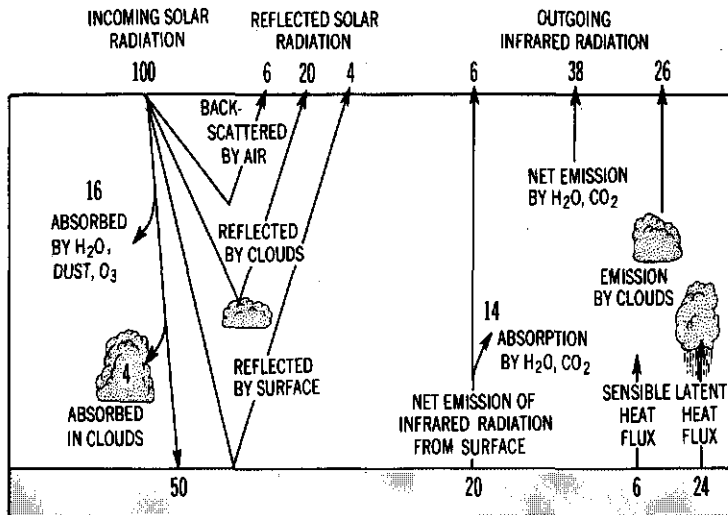


Figure 1.1: Global annual means of the redistribution of incident solar radiation (100% corresponds to an incoming radiative flux density of 343W/m^2) by infrared heat radiation and sensible and latent heat in the climate system (from Peixoto and Oort, 1992).

Information on cloud amounts is obtained by the International Satellite Cloud Climatology Project, ISCCP (Schiffer and Rossow, 1983; Rossow and Schiffer, 1999). This project was

initiated by the World Meteorological Organisation (WMO) as part of the World Climate Research Program (WCRP) in 1983. The ISCCP data set provides the climate research community with a global and 3 hourly climatology on the distribution of clouds at $250 \times 250 \text{ km}^2$ resolution. The cloud amounts are retrieved from measurements from geostationary and polar meteorological satellites. Statistical analysis of ISCCP results show that the global annual average cloud cover fraction is about 63% with a variation smaller than 1% from year to year (Rossow et al. 1993a). There is more cloudiness over sea (70%) than over land (47%). However, the cloudiness over land is probably underestimated by about 3-6%. The monthly mean values have an accuracy of about 10% (Rossow et al 1993b,c) depending on insolation and viewing conditions and surface properties. Comparison with results from imagers with higher spatial resolution suggest that the ISCCP algorithm nicely balances underestimates and overestimates of cloud cover (Wielicki and Parker, 1992; Weare, 1992).

The most commonly used climatology of radiation at the Top of the Atmosphere (TOA) stem from the Earth Radiation Budget Experiment (Barkstrom and Smith, 1986). ERBE was a three satellite mission, which aimed at deriving the spatial distribution and diurnal variation of the radiation components at the TOA. A combination of ISCCP and ERBE results yielded estimates of the difference of the radiation components in cloudy and cloud free conditions (Ramanathan, 1989). On a global yearly average, the amount of solar energy available to the earth-atmosphere is about 50 W/m^2 lower in cloudy conditions than in cloud free conditions. While the amount of energy emitted by the earth-atmosphere system is about 30 W/m^2 lower. So, in our current climate, the direct effect of cloud-radiation interactions is modification of the radiation budget by 20 W/m^2 . The accuracy of an instantaneous measurement at $60 \times 60 \text{ km}^2$ resolution was estimated to be 15 W/m^2 for shortwave flux and 5 W/m^2 for longwave flux (Harrison, 1990; Feijt, 1992).

1.4 This thesis

The work in this thesis was done in the framework of two experimental campaigns: the Tropospheric Energy Budget Experiment, TEBEX (Van Lammeren et al., 2000a; Stammes et al., 1994), and the Clouds and Radiation intensive measurement campaigns, CLARA (Van Lammeren et al., 2000b). The TEBEX clouds-project aimed at 'the reconstruction of the three dimensional cloud distribution suitable for the improvement of sub-grid cloud

parametrizations in atmospheric models.' CLARA was dedicated to improve cloud parameter retrieval methods of the instruments involved.

The aims of this thesis are:

- to develop analysis methods for clouds based on Meteosat and AVHRR measurements
- to validate the retrieval methods with TEBEX and CLARA data
- to use the analysis environment for detailed cloud field studies

In chapter 2, a general introduction to radiative transfer in a cloudy atmosphere is given. The physical principles of cloud-radiative interactions are presented in the context of the wavelength ranges of the meteorological satellite instruments under study.

In chapter 3, a method for analysis of measurements from the AVHRR is presented. This method is used for detailed studies of cloud properties. The AVHRR has 5 spectral channels and a 1km spatial resolution, which makes it suitable for retrievals of a wide range of cloud properties: cloud cover fraction, cloud top temperature, optical thickness, emissivity and liquid water path. However, as the AVHRR is on board a polar orbiter, these measurements are available only a few times per day. The two special features of this analysis environment are the use of Numerical Weather Prediction (NWP) model surface temperatures and the use of Look-up tables from the Doubling-Adding KNMI (DAK) radiative transfer code.

Meteosat is known to the public from the time-loops which are shown on television during the weather forecast. The time-loops of imagery are used to illustrate advection of large scale cloud structures. In this thesis, Meteosat is mostly used to detect clouds at pixel resolution. Detailed study of cloud properties is not attempted, because of the coarse spatial resolution ($5 \times 5 \text{ km}^2$) and the broad spectral band of the visible channel (see chapter 2). In chapter 4, a new cloud detection method is presented that includes the use of surface temperature fields from an operational numerical weather prediction model. An innovative aspect of the method is that the difference between temperatures from the NWP model and as measured from satellite for cloud free conditions is quantified. The skill of the detection method was evaluated over land and ocean for 1997 on a 3 hourly basis by comparison with synoptic

observations. It is shown that the new approach improves the skill of the detection method considerably.

In chapter 5, the retrieval results of Meteosat and AVHRR are compared to observations from ground based remote sensing from the TEBEX and CLARA data sets. This comparison yields unique information on the quality of the satellite retrievals and also on the merits of the ground based remote sensing instruments. The comparison shows that both observational sets have strong points, but a combination is preferred to obtain a good description of the cloud field.

In chapter 6, the correlation between time scales and spatial scales of cloud field variability is studied by comparing variance spectra of time series and spatial distributions of liquid water path derived from microwave radiometer and AVHRR data respectively. The link between atmospheric processes at large and small scales is the physical basis for sub-grid parametrizations in atmospheric models. This link can be studied with spectral analysis of the variance of cloud properties. Spatial scales of cloud field properties can be studied from satellite images, which measure a spatial distribution at one moment in time. Time scales of cloud field properties can be derived from ground based instruments that measure continuously in time at one location. The study investigates the constraints to the comparison of ground based and satellite measurements. Because clouds are highly variable both in time and space it is always questionable which part of the time series corresponds to which part of the spatial distribution.

Results from the satellite cloud parameter retrievals presented in this thesis are used for evaluation of a regional climate model. The satellite data were combined with measurements from a network of stations for ground based remote sensing to obtain an estimate of the distribution of clouds over an area of the size of a climate model grid box. A number of cases are described in the literature (Van Lammeren et al., 2000a; Van Meijgaard et al, 2000). Furthermore, the Meteosat analysis environment is employed to initialize an operational short-term cloud prediction model (Van der Veen and Feijt, 1996). New studies are being done and are planned. In chapter 7 this thesis is put in perspective.

References

- Barkstrom B.R. and G.L. Smith, 1986: The Earth Radiation Budget Experiment: Science and implementation. *Rev. Geophys.* 24, 379-390.
- Cess, R.D. et al., 1989: Interpretation of cloud-climate feedback as produced by 14 atmospheric general circulation models. *Science*, 245, 513-516.
- Cess, R.D. et al., 1990: Intercomparison and interpretation of climate feedback processes in 19 general circulation models. *J. Geophys. Res.*, 95, 16601-16615.
- Cess, R.D. et al., 1996: Cloud feedback in atmospheric general circulation models: An update. *J. Geophys. Res.*, 101D, 12791-12794.
- Feijt, A.J., 1992: The Earth Radiation Budget Experiment: Overview of data-processing and error sources. KNMI TR-162, KNMI, De Bilt, 36pp.
- Frohlich, C. and J. Lean, 1998: The Sun's total irradiance: Cycles, Trends, Related Climate Change Uncertainties since 1976. *Geophys. Res. Lett.*, 25, 4371-4380.
- Gates, W.L. et al., 1999: An overview of the results of the atmospheric model intercomparison project (AMIP I), *Bull. Amer. Meteor. Soc.*, 80, 29-55.
- Harrison, E.F., P. Minnis, B.R. Barkstrom, V. Ramanathan, R.D. Cess and G. Gibson, 1990: Seasonal variation of cloud radiative forcing derived from the Earth Radiation Budget Experiment. *J. Geophys. Res.*, 95, 18687-18703.
- International Panel on Climate Change, 1995: IPCC Second Assessment Report – Climate Change 1995, UNEP/WMO.
- Lammeren A. van, A. Feijt, J. Konings and E. van Meijgaard, 2000a: Combination of ground Based and satellite cloud observations on a routine basis. *Contr. Atmos. Phys.* (in press).
- Lammeren, A. van , H. Russchenberg, A. Apituley, H. ten Brink and A. Feijt, 1998: CLARA a data set to study sensor synergy. *Proc. 'Synergy of Active instruments of the Earth Radiation Mission'*, nov. 12-14, GKSS, Geesthacht, Germany.
- McClatchey, R. et al., 1972: Optical properties of the atmosphere, 3-rd ed., AFCRL-72-0497, Air Force Cambridge Research Labs., 107pp.
- Meijgaard E. van, J. Konings, A. Feijt and A. van Lammeren, 2000: Comparison of model predicted cloud cover profiles with observations from ground and satellite. *Contr. Atmos. Phys.* (in press).
- Peixoto, J.P. and A.H. Oort, 1992: The physics of Climate, American Institute of Physics, N.Y.

- Ramanathan, V., R.D. Cess, E.F. Harrison, P. Minnis, B.R. Barkstrom, E. Ahmad and D. Hartmann, 1989: Cloud radiative forcing and climate: Results from the Earth Radiation Budget Experiment. *Science*, 243, 57-63.
- Rossow, W.B. and R.A. Schiffer, 1999: Advances in understanding clouds from ISCCP. *B.A.M.S.*, 80, 11, 2261-2288.
- Rossow W.B. and L.C. Garder, 1993a: Cloud detection using satellite measurements of infrared and visible radiances for ISCCP, *J. Climate*, 6, 2341-2369.
- Rossow W.B. and L.C. Garder, 1993b: Validation of ISCCP cloud detection, *J. Climate*, 6, 2370-2393.
- Rossow W.B., A.W. Walker and L.C. Garder, 1993c: Comparison of ISCCP and other cloud amounts, *J. Climate*, 6, 2394-2418.
- Rossow W.B. and R.A. Schiffer, 1991: ISCCP cloud data products. *B.A.M.S.*, 72, 2-20.
- Schiffer, R.A. and W. B. Rossow, 1983: The International Satellite Cloud Climatology Project (ISCCP): The first project of the World Climate Research Program. *Bull. Amer. Meteor.Soc.*, 64, 779-784.
- Stammes, P., A. Feijt, A. van Lammeren and G. Prangmsma, 1994: TEBEX observations of clouds and radiation – potential and limitations. KNMI TR-162, KNMI, De Bilt.
- Stull, R.B.: An introduction to Boundary Layer Meteorology. Kluwer, 666 pp., 1988.
- Veen, S. van der, and A. Feijt, 1996: Liquid water initialization in a cloud prediction model Using Meteosat imagery. *Proc. of the 1996 EUMETSAT Meteorological Satellite Data Users'Conference*, EUMETSAT, Darmstadt, 257-264.
- Weare, B. A., 1992: A comparison of ISCCP C1 cloud amounts with those derived from high resolution AVHRR images. *Int. J. Rem. Sens.*, 13, 11, 1965-1980.
- Wielicki, B. A. and L. Parker, 1992: On the determination of cloud cover from satellite sensors: The effect of sensor spatial resolution. *J. Geophys. Res.*, 97, 12799-12823.

2 Radiative transfer in a cloudy atmosphere

The identification and characterization of cloud fields from satellite rely on the interpretation of radiance measurements. In this chapter, the physics of radiative transfer in a cloudy atmosphere is discussed. The emphasis is on the wavelength ranges of the window channels of the AVHRR.

2.1 Atmospheric radiative transfer

In this section, the atmospheric radiative transfer in the solar and infrared regimes is described. The choice of the wavelength ranges of the meteorological satellite instruments is explained from the radiative properties of atmospheric constituents (gases, aerosols, clouds) and the surface.

2.1.1. Shortwave radiation

The source of shortwave irradiance at the earth's top of the atmosphere (TOA) is the sun. The spectrum of the sun, as measured at TOA (Stephens, 1984; Lacis and Hansen, 1974), is shown in Figure 2.1. It is similar to Planck's curve for a black body at about 6000K, but less smooth, because of absorption in the outer layer of the sun. The solar irradiance is attenuated on its

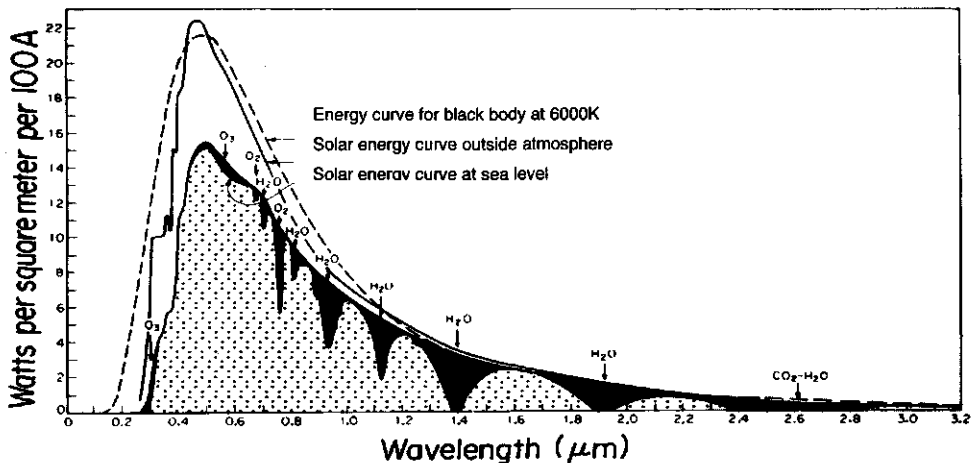


Figure 2.1: Spectral energy curves of solar radiation at sea level and extrapolated outside the atmosphere. The darkened areas illustrate gaseous absorption bands while the unshaded area represents Rayleigh scatter effects. Modified from Lacis and Hansen (1974) by Stephens (1984)

path through the atmosphere due to scattering and absorption. The sum of absorption and scattering is known as extinction. Therefore, the irradiance spectrum as measured at sea level for cloud free conditions (the lower curve in Figure 2.1) deviates considerably from the TOA. This curve shows decreased intensity over the whole range due to Rayleigh scattering by atmospheric gases. The reduction is stronger at shorter wavelengths, because the extinction due to Rayleigh scattering has a wavelength dependence of λ^{-4} . The black areas in Figure 2.1 indicate absorption by atmospheric gases.

The definition of wavelength ranges for the meteorological satellites under study was determined by optimization of the contrast between cloud free and cloudy condition. Therefore, the channels should be chosen such that there is:

- high contrast between clouds and surface
- small influence of other atmospheric constituents
- a high signal to noise ratio

To obtain a maximum signal, the shortwave channels include the wavelength range near the peak in the solar spectrum, which is at about $0.5\mu\text{m}$. The channels should not include strong absorption bands. The wavelength bands of the Meteosat and AVHRR are indicated in Figure 2.2. The Meteosat visible channel spectral response function centers to the right of the peak of the solar spectrum and includes various absorption bands. The channel is broad in order to receive enough energy at its distant location $36,000\text{km}$ from the earth. The AVHRR $0.6\mu\text{m}$ channel is less broad and is centered near the peak in the solar spectrum. It does not include strong absorption bands, but includes moderate Rayleigh scattering. Therefore, it is more suitable for cloud analysis than the Meteosat visible channel. The AVHRR $0.8\mu\text{m}$ channel includes absorption lines from water vapor and the oxygen A-band at $0.762\mu\text{m}$. The inclusion of absorption bands in this instrument channel reduces its usefulness for quantitative analysis. However, this wavelength range is useful to measure surface properties, which is explained below.

The contrast between surface and cloud should be at a maximum for the identification of cloudy scenes and for quantitative analysis of the radiances to obtain cloud properties. The spectrum of clouds is nearly flat (Bowker et al., 1985). Therefore, the wavelength ranges with minimum surface reflectivity are most suitable. In Figure 2.2 the spectrum at the top of the

atmosphere at nadir as measured from GOME on board the ERS-2 for a cloud free day over the Netherlands is shown (Stammes and PETERS, 1996). The Instantaneous Field of View (IFOV) of the instrument is $40 \times 360 \text{ km}^2$, and thus the signal includes contributions from many

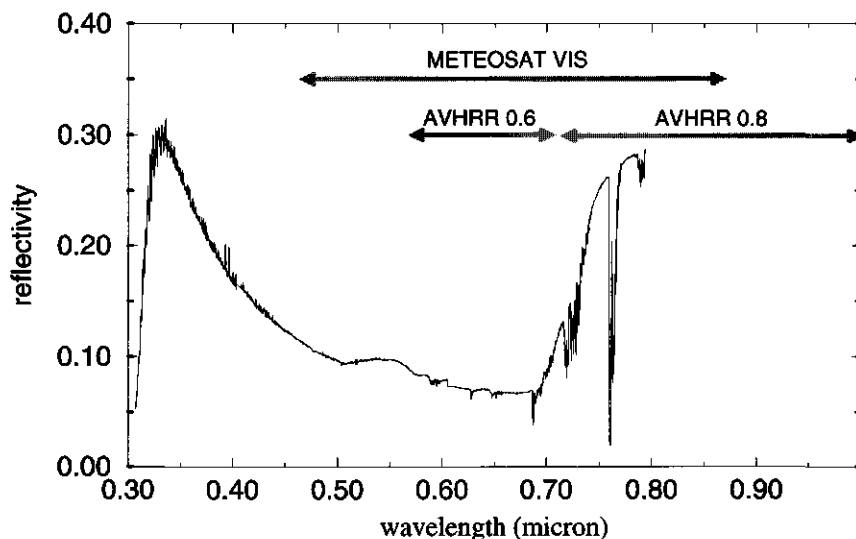


Figure 2.2: Spectrum at TOA measured from GOME for a cloud free day over the Netherlands.

different vegetation and surface types. However, this spectrum is suitable to illustrate the large differences of surface reflectivity in the $0.6 \mu\text{m}$ and $0.8 \mu\text{m}$ channels, which are indicated in the Figure. At $0.6 \mu\text{m}$ the reflectivity is relatively low, which is preferred for cloud analysis. At $0.8 \mu\text{m}$ reflectivity is relatively high. The difference between reflectivity in both AVHRR visible channels is caused by the absorption by chlorophyll at $0.6 \mu\text{m}$. As a result, the $0.8 \mu\text{m}$ channel is not suitable for analysis of cloud properties over land, but (in combination with the $0.6 \mu\text{m}$ channel) can be used as an indicator for the amount of vegetation. Also the Meteosat channel wavelength range is indicated. From Figure 2.2 we may conclude that the Meteosat is less suitable for cloud analysis over land, because the reflectivity for clear sky conditions may be more than 25%.

2.1.2. Longwave radiation

The longwave radiation discussed in this section originates from the earth's surface or atmospheric constituents (gases, clouds and aerosols). Planck's law relates emitted longwave radiation and temperature of a perfect black body:

$$B_{\lambda}(T) = (8\pi hc/\lambda^5) \{ \exp[hc/\lambda kT] - 1 \}^{-1} \quad \text{Wm}^{-2}\text{sr}^{-1}\mu\text{m}^{-1} \quad (2.1)$$

where λ the wavelength in μm ; T the temperature in K; c is the speed of light in m/s; h is Planck's constant in Js; and k is Boltzmann's constant in J/K.

The temperature of the earth surface ranges roughly from 220 to 320K. The corresponding maxima in the Planck's curve occur at 13 and $9\mu\text{m}$, respectively. In Figure 2.3, Planck's curve is shown for a surface temperature of 275, 290 and 305K. The thermal radiation of the surface is partly absorbed by the gases in the atmosphere. The gases re-emit at their ambient temperature. The impact on the spectrum of atmospheric absorption in cloud free conditions is illustrated by the solid curve in Figure 2.3. This curve is the spectrum at the TOA obtained from Modtran calculations for mid latitude conditions and a surface temperature of 290K. The atmosphere absorbs efficiently at most wavelengths. The attenuation is at its minimum in the

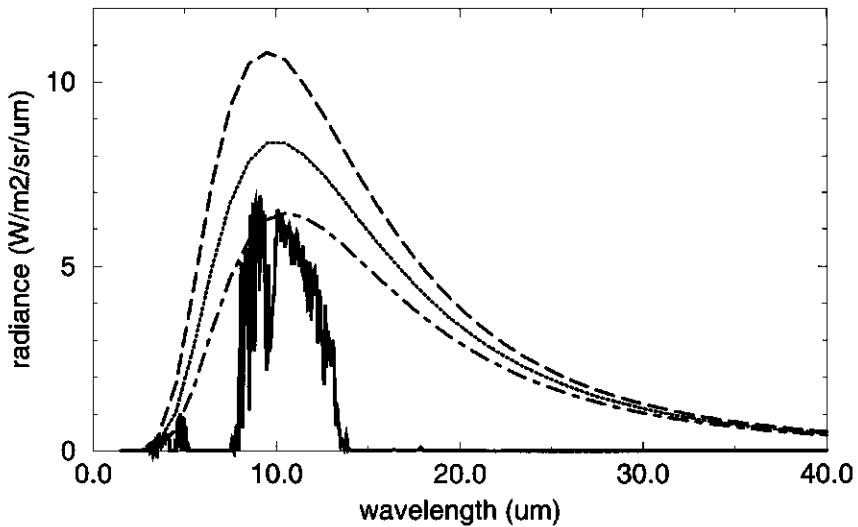


Figure 2.3: Spectral radiances at the TOA for a MLS atmosphere over a black body at 290K (solid) and Planck's curve for a surface at 275K (dashed dotted), 290K (dotted) and 305K (long dashed).

8-12.5 μm range with the exception of the ozone absorption band at 9.6 μm . Due to the low attenuation, the 8-12.5 μm wavelength range is called the atmospheric window and is suitable to analyze cloud and surface temperatures.

Both the Meteosat and AVHRR have a channel in the atmospheric window, because it gives the best estimate of the temperature of both the clouds and the surface. In general, clouds are colder than the surface, because temperature decreases with height. This implies that the contrast between cloud free and cloudy conditions is optimal in the atmospheric window.

2.2. Cloud-radiation interactions at 0.6 μm

From a radiative transfer perspective, a cloud is an ensemble of particles that scatter, absorb and emit radiation. The radiative transfer is determined by the characteristics of the cloud particles and their horizontal and vertical distribution in the atmosphere. In this section, cloud-radiation interactions in the atmospheric window at 0.6 μm will be described for liquid and ice particles. In the next section the interactions at 10.8 μm will be described. The AVHRR cloud parameter retrieval method, which is described in chapter 3, is based on the analysis of the measured radiances at these wavelengths.

2.2.1. Water clouds

In general, it is assumed that water cloud droplets are spherical, which is a robust assumption. The interaction of monochromatic light with a single spherical water particle, can be described by three parameters:

- the single scattering albedo, ω ,
- the scattering efficiency, Q
- the phase function, P .

The single scattering albedo is the ratio of amount of scattered light over the total amount of light removed from the incident beam by the particle. The attenuation of the incident solar radiation is caused either by scattering or absorption. In general, it is assumed that at 0.6 μm hardly any light is absorbed by water cloud particles, so ω approximates unity.

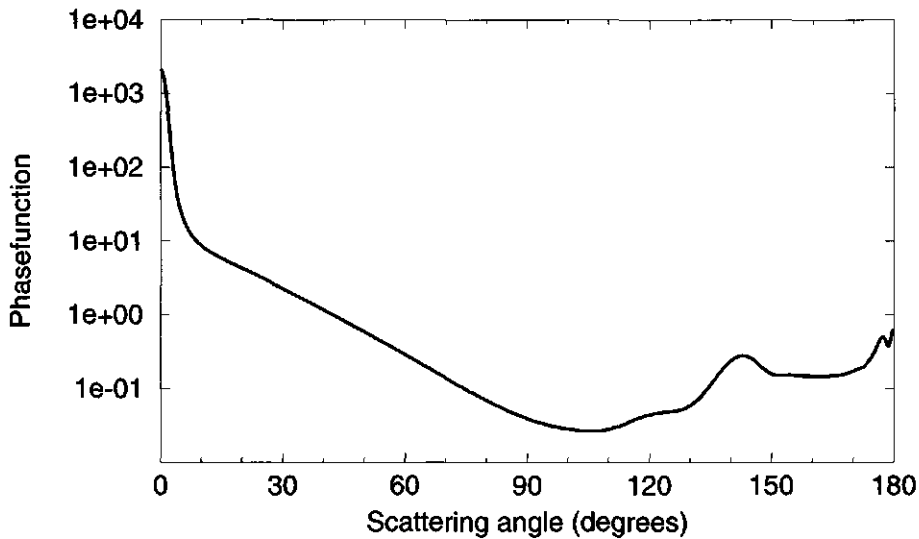


Figure 2.4: Scattering phasefunction for a distribution of water spheres.

The scattering efficiency, $Q(r, \lambda)$, is the ratio of the amount of light that is scattered by a single particle, to the amount of light incident on its projected area. This coefficient depends on the radius of the sphere, r , and the incident wavelength, λ . According to Mie theory, the scattering coefficient of a perfect spherical water droplet varies strongly with its size between 0 and $4\mu\text{m}$. For small particles ($r < 0.1\mu\text{m}$) the cloud-radiation interaction is in the Rayleigh regime. For large particles ($r > 20\mu\text{m}$) the geometrical optics limit can be applied, which defines Q to be 2. For monodisperse water spheres of radius 0.1 to $20\mu\text{m}$, $Q(r)$ varies considerably with size, with mode of about 2 and maximum 4. In clouds, the size distribution is never monodisperse and therefore the variations in scattering coefficient average out. For wide distributions of particle sizes the scattering coefficient may be assumed to be 2 for large particles and about 2.3 for small ($r \approx 2\mu\text{m}$) particles (Minnis et al., 1998).

The phase-function, $P(\Theta)$, is the amount of energy scattered at an angle Θ relative to the direction of propagation of the incident light. The angular distribution of scattering of the incident light by a single spherical water drop can be calculated exactly using Mie-theory. A typical phase functions for a distribution of water spheres illuminated by monochromatic light of wavelength $0.6\mu\text{m}$, is shown in Figure 2.4 (Koelemeijer et al., 1995). The main features are: the distinct forward peak ($\Theta = 0$), a minimum near the side-scattering angle ($\Theta = 90$), the cloud bow at ($\Theta = 140$), and the backscatter peak ($\Theta = 180$). The phase functions for water

spheres of size 4 to 20 μm are similar, but the features differ in proportion and location. The larger water spheres have a phase function with a more distinct forward peak. The cloud bow is shifted to a slightly smaller phase angle. The forward peak includes light that is hardly redirected and thus can hardly be distinguished from the incident light. Therefore, in many approaches to radiative transfer calculations the strong forward peak is excluded from calculations to reduce the computational burden (Minnis, 1991, 1995). The cloud bow, the local maximum near 140 degrees, is the cloud particle analog of the rainbow. The peak near backscatter geometry, 180 degrees, indicates the glory, which sometimes can be seen from an aircraft as a ring around its shadow. Cloud bow and glory can only be seen clearly if the droplets in the top of the cloud all have about the same size. The droplet size distribution must be narrow, because the peak in the phase function shifts gradually with drop radius and thus a wide distribution smoothes the intensity peak.

The first order measure of the effect that a cloud has on radiation is defined by its optical thickness, τ . The optical thickness can be interpreted as the number of scattering events a photon would have if it was to penetrate a cloud vertically without being attenuated or deflected from the incident beam. The optical thickness of a cloud is the product of projected area of the particles and their scattering coefficient. The latter depends on the wavelength. In formula:

$$\tau = \int n(r) A(r) Q(r, \lambda) dr = \int n(r) Q(r, \lambda) \pi r^2 dr \quad (2.2)$$

where, $n(r)$ is the number of particles of size r and $A(r)$ is the projected area.

In a cloud, photons are redirected after each interaction with a water drop. Because absorption is low, a photon may scatter 100 times on its path through the cloud. The photon may travel a considerable distance through the atmosphere, before being scattered outside the cloud either to the surface or into space (Feigelson, 1984). This multiple scattering induces effects that are specific for clouds. The increase of the optical path may amplify weak atmospheric absorption or scattering (Stammes, 1994). Furthermore, the radiation field is smoothed spatially, because photons travel over several hundreds of meters (Marshak, 1998; Savigny, 1999). This sets a lower limit to the geometrical size of measurements that can be analyzed independently from their environment (Cahalan et al., 1994). The increase of the optical path was directly

measured from space during the Lidar in Space Technology Experiment, LITE (Winker et al., 1996). The optical path in the cloud was occasionally lengthened by several kilometers.

The reflection of a cloud as measured from satellite is the result of multiple interactions between photons and cloud particles in the 1 to 10km instantaneous field of view (IFOV) of the instrument. Due to the phase function and multiple scattering effects the cloud reflectivity is not evenly distributed over all angles (isotropic reflection), but depends on the angles of incidence and reflection (anisotropic reflection). The anisotropy is quantified in the bi-directional reflection function. In Figure 2.5, the sun-satellite geometry is shown. It defines the solar zenith angle, θ_0 , the viewing zenith angle, θ , and the relative azimuth, ϕ , which is the angle between the plane of incidence and the plane of reflection. The measurement of the anisotropy of clouds requires radiance measurements at all viewing angles and azimuths at the same time. This is technically not feasible, because it would require a large number of aircraft or satellites that all measure the radiation coming from one location at the same time. Nevertheless, there have been attempts to estimate anisotropy from sequences of measurements.

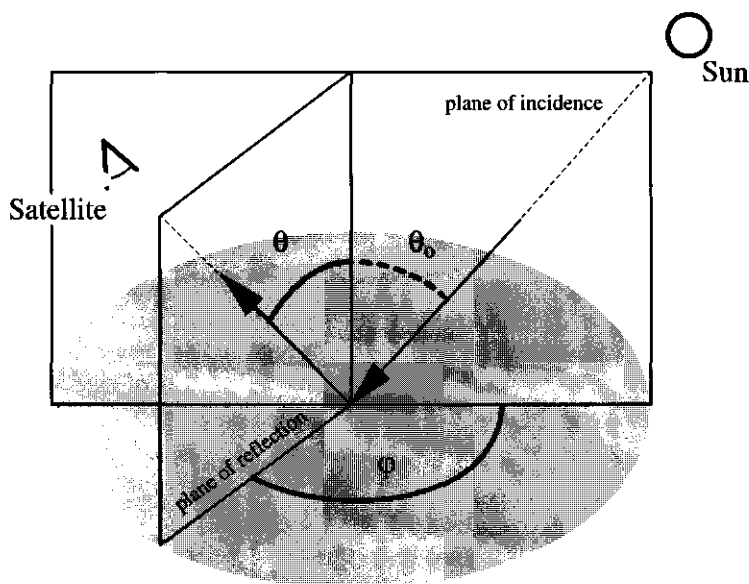


Figure 2.5: Sun-satellite scattering geometry.

In the 1970's the angular distributions of broad band shortwave and longwave radiation were measured from space with the Nimbus-7 satellite. In a specific mode it was possible to keep the instruments IFOV of about $60 \times 60 \text{ km}^2$ focussed on one location while the satellite was moving along its orbit around the earth, and thus gradually changing the viewing angle and the azimuth angle. Taylor and Stowe (1984a,b) statistically manipulated the data set to provide the scientific community with lookup tables of measured albedo and angular distributions of reflectivity for a number of surface types and cloud types. Although the lookup table represents the statistical means over a wide variety of climate regimes and surface types, and inherently the distributions show a large dispersion, the table is widely used in the analysis of broadband radiometer signals (Suttles et al, 1988,1989; Wielicki et al., 1989) and in the analysis of meteorological satellite measurements: AVHRR (Kriebel et al., 1989) and Meteosat (De Valk et al., 1997).

More recently, the anisotropy function over an extended stratocumulus field was reconstructed for narrow spectral bands from aircraft measurements with POLDER (Descloîtres et al. 1995; Parol et al, 1994). POLDER instantaneously measures at different

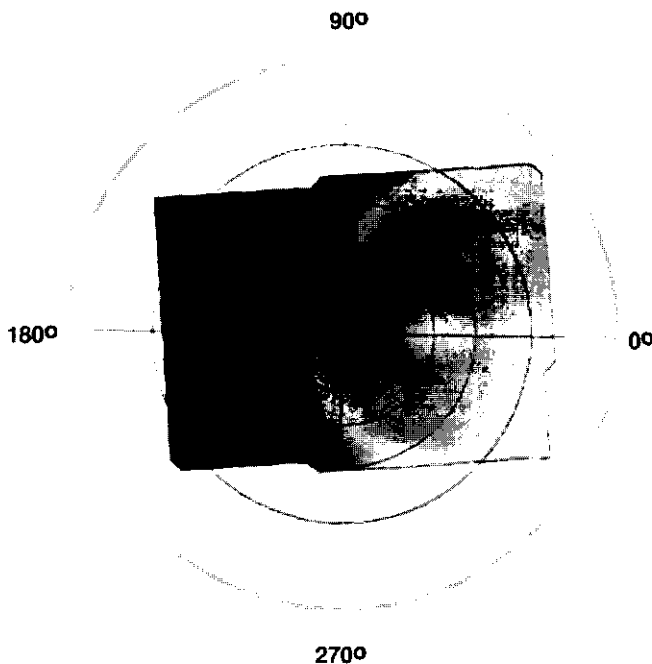


Figure 2.6: Pattern of observed bidirectional reflectances over stratocumulus clouds. Solar zenith angle is 36° . Circles correspond to viewing zenith angles, and axis correspond to relative azimuth (from Parol et al., 1994). Scaling: black, $0.53 < \text{reflectivity} < 0.61$, white.

viewing zenith and azimuth angles. The instrument gives an instantaneous angular distribution, however, the radiation measured at different angles originates from different locations. Therefore, the instantaneous measurement is only representative in case of spatially homogeneous cloud fields. In Figure 2.6 the anisotropy is shown from an average of 10 consecutive measurements. The most pronounced feature is the arc of high reflectivity related to the single scattering cloud bow peak in the phase function. The need for correct estimates of the anisotropy of radiation is reflected in the current initiative to obtain values at $40 \times 40 \text{ km}^2$ resolution for about 200 different scene types from CERES (Wielicki et al., 1996).

It may seem a bit awkward to invest so much efforts to measure bi-directional reflection functions while the radiative transport can be calculated exactly from Mie-theory combined with a radiative transfer model that includes multiple scattering. The reason is that accurate radiative transfer calculations require information on microphysical properties and the 3 dimensional structure of the cloudy scene under study. This results in assumptions on:

- Single scattering properties, for water clouds directly related to $n(r)$.
- Horizontal distribution of scatterers
- Vertical distribution of scatterers, variations in the vertical extent

The drop size distribution is not the same for all cloud fields. On the contrary, the frequency distribution of drop sizes reflects the complex physical processes related to generation and evaporation of water droplets. The frequency distribution changes with place and time continuously. For example, the life cycle, from condensation to evaporation, of fair weather cumuli of 1 km size only lasts tens of minutes. This implies that the maximum change of droplet size for fair weather cumuli, from zero to maximum, occurs within tens of minutes and within 1 km. Obviously, the actual drop size distribution at the time of satellite overpass is not known. Therefore, in the retrieval a dropsize distribution has to be assumed. In general, measured distributions corresponding to specific meteorological cloud types are used such as those described by Stephens (1978) and Dermendjian (1969).

The horizontal variability of optical thickness has a considerable impact on the relation between number of scatterers and cloud radiative properties (Cahalan et al., 1994). The contribution of cloud structures of a specific spatial scale to the variance can be quantified and even modeled for specific cloud types using the bounded cascade method (Cahalan et al.,

1989). This model is used in studies on the impact of variability of optical thickness on radiation components (Boers et al., 2000). However, if there are considerable optical thickness variations within a cloud field, this in general implies variations in the vertical extent as well. This also has considerable impact on the radiation field.

Variations in the vertical extent of clouds causes three dimensional cloud-radiation effects like shadows. In meteorological practice, the horizontal extent of shadows is used to estimate the cloud height. Actually, the horizontal extent of the shadow of a cloud over cloud free area in the plane of insolation, S_{shadow} , is related to the height of the cloud through the tangens of the solar zenith angle. Also, in case of a multi-layer cloud system, the top layer may be identified by its shadow on a lower layer. There have been some sensitivity studies on the impact of three dimensional effects on radiative transfer. A method, which is widely used, is Monte Carlo modeling, which calculates the path of a large number of photons (typically a million) through the cloud. Each individual scattering event is taken into account. In these studies the geometrical shape of clouds are represented by boxes, spheres, cylinders or hexagons of various sizes. These studies have shown that indeed three-dimensional structures do affect the radiative transfer significantly both for satellite observations (Davies, 1978; Jolivet, 1999) and surface based observations (Coley and Jonas, 1995). However, it is not feasible to use Monte Carlo calculations to interpret radiances in the IFOV of the satellite instrument, because there is no information available on the three dimensional distribution of cloud particles.

2.2.2. Ice clouds

The phase function, which plays an important role in the radiative transfer in clouds, is different for ice crystals and water droplets. This is due to their different size and shape. Ice crystals occur in many shapes and sizes (Pruppacher and Klett, 1978). In Figure 2.7, examples of ice crystals shapes are shown. The basic shapes are columns and plates, which can occur in aggregates as well. The size ranges from 10 to 2000 μm . The shape and size depend on the time the crystal has grown, the relative humidity, temperature and the history of the air mass. Heymsfield (1994) and Heymsfield and Platt (1984) analyzed measurements of ice crystal shape and size and quantified the correlation between temperature and crystal size in terms of a parameterization. For large ice crystals, ($r > 100\mu\text{m}$) the phase function cannot be described in an analytic formula for arbitrary shapes and sizes. Only for some special non-spherical












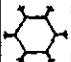

























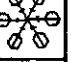


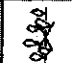








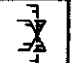



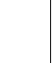




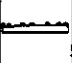









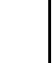











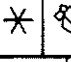


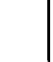
	N1a Elementary needle		C1f Hollow column		P2b Stellar crystal with sectorlike ends
	N1b Bundle of elementary needles		C1g Solid thick plate		P2c Dendritic crystal with plates at ends
	N1c Elementary sheath		C1h Thick plate of skeleton form		P2d Dendritic crystal with sectorlike ends
	N1d Bundle of elementary sheaths		C1i Scallops		P2e Plate with simple extensions
	N1e Long solid column		C2a Combination of bullets		P2f Plate with sectorlike extensions
	N2a Combination of needles		C2b Combination of columns		P2g Plate with dendritic extensions
	N2b Combination of sheaths		P1a Hexagonal plate		P2a Two-branched crystal
	N2c Combination of long solid columns		P1b Crystal with sectorlike branches		P2b Three-branched crystal
	C1a Pyramid		P1c Crystal with broad branches		P2c Four-branched crystal
	C1b Cup		P1d Stellar crystal		P4a Broad branch crystal with 12 branches
	C1c Solid bullet		P1e Ordinary dendritic crystal		P4b Dendritic crystal with 12 branches
	C1d Hollow bullet		P1f Fertile crystal		P5 Malformed crystal
	C1e Solid column		P2a Stellar crystal with plates at ends		P6a Plate with spool plates
	P6b Plate with spool dendrites		P6c Stellar crystal with spool plates		P6d Stellar crystal with spool dendrites
	P7a Radiating assemblage of plates		P7b Radiating assemblage of dendrites		C7a Column with plates
	C7b Column with dendrites		C7c Multiple capped column		R2a Densely rimmed plate or sector
	R2b Densely rimmed stellar crystal		R2c Stellar crystal with rimmed spool branches		R3a Grouped-like snow of hexagonal type
	R3b Grouped-like snow of lump type		G4 Minute stellar crystal		G5 Minute assemblage of plates
	G1 Minute column		G2 Germ of skeleton form		G3 Minute hexagonal plate
	I3a Broken branch		I3b Rimmed broken branch		I4 Miscellaneous
	I12 Rimmed particle		I11 Ice particle		R4c Concave groupel
	R4a Hexagonal groupel		R3c Groupel-like snow with nonrimmed extensions		R4b Lump groupel
	S1 Side planes		S2 Scale-like side planes		S3 Combination of side planes, bullets, and columns
	R1a Rimmed needle crystal		R1b Rimmed columnar crystal		R1c Rimmed plate or sector
	R1d Rimmed stellar crystal		I3a Broken branch		I3b Rimmed broken branch
	I4 Miscellaneous		G1 Minute column		G2 Germ of skeleton form
	G3 Minute hexagonal plate		G4 Minute stellar crystal		G5 Minute assemblage of plates
	G6 Irregular germ		R3a Groupel-like snow of hexagonal type		R3b Groupel-like snow of lump type

Figure 2.7: Classification of ice crystal shapes (from Magano and Lee, 1966).

particles analytic solutions exist (Mischenko et al, 2000). However, the phase function can be obtained by the ray tracing technique. This method involves the calculation of millions of photon paths through the crystal for a variety of incident angles and crystal orientations. Each interaction of a photon at the ice/air boundary is described with the laws of reflection and refraction of plane waves at media boundaries. Hess and Wiegner (1994) calculated phase functions for a wide range of hexagonal ice crystal shapes. The phase function shows a number of distinct scattering features like halos of which the scattering angle and magnitude strongly depend on the exact crystal shape. Therefore, the phase function is representative for only one specific crystal shape. This limits the applicability in the interpretation of radiation measurements Macke (1996; 1994) succeeded in generating a phase function without distinct features, which is more generally applicable, using the scattering characteristics of a fractal ice crystal. This theoretically exact shape of infinite detail is assumed to resemble the statistical mean of the scattering effects of a wide variety of shapes and sizes. Recently, Hess et al.(1998) produced a similar phase function using statistical means of columns and plates with varying rate of imperfection and distortion. (Figure 2.8).

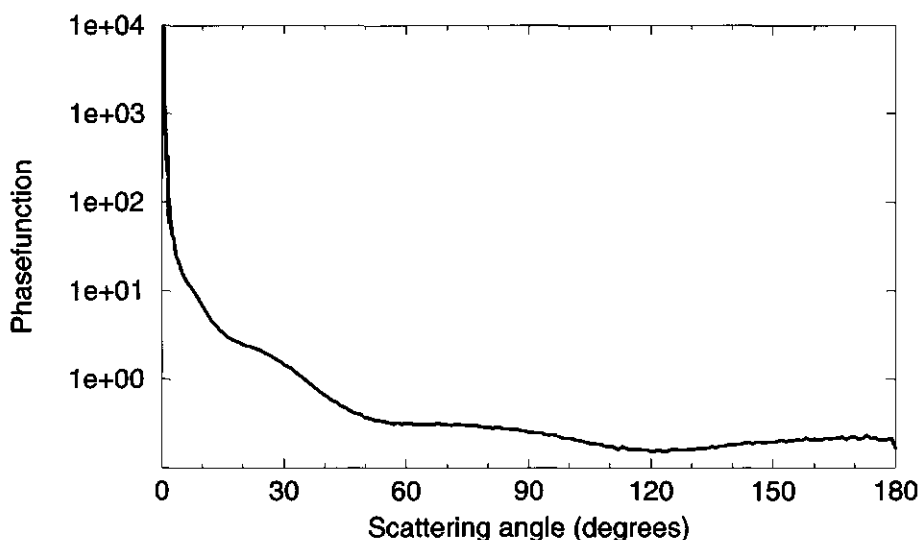


Figure 2.8: Scattering phasefunction for a distribution of ice crystals.

As discussed earlier, any conceptual model of water or ice clouds, which is the basis for radiative transfer calculations, suffers from a lack of information on microphysics and three

dimensional structure, which in general, cannot be measured directly. The quality of the concept is evaluated indirectly by comparison of the retrieved macro-physical cloud parameters with other measurements. In order to improve the concept itself, information on droplet sizes, layering, three dimensional structure and high resolution variability collocated with radiometer measurements are required. Therefore, intensive measurement campaigns like CLARA (Van Lammeren et al., 2000) are of great value.

2.3. Cloud-radiation interactions at $10.8\mu\text{m}$

Cloud-radiative interactions in the longwave range can be understood from the single scattering properties. In the following, some typical values for clouds are given (Minnis, 1998). The radiation as measured from an optically thick cloud layer may be interpreted as the black body radiation emitted by the top layer, because the cloud-radiation interaction of cloud particles at $10.8\mu\text{m}$ is dominated by absorption and emittance. For large cloud particles, the absorption efficiency is about 1. The lower size limit for this approximation is about $12\mu\text{m}$ for liquid water droplets and about $50\mu\text{m}$ for ice crystals. This implies that all radiation incident on the projected area of the particle is absorbed. The cloud particle re-emits black body radiation corresponding to its temperature.

For large particles the extinction efficiency is about 2 and the single scattering albedo is about 0.5. So, an equal amount of radiation is scattered and absorbed. The scattering is mainly directed forward. The asymmetry parameter, g , which is the ratio of forward scattered radiation and incident radiation, is larger than 0.93 for the large particles considered here. This implies that more than 90% of the incident radiation (from below) is scattered forward (upward) and less than 10% is scattered backward (to the surface). As a result, the scattering of infrared radiation has a minor impact on the radiation field and is, in general, ignored.

For optically thin clouds, the radiation at the top of the atmosphere is a weighted average of contributions from the cloud and contributions from the surface transmitted through the cloud.

If a number of simplifying assumptions are met, this can be approximated by:

$$R_{\lambda, \text{TOA}} = \epsilon_{\lambda} B_{\lambda}(T_{\text{cloud}}) + (1 - \epsilon_{\lambda}) B_{\lambda}(T_{\text{surface}}) \quad (2.3)$$

where $R_{\lambda, \text{TOA}}$ is the monochromatic radiance at the top of the atmosphere; $B(T)$ is Planck's curve at wavelength λ , corresponding to temperature T ; ϵ_{λ} is the emissivity of the cloud. The emissivity is the vertically integrated effect of a cloud on radiation and can be formulated as:

$$\epsilon_{\lambda} = 1 - \exp(-\tau_{\lambda, \text{abs}}/\mu) \quad (2.4)$$

where $\tau_{\lambda, \text{abs}}$ is the absorption optical thickness at wavelength λ and μ is $\cos(\theta)$. For clouds of high absorption optical thickness, ϵ_{λ} approaches 1, such that the measured radiance equals the equivalent black body temperature of the cloud. Equations (2.3) and (2.4) are used widely in retrieval of cloud temperatures for water and ice clouds. There are, however, a number of details of radiative transfer, which are not taken into account. These may reduce the accuracy of the retrieval considerably. In the following the most important assumptions made in this approach are evaluated.

Equation (2.4) assumes that the drops do not scatter any incident radiation, but only absorb all radiation incident on their projected area. As described above, this is not true. There are also scattering effects, especially for small cloud particles. The (multiple-)scattering reduces the amount of radiation from the surface that is transmitted un-impeded through the cloud and increases the effect of the cloud on the radiation field. The emissivity, which is used in equation 2.3 should include this effect. Minnis studied the impact of scattering on retrieved emissivity with a infrared doubling-adding model (Minnis et al., 1998; Minnis, 1991). It was found that the emissivity may be underestimated by up to 10% using equations 2.4, depending on viewing geometry, optical thickness and the temperatures of surface and cloud. The effect is largest for large viewing angles, large temperature differences between cloud top and surface and for $1 < \tau_{10.8\mu\text{m}, \text{abs}} < 4$.

Equation 2.3 assumes one cloud temperature, which is a valid assumption for dense clouds. For typical liquid water clouds this assumption holds. However, for ice clouds the density of scattering particles per volume may be much lower (Pruppacher and Klett, 1978). An ice cloud of optical thickness 2 may be 2km thick, which implies that the temperature difference between cloud top and base is more than 10K. As a result, T_{cloud} in equation 2.3 does not represent the temperature of the cloud top, but the temperature of a level within the cloud. The exact level depends on the vertical profiles of particle number density and temperature, the surface temperature and the radiative properties of the ice crystals. This kind of detailed information is hardly ever available.

The conceptual model of the radiative transfer in the thermal atmospheric window, which is basis for equations (2.3) and (2.4), also does not include:

- layering of clouds
- variability of vertical extent
- partly cloudy scenes
- emissivity of the earth surface not equal to one
- atmospheric absorption (under and above the cloud)
- heterogeneity of the surface properties

The required information is not available. It is not expected that the first two phenomena will give rise to modeling problems in a significant number of cases. In order to significantly change the radiation at the top of the atmosphere, as measured from satellite, the top layer in a multi-layer case must be optically thin ($\tau_{10.8\mu\text{m},\text{abs}} < 4$) and the lower cloud layer must have a temperature which differs considerably from the top cloud layer.

The vertical extent of clouds must vary more than several hundreds of meters within the $1 \times 1 \text{ km}^2$ IFOV of the AVHRR to have significant impact on the estimate of the cloud temperature.

Partly cloudy scenes do occur at any scale, also at the scale of an AVHRR pixel. In the conceptual model, which will be presented in chapter 3, partly cloudy scenes are approximated by homogeneous plane parallel clouds of limited optical thickness. The

contribution from the surface is in this concept underestimated and thus the cloud temperature is overestimated.

In this chapter, the physics of radiative transfer in a cloudy atmosphere was discussed in terms of the window channels of the AVHRR. In the next chapter, analysis methods are presented for the identification and characterization of cloud fields from satellite. The radiative transfer models, which are used for quantitative analysis of shortwave and longwave radiances, are introduced.

References

- Auer, A.H. and D.L. Veal, 1970: The dimensions of ice crystals in natural clouds. *J. Atmos. Sci.*, 27, 919-926.
- Boers, R., A. van Lammeren and A. Feijt, 2000: Accuracy of cloud optical depth retrievals from ground based pyranometers. *Atmos. and Ocean. Techn.* (accepted).
- Bowker, D.E., R.E. Davis, D.L. Myrick, K. Stacy and W.T. Jones: Spectral reflectances of natural targets for use in remote sensing studies. NASA Rep. 1139, p181.
- Cahalan, R.F., W. Ridgeway, W.J. Wiscombe, S. Gollmer and Harshvardhan, 1994: Independent pixel and Monte Carlo estimates of Stratocumulus albedo. *J. Atmos. Sci.*, 51, 3776-3790.
- Cahalan, R.F. and J.H. Snider, 1989: Marine StratoCumulus structure. *Remote Sens. Environ.* 28, 95- 107.
- Coley, P.F. and P.R. Jonas, 1996: The influence of cloud structure and droplet concentration on the reflectance of shortwave radiation. *Ann. Geophys.*, 14(8), 845-852.
- Davies, R., 1978: Effect of finite geometry on the three-dimensional transfer of solar irradiance in clouds. *J.A.S.*, 9, 1712-1725.
- Deirmendijan, D., 1969: Electromagnetic scattering on spherical polydispersions. American Elsevier, New York.
- Descloîtres, J. F. Parol and J. Buriez, 1995: On the validity of the plane-parallel approximation for cloud reflectances as measured from POLDER during ASTEX. *Ann. Geophys.*, 13, 108-110.
- Feigelson, E.V. (editor), 1984: Radiation in a cloudy atmosphere, Reidel etc., Dordrecht

- Gesell, G, 1989: An algorithm for snow and ice detection using AVHRR data: An extension to the APOLLO software package, *Int. J. Rem. Sens.*, 10, 897-905.
- Haan, J.F. de, P. Bosma and J. Hovenier, 1987: The adding method for multiple scattering calculations of polarized light. *Astron. Astrophys.*, 131, 371-391.
- Han, Q., W. B. Rossow and A. A. Lacis, 1994: Near-global survey of effective droplet radii in liquid water clouds using ISCCP data. *J. of Clim.*, 7, 465 – 497.
- Hess, M., R.B.A. Koelemeijer and P. Stammes, 1998: Scattering matrices of imperfect hexagonal ice crystals. *J. Quant. Spectrosc. Radiat. Transfer*, 60, 301-308.
- Hess, M., P. Stammes and R. Koelemeijer, 1997: Scattering matrices of ice crystals. KNMI Scientific Rep. 97-07, KNMI, Bilthoven
- Hess, M. and M. Wiegner, 1994: COP: A data library of optical properties of hexagonal ice crystals. *Appl. Opt.*, 33, 7740-7746.
- Heymsfield, A.J. and C.M.R. Platt, 1984: A parametrization of the particle size spectrum of ice clouds in terms of the ambient temperature and the ice water content, *J. Atm. Sci.*, 41, 846-855.
- Jolivet, D., 1999: Etude de l'influence de l'heterogeneite des nuages sur le champ de rayonnement solaire reflechi vers l'espace. Univ. of Lille, France.
- Knap, W.H., M. Hess, P. Stammes, R.B.A. Koelemeijer and P.D. Watts, 1999: Cirrus optical thickness and crystal size retrieval from ATSR-2 data using phase functions of imperfect hexagonal ice crystals. *J. Geophys. Res.*, 104 (D24), 31, 721-31,730.
- Koelemeijer R. B. A., P. Stammes and A. Feijt, 1995: Cloud optical thickness retrieval from AVHRR-data. *Proc. Symposium on Atmospheric Sensing and Modelling II*, SPIE vol. 2582, 284-293.
- Kriebel, K.T., R.W. Saunders and G. Gesell, 1989: Optical properties of clouds derived from fully cloudy AVHRR pixels. *Contrib. Atmos. Phys.*, 62, 165-171.
- Lacis, A.A. and J.E. Hansen, 1974: A parametrization of the absorption of solar radiation in the earth's atmosphere. *J. Atmos. Sci.*, 31, 118-133.
- Lammeren, A.C.A.P. van, H.W.J. Russchenberg, A. Apituley, H. ten Brink and A.J. Feijt. CLARA: a data set to study sensor synergy, *Proceedings of the Workshop on 'Synergy of Active Instruments of the Earth Radiation Mission*. November 12-14, GKSS Research Center, Geesthacht, Germany, 1998.
- Lammeren A.C.A.P. van, and A.J. Feijt, 1997: Cloud research in the Netherlands: CLARA, *Change*, 34, NRP, Bilthoven, 10-13.

- Macke, A., J. Muller and E. Raschke, 1996: Single scattering properties of atmospheric ice crystals. *J. Atmos. Sci.*, 53, 2813-2825.
- Macke, A., 1994: Modellierung der optische Eigenschaften von Cirruswolken, Ph. D. Thesis, 98pp. Univ. Of Hamburg, Germany
- Marshak A., A. Davis, W. Wiscombe and R. Cahalan, Radiative effects of sub-mean free path liquid water variability observed in stratiform clouds. *J. Geophys. Res.*, 103, D16, 19,557-19,567, 1998.
- Minnis P., D.P. Graber, D.F. Young, R.F. Arduini, Y. Takano, 1998: Parametrization of reflectance and effective emittance for satellite remote sensing of cloud properties. *J.A.S.*, 55, 3313-3339.
- Minnis P., W.L. Smith Jr., D. P. Garber, J.K. Ayers and D.R. Doelling, 1995: Cloud properties derived from GOES-7 for the spring 1994 ARM intensive observing period using version 1.0.0 of the ARM satellite data analysis program. NASA RP 1366, pp 59.
- Minnis P., K-N Liou and Y Takano, 1993a: Inference of cirrus cloud properties using satellite-observed visible and infrared radiances. Part I: Parametrization of radiance fields, *JAS*, 50, 1279-1304.
- Minnis P., P.W. Heck and D.F. Young, 1993b: Inference of cirrus cloud properties using satellite-observed visible and infrared radiances. Part II: Verification of theoretical cirrus radiative properties, *JAS*, 50, 1305-1322
- Minnis P., 1991: Inference of cloud properties from satellite-observed visible and infrared radiances. Thesis. Univ. Of Utah.
- Mischenko, M.I., J.W. Hovenier and L.D. Travis (editors), 2000: Light scattering by nonspherical particles. Academic Press, San Diego.
- Nakajima, T. and M.D. King, 1990: Determination of the optical thickness and effective particle radius of clouds from reflected solar radiation measurements: I Theory. *J. Atmos. Sci.*, 47 (15), 1878-1893.
- Parol, F., J.C. Buriez, D. Cretel and Y. Fouquart, 1994: Cloud optical thickness retrieval from POLDER measurements during ASTEX. *Atmospheric Sensing and Modeling*, R.P. Santer ed., Proc. SPIE 2311, 90-100.
- Pruppacher, H.R. and J.D. Klett, 1978: Microphysics of clouds and precipitation, D. Reicherl Publ. Co, Dordrecht, Holland, 714pp.
- Salisbury J.W. and D.M. D'Aria, 1992: Emissivity of terrestrial materials in the 8-14 μ m atmospheric window. *Rem. Sens. Environ.*, 42, 83-106.

- Savigny, C. von, O. Funk, U. Platt and K. Pfeilsticker, Radiative smoothing in zenith scattered skylight transmitted through optically thick clouds to the ground, *Geophys. Res. Let.*, 26, 2949-2952, 1999.
- Stammes, P. and A.J.M. Peters (Eds.), 1996: GOME validation at KNMI and collaborating institutes, KNMI Scientific Report WR 96-08, De Bilt
- Stammes, P., 1994: Errors in UV reflectivity and albedo calculations due to neglecting polarisation. *SPIE*, 2311, 227-235.
- Taylor V. and L. L. Stowe, 1984a: Atlas of reflectance patterns for uniform earth and cloud Surfaces from Nimbus-7 ERB. *J. Geophys. Res.*, 89, 5345-5363.
- Taylor V. and L. L. Stowe, 1984b: Atlas of reflectance patterns for uniform earthh and cloud Surfaces (NIMBUS-7 61 days). NOAA Tech. Rep. NESDIS 10, 66 pp.
- Stephens, G.L., 1984: The parametrization of radiation for numerical weather prediction and climate models., *Mon. Weath. Rev.*, 112, 826-866.
- Stephens G.L., 1978: Radiation profiles in extended water clouds. Part II: Parametrization schemes. *J.A.S.*, 35, 2123-2132.
- Suttles et al., 1989: Angular radiation models for the Earth-atmosphere system. Vol I: Shortwave radiation. NASA Ref. Publ. RP-1184, Vol I, 147 pp.
- Suttles et al., 1988: Angular radiation models for the Earth-atmosphere system. Vol II: Longwave radiation. NASA Ref. Publ. RP-1184, Vol II, 87 pp.
- Taylor V.R. and L.L. Stowe, 1984: Atlas of reflectance patterns for uniform earth and cloud surfaces (NIMBUS-7 ERB 61 days). NOAA Tech. Rep. NESDIS 10, 66pp.
- Valk de P., A. Feijt and Roozkrans H., 1998: Cloud field characterization based on meteosat imagery and NWP model data. Proc. of the 1998 EUMETSAT Meteorological Satellite Data Users'Conference, EUMETSAT, Darmstadt,
- Wielicki, B.A., B.R. Barkstrom, E.F. Harrison, R.B. Lee III, G.L. Smith and J.E. Cooper, 1996: Clouds and the Earth's Radiant Energy System (CERES); An Earth observing system experiment. *Bull. Am. Meteorol. Soc.*, 77853-77868.
- Winker, D.M., R.M. Couch and M.P. McCornick, 1996: An overview of LITE: NASA's lidar in-space technology experiment. *Proc. IEEE*, 84, 164-180.
- Wielicki B. and R. Green, 1989: Cloud identification for ERBE radiative flux retrieval. *J. Appl. Meteorol.*, 28, 1133-1146.

3. The AVHRR analysis environment

In the framework of this thesis the AVHRR instrument is used to study the spatial distribution of cloud properties at medium high resolution ($1 \times 1 \text{ km}^2$ sub-satellite). The objective is to combine results with ground based observations to obtain a complete description of the cloud field parameters and their variability. Therefore, cloud observations are the topic of this thesis and not the AVHRR retrieval scheme itself. Nevertheless, the skill of the retrievals are evaluated with ground based measurements from the CLARA campaigns of which two cases are presented in section 5.2. Two studies of combined analysis of satellite and ground based measurements are described in chapter 5.1. The emphasis with respect to the analysis is on daytime, because sunlight is required for the retrieval of optical properties and adds to the quality of cloud detection. The AVHRR analysis can be done automatically. However, for detailed studies the analysis is done supervised in order to ensure and enhance quality. In the following paragraphs the processing environment is described for daytime analysis in supervised mode.

3.1 The satellite instrument

The AVHRR is an instrument on board the NOAA series of operational meteorological polar satellites, which are listed in Table 3.1. The orbits of the satellite are sun-synchronous with a frequency of one full circle per 102 minutes. The satellite altitude is about 800km. The instrument scans across track with maximum amplitude of 55degrees. This implies that the Instantaneous Field of View (IFOV) varies a factor six from nadir to the extremes of the swath. The minimum IFOV is 1.2km at sub-satellite. Although the orbit is categorized 'sun-synchronous', which suggests the same position at local solar time, the viewing geometry changes from day to day due to slight shifts in the orbit of the satellite relative to Earth. The orbits also shift gradually during the lifetime of the satellite (Price, 1991). This drift has considerable impact on the quality of climatologies made on basis of a sequence of polar orbiters (Klein and Hartmann, 1993; IPCC, 1995).

The AVHRR has 5 wavelength channels centered at: 0.6, 0.8, 3.7, 10.8, 11.9 μm . The channels are optimized to measure cloud and surface characteristics with minimum of contamination from other atmospheric constituents (see chapter 2). The spectral response functions of the AVHRR on board of NOAA-14 are given in Figure 3.1.

Number	Overpass time	Launch date
7	Morning	23 June 1981
8	Afternoon	28 March 1983
9	Morning	12 December 1984
10	Afternoon	17 September 1986
11	Morning	24 September 1988
12	Afternoon	14 May 1991
13	Morning	9 August 1993
14	Morning	30 December 1994
15	Afternoon	13 May 1998

Table 3.1: NOAA polar orbiter series.

For quantitative analysis calibration is important. The spectral response function of the instruments is measured before launch (Planet, 1988). There is no on board calibration of the visible channels. The absolute calibration changes abruptly during the launch and gradually in time thereafter. The approach by Che and Price (1992) was adopted for re-calibration of the visible channels of AVHRRs up till number 11 (Koelemeijer, 1995c). The accuracy of the reflectivities after re-calibration is estimated to be about 10%. For NOAA 14 the coefficients provided by Rao and Chen (1995) are used. Recently NOAA/NESDIS set up an Internet site, on which new calibration coefficients are available each month (<http://www2.ncdc.nasa.gov/>).

Geolocation of the AVHRR images is a topic of research itself. The difference between pre-calculated and actual position of an IFOV at surface level can be as much as 30km. Algorithms for automatic repositioning have been developed to reduce the positioning uncertainty (Bordes et al., 1992). At KNMI the positioning is made more accurate by interpreting the Dopplershift in the received signal. However, for exact positioning still some cloud free scenes and the human eye are required, than a typical accuracy of 3km is obtained.

3.2 Qualitative analysis of AVHRR radiances

In this paragraph a qualitative description is given of the contribution of surface and atmospheric constituents to the radiances measured from AVHRR. A detailed description of the quantitative cloud property retrievals is given in section 3.3 and further.

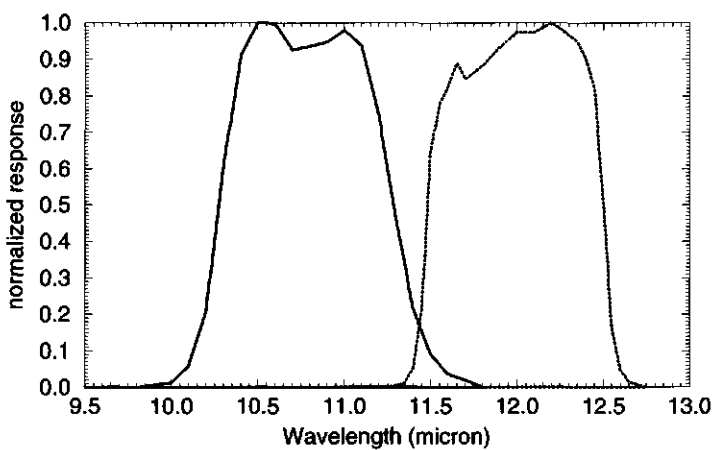
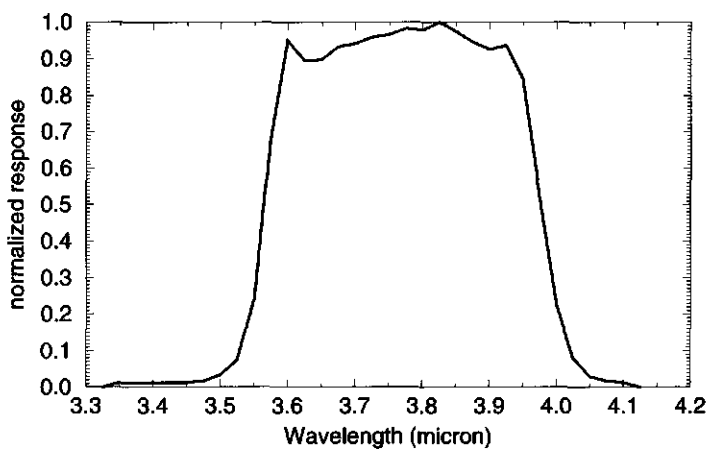
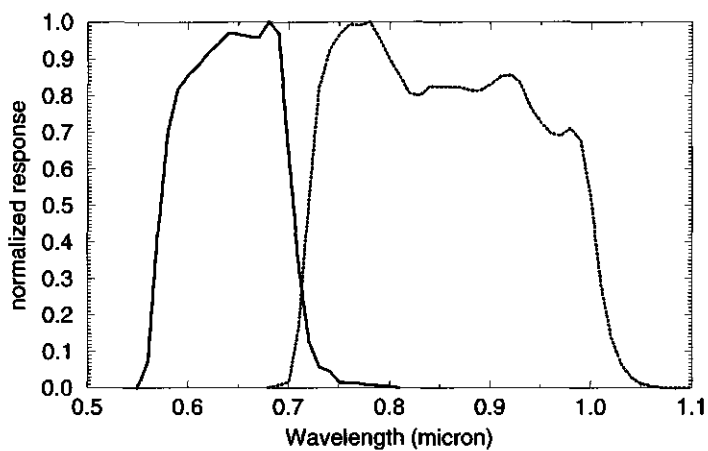


Figure 3.1: Spectral channels of the AVHRR. The visible channels, 0.6 and 0.8 μm (top); near-infrared channel, 3.7 μm (middle) and the infrared channels 10.8 and 11.9 μm (bottom).

The 0.6 μm channel is mainly used for the identification of clouds, because at this wavelength both land and sea surface are dark and clouds are bright. The main contributions from other atmospheric constituents are due to Raleigh scattering, ozone and aerosols.

The 0.8 μm is sometimes used to obtain cloud properties over sea, because the sea is dark and Raleigh scattering can be neglected. However, there are absorption bands of oxygen and water vapor in this wavelength band. The combination of 0.6 and 0.8 μm channels is most frequently used to estimate the amount of vegetation, because sunlight is absorbed efficiently at 0.6 μm but not absorbed at 0.8 μm .

The 3.7 μm channel measures signal both from reflected sunlight and from thermal emission. If the solar contribution can be isolated, the difference with the 0.6 and 0.8 μm channels can be used to estimate droplet size for water clouds (Han et al., 1994; Nakajima and King, 1990). In cloud free conditions snow can be identified (Gesell, 1989). During the night low stratus and fog can be identified from the difference in emissivity at 3.7 and 10.8 μm . The single scattering albedo is relatively high at 3.7 μm and the asymmetry parameter relatively low. Therefore, the emissivity is lower at 3.7 μm than at 10.8 μm .

The 10.8 μm channel is most appropriate to estimate the temperature of clouds and surface. The channel is located in the middle of the atmospheric window and thus atmospheric absorption is at a minimum, but not negligible.

The 11.9 μm channel is mainly used to estimate the atmospheric absorption in the 10.8 μm channel. At 11.9 μm the atmospheric absorption is slightly higher due to a water vapor band and CO_2 . Therefore, the atmospheric absorption in the 10.8 μm channel can be estimated from the difference of measured radiance with the 11.9 μm signal. This method is widely employed to retrieve sea surface temperatures. This method is not very effective to retrieve land surface temperatures, because the emissivities of land surface at 10.8 and 11.9 μm differ and depend on surface type and vegetation (Salisbury and d'Aria, 1992).

Furthermore, thin clouds can be identified from the different equivalent black body temperatures at 10.8 and 11.9 μm . The wavelength dependence of the imaginary part of the

refractive index causes a significant difference in cloud emissivity at these wavelengths (Minnis et al. 1998). As a result the contribution of the surface radiation to the signal measured at TOA is larger at 10.8 μm than at 11.9 μm , especially if there is a large difference between cloud and surface temperatures.

The qualitative analysis described in this section gives insight into the radiative transfer in cloudy atmospheres at the AVHRR channel wavelength. However, to do quantitative analysis a radiative transfer model is required. In the following section the models employed in the AVHRR analysis environment are presented.

3.3 Radiative transfer model calculations

For the analysis of AVHRR radiances two models are employed:

- Modtran (Moderate resolution transmittance) for longwave radiances
- DAK (Doubling-Adding KNMI) for shortwave radiances.

In this section a description is given how these models are used.

3.3.1 Modtran

Modtran is a widely used narrow band model with a 5 cm^{-1} spectral resolution (Berk et al., 1989; Kneizys et al., 1988). The calculated radiances are weighted with the spectral response functions of the channels under study to obtain the channel signal. Modtran requires vertical profiles of atmospheric constituents and radiative properties of the radiating surface (temperature and emissivity). The radiating surface can be either the earth's surface or a cloud, which can be anywhere in the atmosphere. Modtran includes the vertical profiles of 7 standard atmospheres, but the user can input measured vertical profiles. In the AVHRR analysis environment the vertical profiles of temperature, pressure and humidity obtained from radiosondes are used. To estimate the radiance of an opaque cloud at a specific height, clouds are represented by perfect black bodies in the vertical profiles. This results in a table of cloud height versus radiances in the 10.8 and 11.9 μm channels (Bunskoek et al., 1998). The table is used to interpret the AVHRR measurements. Modtran is constantly under development. The most recent information can be found on internet: <http://www-vsbn.plh.af.mil/soft/modtran.html/>.

3.3.2 DAK

The doubling adding method is an effective way of calculating the transmission and reflection of plane parallel layers of scattering particles (Van der Hulst, 1963). The concept is the accurate calculation of the radiative properties of a thick atmospheric layer starting with the adding of thin atmospheric layers. The method starts with two thin layers of known radiative properties, which are placed on top of each other. The incident light on the top layer is partly reflected and partly transmitted through this layer. The transmitted light illuminates the lower layer that transmits and reflects. The light reflected by the lower layer is incident on the bottom of the upper layer, which induces multiple reflections between the two layers. If the internal reflections are determined with sufficient accuracy the radiation field of the combined layer is determined. Doubling is an efficient way of constructing a thick layer. Each processing step the thickness of the layer is doubled by adding two layers of equal thickness. A detailed description of the fundamentals of DAK is given by Stammes (1994) and De Haan et al. (1987) and references therein.

The DAK model was employed to make a database of monochromatic radiative transfer calculations for a wide range of sun-satellite geometry's and atmospheric conditions. The total database consists of 3 million pre-calculated values, with the following parameters:

Solar zenith angle,	40 intervals of about 2°
Viewing zenith angle,	40 intervals of about 2°
Relative azimuth,	19 intervals of 10°
Surface albedo,	0, 0.1, 0.2 and 0.4
Optical thickness,	0, 0.1, 0.2, 0.5, 1, 2, 5, 10, 20, 50, 100, 200, 500
Cloud types,	water and ice

A number of parameters are common to all calculations. The calculations are done at $0.63\mu\text{m}$, which is the representative wavelength of the channel. In the model, the clouds are single layered, horizontally and vertically homogeneous and have an infinite horizontal extent. The atmospheric profiles resemble a midlatitude summer (MLS) atmosphere (McClatchey, 1972). The surface is assumed to reflect light isotropic.

For the calculations, the cloud layer is defined to be between 1 and 2 km height. The droplet size distribution of the water cloud particles is a gamma distribution with an effective radius of $6\mu\text{m}$ and effective variance of 0.11, resembling the C1 type (Deirmendjian, 1969). The

phase function and scattering efficiency of the distribution are calculated with Mie-theory (De Rooij and Van der Stap, 1984). The phase function is shown in Figure 2.4. The single scattering albedo is 1. A study of the sensitivity of the model revealed that the results are not sensitive to the exact height of the cloud, nor to the exact drop size distribution (Koelemeijer, 1994).

The ice cloud is assumed to be at 7-8km height. The phase function is constructed using the method by Hess et al. (1997), which is ray tracing calculations on imperfect ice crystals. The method is based on ray tracing in perfect hexagons as described in chapter 2. However, at each interaction between photon and ice/air interface, the plane of reflection and refraction is tilted. The tilting is assumed to have the same impact as an imperfection in the ice crystal geometry. The tilt angle is chosen randomly between 0 and 30°. The tilt azimuth angle is chosen randomly between 0 and 360°. The tilting smoothes the strong features in the phase function of hexagons, which are due to their perfect geometry. The size distribution is adopted from Heymsfield and Platt (1984). The phase function is shown in Figure 2.8.

3.4 AVHRR retrievals of cloud properties

The AVHRR analysis environment is called KLAROS, which stands for 'KNMI Local implementation of APOLLO Retrievals in an Operational System.'

KLAROS is a two step approach. In step one, cloudy pixels are identified. The cloud detection part consist of tests, which are adopted from the AVHRR Processing over Land Cloud and Ocean (APOLLO), which was developed in the 1980's (Saunders, 1986; Saunders and Kriebel, 1988). The APOLLO scheme as described in these papers is basically a supervised method. The analysis was based on AVHRR measurements alone and relied on histogram analysis over large areas to obtain estimates of surface properties. In the 1990's the histogram analysis was automated (Kriebel, personal communication). In KLAROS adaptations to the original APOLLO version were made to enable automated retrievals and to improve the quality. Cloud detection is described in detail in section 3.4.1. In the second step, the radiances of cloudy pixels are interpreted in terms of cloud parameters, which is described in section 3.4.2.

3.4.1 Cloud detection

Cloudy scenes are identified with a thresholding method, which tests if the signal in a channel or combination of channels originates from the surface in a cloud free atmosphere. If not, the scene is assumed to be cloud contaminated. Here, the main tests for daytime are presented. A scene is identified cloudy if one of the following conditions is met:

Temperature test:

$$T_{10.8\mu\text{m}} (\text{measured}) < T_{10.8\mu\text{m}} (\text{cloud free}) - \text{temperature_threshold} \quad (3.1)$$

Reflectivity test:

$$R_{0.6\mu\text{m}} > R_{0.6\mu\text{m}} (\text{cloud free}) + \text{reflectivity_threshold} \quad (3.2)$$

Semi-transparency test:

$$T_{10.8\mu\text{m}} - T_{11.9\mu\text{m}} > T_{10.8\mu\text{m}}(\text{cloud free}) - T_{11.9\mu\text{m}}(\text{cloud free}) + \text{semi-transparency_threshold} \quad (3.3)$$

T_λ is the equivalent black body temperature in the spectral channel denoted by λ . R_λ is the reflectivity in the spectral channel denoted by λ .

The crucial part of the temperature test is the estimate of $T_{10.8\mu\text{m}} (\text{cloud free})$. In this aspect APOLLO and KLAROS differ. The estimate of the temperature for cloud free conditions in KLAROS originates from an operational numerical weather prediction model called HIRLAM, the High Resolution Limited Area Model (Gustafsson, 1993), whereas in APOLLO histogram analysis over large areas from the satellite overpass under study is used. The histogram analysis approach assumes that for each analysis area it is possible to identify a cloud free scene, which is representative for cloud free conditions over the whole analysis area. This approach does not work for extended cloud fields or in case of sharp surface temperature gradients due to air mass changes. A more elaborate discussion of this topic is given in chapter 4 for Meteosat analysis. The KLAROS approach uses values from the atmospheric model. As shown in chapter 4.1 for Meteosat analysis this introduces a bias due to the difference between the model surface temperature and the satellite equivalent black body temperature for cloud free conditions (Feijt et al., 1998;1999a). In supervised mode of KLAROS the bias can be estimated from cloud free areas in the satellite data. Derrien et al

(1993) showed that orographic effects at sub-grid scales of the atmospheric model can introduce a significant difference between the model surface temperature and the satellite equivalent black body temperature.

The reflectivity test requires an estimate of the reflectivity for cloud free conditions. In APOLLO this value is also obtained from histogram analysis. In KLAROS the surface reflectivity is estimated from a combination of three sources. 1) histogram analysis of the satellite observations under study. 2) histogram analysis of a recent satellite observation at clear sky conditions 3) a two-year data set of AVHRR radiances collocated with synoptic observations of clear sky.

The semi-transparency test is based on the difference in absorption and scattering properties of water droplets and ice crystals at 10.8 and 11.9 μm (Minnis et al., 1998; Olesen and Grassl, 1985). This results in different optical thicknesses and thus different cloud emissivities and equivalent black body temperatures. Minimum differences occur for cloud free conditions and for opaque clouds, when emissivity in both channels is near unity. The maximum difference is governed by the micro-physical properties of the cloud and the cloud top and surface temperature. The difference is largest for small water spheres and decreases with increasing drop size. For spheres larger than 20 μm the emissivities at 10.8 and 11.9 μm are similar (Minnis et al., 1998). The test is sometimes referred to as cirrus-test, because it is most effective in case of a large temperature differences between surface and clouds, i.e. in case of cirrus. To obtain an estimate of the difference for cloud free conditions, Modtran calculations are done at the appropriate viewing zenith angle on profiles of water vapor and temperature as measured from radiosondes. Main sources of uncertainty in these calculations are:

- surface temperature
- surface emissivity at 10.8 μm and 11.9 μm
- representativeness of the radiosonde profiles

These uncertainties are taken into account in the semi-transparency_threshold, which in general is of the order of 1.5K.

3.4.2 Cloud characterization

KLAROS includes retrievals of the following cloud parameters:

- cloud cover fraction
- cloud top temperature
- optical thickness
- emissivity
- liquid water path

In the following the cloud parameter retrievals are described.

Cloud cover fraction

The ratio of cloudy pixels over all pixels is used as an estimate of the cloud fraction. Implicitly it is assumed that cloudy pixels are fully cloudy, which in general is a robust assumption at the scale of the AVHRR IFOV. Statistical analysis of synoptic observations shows that most observations are either in the 0-1 octas or 7-8 octas range, which results in U or J shaped frequency distributions of cloud cover fraction (Henderson-Sellers and McGuffey 1991; Jonas, 1991). Small cloud amounts of the 1-2 octas range will often be identified as cloud free by KLAROS due to the low contrast with the surface. The near overcast situations generate fully cloudy pixels, which is consistent with the approach. So, for the most frequent cloud conditions the approach yields reliable results. In the less frequent 3-6 octas range of observations there may be a bias. This can be an overestimate, if all partly cloudy pixels are assumed fully cloudy, or an underestimate if the cloud detection tests fail to identify part of the cloudy pixels. However, in most cases, part of the cloudy pixels will be correctly labeled as such, and thus the over- and underestimates will compensate each other largely.

Actually, the retrieved cloud cover fraction is merely a cloud projected area. In general, the cloud fraction seems higher when the clouds are observed from a slanting angle, because the vertical dimension is projected on the horizontal. The difference is not accounted for, because it would require a measure of the cloud vertical extent.

Cloud layer temperature

The basic information used to retrieve cloud top temperature is the measured equivalent black body temperature at 10.8 μ m, which is representative of the cloud layer if the pixel is completely filled with an opaque cloud. However, in case of semi-transparent clouds or partly

cloudy scenes, the measured radiance is a combination from contributions from cloud and surface, which results in an overestimate of the cloud temperature. In KLAROS a method is implemented to obtain an estimate of the temperature of cloud layers by excluding those pixels that are affected by semi-transparency. It uses the difference in equivalent black body temperature at 10.8 and 11.9 μm to detect semi-transparent clouds (see also section 3.4.1.). If the following condition is met, the scene is assumed to be filled with opaque clouds.

Selection test:

$$T_{10.8\mu\text{m}} - T_{11.9\mu\text{m}} < \text{selection_threshold} \quad (3.4)$$

The selection test is similar to the semi-transparency test (equation 3.3). The conditions are better defined, because the surface does not contribute to the signal. So, variability of surface temperature and surface emissivity have not to be taken into account. Furthermore, the atmospheric absorption is limited to the atmospheric layer above the cloud and is, especially for ice clouds, negligible. Therefore, selection_threshold may be chosen smaller than semi-transparency_threshold. In general, selection_threshold is about 1K.

This test yields cloud temperatures from individual pixels. Cloud layers may be identified from frequency analysis. Information on cloud fraction per cloud layer is not available from this method. The retrieved cloud top temperature is measured directly and thus is accurate provided that the atmospheric absorption above the cloud may be neglected. This simple method has proven to be effective both for ice clouds and water clouds as was shown by Koelemeijer et al. (1995a) and Feijt et al. (1999). An example is given in chapter 5. Furthermore, the test can be applied both day and night. During daytime, the cloud temperature can also be retrieved from the optical thickness at 0.6 μm . This approach is described below.

Optical thickness

The retrieval of $\tau_{0.6\mu\text{m}}$ is retrieved from $R_{0.6\mu\text{m}}$. The surface reflectivity is estimated in a similar way as for cloud detection. The database of DAK calculations of reflectivity is searched for the appropriate sun-satellite geometry, cloud type, and surface reflectivity. This results in 12 values of $R_{0.6\mu\text{m}}$, corresponding to 12 values of the optical thickness. The thus obtained pre-

calculated values are compared with the measured reflectivity for each pixel to obtain an estimate of optical thickness at 0.6 μm .

Emissivity

The cloud emissivity can be derived from the optical thickness at 10.8 μm , $\tau_{10.8\mu\text{m}}$, using equation 2.4. The optical thickness in the infrared, $\tau_{10.5\mu\text{m}}$, and the optical thickness in the visible, $\tau_{0.6\mu\text{m}}$, are linked with the efficiency ratio, ξ , which depends on the size of the particles:

$$\xi = \tau_{0.6\mu\text{m}} / \tau_{10.8\mu\text{m,abs}} = \langle Q_{0.6\mu\text{m,scatt}} \rangle / \langle Q_{10.8\mu\text{m,abs}} \rangle \quad (3.5)$$

ξ is 2.4 for the water cloud size distribution that was used in the DAK calculation. For ice crystals the value for large particles, $r > 50\mu\text{m}$, is used: $\xi = 2.0$ (Minnis, 1998). This assumption is consistent with the use of the ray tracing technique to obtain a scattering phase function at 0.6 μm (section 3.3.2), which also requires particles to be large.

Cloud temperature

The cloud temperature can be derived from the emissivity and the estimated contribution of the surface, with a formula analogous to equation 2.3:

$$B_{10.8\mu\text{m}}(T(\text{cloud})) = (B_{10.8\mu\text{m}}(T(\text{measured})) - (1 - \epsilon) B_{10.8\mu\text{m}}(T(\text{surface}))) / \epsilon \quad (3.6)$$

$B_{10.8\mu\text{m}}$ is the radiance of a perfect black body at temperature T filtered by the spectral response function of the AVHRR 10.8 μm channel. The spectral response function is obtained from the pre-flight calibration (Planet, 1988). $B(T)$ can be fit to a second order polynomial of T with sufficient accuracy.

$T(\text{surface})$ is estimated from the numerical weather prediction model surface temperature, T_{nwp} . As described in section 3.4.1. this estimate is significantly biased, particularly for cloud free conditions. For detailed studies the difference between model surface temperature and equivalent black body temperature as measured from satellite is estimated from cloud free areas in the AVHRR image. The temperature difference in cloudy areas is expected to be

between 0 and 30% of that in cloud free conditions, depending on the transmission of sunlight through the cloud.

Liquid water path

The LWP and the optical thickness are both directly related to the drop size distribution:

$$\text{LWP} = \int n(r) \frac{4}{3} \pi r^3 \rho \, dr \quad (3.7)$$

where r the droplet radius, ρ the density of water and $n(r)$ the droplet size distribution. The corresponding optical thickness, τ , is given by equation 2.2. The scattering coefficient, $\langle Q \rangle_{n(r)}$, is the weighted average of contributions per drop size, which yields:

$$\tau = \langle Q \rangle_{n(r)} \int n(r) \pi r^2 \, dr \quad (3.8)$$

The droplet size distribution and the amount of liquid water can be linked to the optical thickness through one single parameter, the effective radius, r_e , (Stephens, 1984):

$$r_e = \int n(r) r^3 \, dr / \int n(r) r^2 \, dr \quad (3.9)$$

Combining equations 3.7, 3.8 and 3.9 yields a relation between τ and LWP:

$$\text{LWP} = \frac{4}{3} \tau r_e \rho / \langle Q \rangle_{n(r)} \quad (3.10)$$

If no information on the drop size is available, $\langle Q \rangle_{n(r)}$ is often assumed to be 2 (Stephens, 1984), which is a good approximation for most typical cloud particle size distributions. For the drop size distribution used in the DAK calculations, $\langle Q \rangle_{n(r)}$ equals 2.14.

To complete the retrieval, the effective radius is estimated. If there is no additional information at hand, the effective radius is assumed to be $10 \mu\text{m}$. This is consistent with the values used by Rossow (WCRP, 1988); Stephens (1984) and Minnis (1991), but inconsistent with the drop size distribution used in the DAK calculations. However, the effective radius for

the LWP retrieval can be chosen independently from the optical thickness retrieval, because the latter is hardly affected by the choice of effective radius (Koelemeijer, 1994). As the drop size distribution depends on cloud type it is difficult to estimate the appropriate value in individual cases.

In the method presented in this chapter, the retrieved cloud parameters resemble the description of the atmosphere as used in the radiative transfer calculations. Therefore, we may expect that the results are sensitive to differences between the conceptual model and the cloud field under study. However, it is not feasible to estimate the errors that will occur from theoretical argumentation alone. Therefore, the skill of the retrieval method is evaluated with ground based observations of cloud fields. In chapter 5 a number of cases are presented.

References

- Bordes, P., P. Brunel and A. Marsouin, 1992: Automatic adjustment of AVHRR navigation. *J. Atmos. Ocean. Techn.*, 9, 15-27.
- Bunskoek D.A., A.C.A.P. van Lammeren and A.J. Feijt, 1998: Temperature corrections on radiation measurements using Modtran 3. KNMI Techn. Rep.-204, KNMI, De Bilt.
- Che, N and J.C. Price, 1992: Survey of radiometric calibration results and methods for visible and near infrared channels of NOAA-7, -9 and 11 AVHRR's, *Rem. Sens. Environ.*, 41, 19-27.
- Coley, P.F. and P.R. Jonas, 1996: The influence of cloud structure and droplet concentration on the reflectance of shortwave radiation. *Ann. Geophys.*, 14(8), 845-852.
- Derrien M., B. Farki, L. Harang, H. Legleau, A. Noyalet, D. Pochic and A. Sairouni, 1993: Automatic cloud detection applied to NOAA-11/AVHRR imagery. *Rem. Sens. Environ.* 46, 246-267.
- Deirmendijan, D., 1969: Electromagnetic scattering on spherical polydispersions. American Elsevier, New York.
- Feijt A., H. ten Brink, S. Jongen, A. van Lammeren and H. Russchenberg, 1999: Validation of cloud parameter retrieval methods with objective ground based measurements. *Phys. Chem. Earth*, 24, 173-176.
- Feijt, A. and P de Valk, 2000: The use of NWP model data in cloud detection from METEOSAT imagery, *Int. J. Rem. Sens.* (accepted)

- Feijt, A. and P. de Valk, 1998: Quantifying the difference between NWP surface temperatures and cloud free satellite apparent brightness temperatures, *Contrib. Atmos. Phys.*, 455-460.
- Gesell, G., 1989: An algorithm for snow and ice detection using AVHRR data: An extension to the APOLLO software package, *Int. J. Rem. Sens.*, 10, 897-905.
- Haan, J.F. de, P.B. Bosma and J.W. Hovenier, 1987: The adding method for multiple scattering calculations of polarized light. *Astron. Astrophys.*, 183, 371-391.
- Han, Q., W. B. Rossow and A. A. Lacis, 1994: Near-global survey of effective droplet radii in liquid water clouds using ISCCP data. *J. of Clim.*, 7, 465 – 497.
- Henderson-Sellers A. and K. McGuffey, 1991: An investigation of the burger distribution to characterize cloudiness. *J. of Clim.*, 4, 1181-1209.
- Hess, M., R.B.A. Koelemeijer and P. Stammes, 1998: Scattering matrices of imperfect hexagonal ice crystals. *J. Quant. Spectrosc. Radiat. Transfer*, 60, 301-308.
- Hess, M., P. Stammes and R. Koelemeijer, 1997: Scattering matrices of ice crystals. KNMI Scientific Rep. 97-07, KNMI, Bilthoven
- Hess, M. and M. Wiegner, 1994: COP: A data library of optical properties of hexagonal ice crystals. *Appl. Opt.*, 33, 7740-7746.
- Heymsfield, A.J. and C.M.R. Platt, 1984: A parametrization of the particle size spectrum of ice clouds in terms of the ambient temperature and the ice water content, *J. Atm. Sci.*, 41, 846-855.
- Hulst van der, 1963: A new look at multiple scattering, Tech. Rep., Institute of Space Studies NASA, New York.
- Intergovernmental Panel on Climate Change, 1995: IPCC Second Assessment Report Climate Change, UNCEP/WMO.
- Jonas P., 1991: Cloud cover distributions and correlations. *J. Appl. Met.*, 31, 732-741.
- Klein, S.A. and D.L. Hartmann, 1993: Spurious changes in the ISCCP data set. *Geophys. Res. Letters*, 20, 455-458.
- Koelemeijer, R., A. Feijt, A. Hulshof and A. van Lammeren, 1995: Cloud properties from the KNMI cloud detection system compared with LITE observations. *Proc. of the 1995 EUMETSAT Meteorological Satellite Data Users'Conference*, EUMETSAT, Darmstadt
- Koelemeijer, R. P. Stammes, and A. Feijt, Cloud optical thickness retrieval from AVHRR data, paper presented at symposium on satellite remote sensing, *SPIE*, 2582, 284-293, 1995

- Koelemeijer, R.B.A., 1995: Calibration of AVHRR channels 1 and 2, KNMI Memo number AO-95-02, De Bilt.
- Koelemeijer, R.B.A., 1994: Nadir reflectivity of a stratocumulus cloud deck at 630nm: a sensitivity study. KNMI report: AO-94-08.
- Macke, A., J. Muller, and E. Raschke, 1996: Single scattering properties of atmospheric ice crystals. *J. Atm. Sci.*, 53, 2813-2825.
- Macke, A., 1994: Modellierung der optische Eigenschaften von Cirruswolken, Ph. D. Thesis, 98pp. Univ. Of Hamburg, Germany
- Marshak A., A. Davis, W. Wiscombe and R. Cahalan, Radiative effects of sub-mean free path liquid water variability observed in stratiform clouds. *J.Geophys.Res.*, 103, D16, 19,557-19,567, 1998.
- McClatchey, 1972: Optical properties of the atmosphere, 3-rd ed., AFCRL-72-0497, Air Force Cambridge Research Labs., 107pp.
- Minnis, P., D. Graber, D. Young, R. Arduini and Y. Takano, 1998: Parametrizations of reflectance and effective emittance for satellite remote sensing of cloud properties. *J. Atmos. Sci.*, 55(22), 3313-3339.
- Minnis P., 1991: Inference of cloud properties from satellite-observed visible and infrared radiances. Thesis. Univ. Of Utah.
- Planet, W.G. (editor), 1988: Data extraction and calibration of TIROS-N/NOAA radiometers. NOAA Techn.Mem NESS 107.
- Price, J.C., 1991: Timing of NOAA afternoon passes. *Int. J. Rem. Sens.*, 12, 193-195.
- Pruppacher, H.R. and J.D.Klett, 1978: *Microphysics of clouds and precipitation*, D. Reichel Publ. Co, Dordrecht, Holland, 714pp.
- Olesen, F.S. and H. Grassl, 1985: Cloud detection and classification over oceans at night with NOAA-7. *Int. J. Rem. Sens.*, 6, 8, 1435-1444.
- Rao, N.C.R. and J. Chen, 1996: Post launch calibration of the visible and near-infrared channels of the Advanced Very High Resolution Radiometer on the NOAA-14 spacecraft. *Int. J. Rem. Sens.*, 17, 14, 2743-2747.
- Rooij, W.A. de, and C.C.A.H. van der Stap, 1984: Expansion of Mie scattering matrices in generalized spherical functions, *Astron. Astrophys.*, 131, 237-248.
- Salisbury J.W. and D.M. D'Aria, 1992: Emissivity of terrestrial materials in the 8-14 μ m atmospheric window. *Rem. Sens. Environ.*, 42, 83-106.

- Savigny, C. von, O. Funk, U. Platt and K. Pfeilsticker, 1999: Radiative smoothing in zenith-scattered skylight transmitted through optically thick clouds to the ground, *Geophys. Res. Let.*, 26, 2949-2952
- Saunders R.W. and K.T. Kriebel, 1988: An improved method for detecting clear sky and cloudy radiances from AVHRR-data, *Int. J. Remote Sensing*, 9, 123-150.
- Saunders, R.W., 1986: An automated scheme for the removal of cloud contamination from AVHRR radiances over western Europe. *Int.J.Remote Sens.*, 7, 867-886.
- Stammes, P., 1994: Errors in UV reflectivity and albedo calculations due to neglecting polarisation. *SPIE*, 2311, 227-235.
- Stephens, G.L., 1984: The parametrization of radiation for numerical weather prediction and climate models., *Mon. Wea. Rev.*, 112, 826-866.
- WCRP, 1988: International Satellite cloud Climatology Project (ISCCP) – Documentation of cloud data. WMO/TD-No.266, 76pp.

4. Cloud detection using Meteosat imagery and Numerical Weather Prediction model data

Meteosat is the operational European geo-stationary meteorological satellite. The high frequency of measurements and its fixed viewing geometry, makes it suitable for analysis of time series. Meteorologists use sequences of Meteosat images to illustrate large scale air mass movements to the public. They use the infrared channel, because the visible channel measures reflected sunlight, which varies with latitude, longitude and time of day, which complicates the interpretation. Obviously, there is no visible image during the night.

The infrared channel signal is closely correlated to the temperature of the radiating surface, which can be the cloud top, the surface or a mixture of sources. As clouds, in general, are colder than the surface, the infrared image shows the cold clouds in contrast to the warm surface. The surface is on average colder in the North than in the South due to insolation differences, but this does not hamper the visual interpretation of the image, because locally the contrast remains. The sequences are used by meteorologists to estimate the speed and magnitude of changes in atmospheric conditions. Quantitative analysis of movements of cloud fields are also made to obtain wind vectors (Schmetz et al., 1995). These wind vector fields are assimilated in the model of the European Center for Mediumrange Weather Forecasting (ECMWF).

In this chapter a Meteosat analysis environment is presented. The Meteosat instrument is described in section 4.1. The methods that are described in sections 4.2 and 4.3 are designed to be used in an operational meteorological environment and in the analysis of data from the Tropospheric Energy Budget Experiment, TEBEX. The applications mentioned favor constant quality for both day and night. Therefore, much effort was spent on optimizing the use of the infrared channel for cloud detection.

Clouds are assumed to be colder than the surface. The first order estimate of the surface temperature was chosen to originate from a numerical weather prediction model, because the model provides a spatial distribution of surface temperatures each hour of the day. It was found that the model surface temperature and satellite equivalent black body temperature represent related, but different physical quantities. Therefore, a method was developed to quantify the difference of the Meteosat equivalent black body temperature and model surface

temperature for cloud free conditions (Feijt and De Valk, 1998). This method was employed to improve the discrimination of cloudy and cloud free scenes. The method and results are described in section 4.2.

The optimized infrared analysis together with tests using the visible channel make up the Meteosat Cloud Detection and Characterization KNMI (Metclock) scheme, which is described in section 4.3. The skill of the scheme was assessed over land and sea over Europe each three hours for 1997.

4.1. The Meteosat instrument

The first Meteosat was launched in 1977. In table 4.1 the launch dates of the satellites are listed. Meteosat is in a geo-stationary orbit at 36,000km distance. The angular speed of the satellite equals the rotation of the earth and thus the sub-satellite point is stable. It is located at about 0 longitude at the equator. The satellite covers Europe and a large part of the Atlantic Ocean. The countries contributing to the Europe's Meteorological Satellite Organisation, EUMETSAT, therefore have a clear view of the current cloud cover and the weather systems that move from the Atlantic Ocean to Europe due to the rotation of the earth.

Number	Launch date
1	1977 November
2	1981 June
3	1988 June
4	1989 March
5	1991 March
6	1993 November
7	1997 September

Table 4.1: The launch dates of the Meteosat series.

Meteosat has a stable viewing geometry. The detection of the edges of the earth disc provides geo-location information that is operationally processed at EUMETSAT. Users are provided with well geo-located data that has a positioning accuracy of about 5km (Diekmann and De Waart, 1992). The instrument consists of three channels, the so-called visible (VIS), infra-red (IR) and water-vapor (WV) channels. The spectral response functions are shown in Figure 4.1. The VIS channel is processed in two spatial resolution modes. Here only the low resolution data is used, which is common to all three channels. The spatial resolution sub-satellite, at the equator, is about 5km. Due to the curvature of the earth the resolution in Europe is about $5 \times 9 \text{ km}^2$.

The Meteosat spins about its axis, which is about parallel to the earth axis of rotation. Each cycle the sensors focus at a different latitude. By changing the orientation of the sensor the latitude observed is gradually changed from the Southpole to the Northpole until the full earth

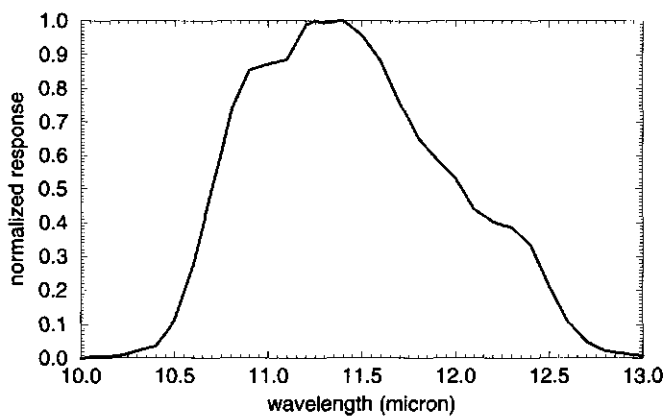
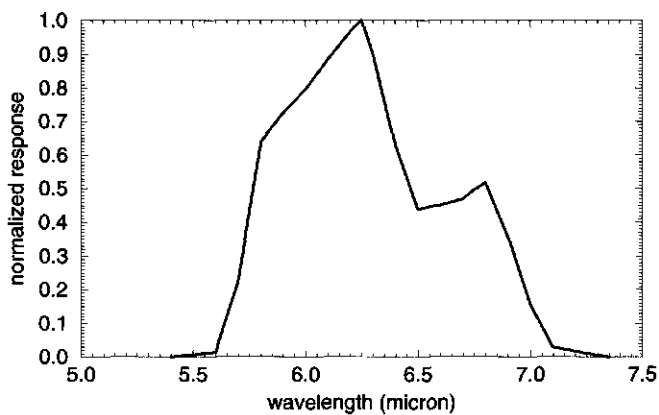
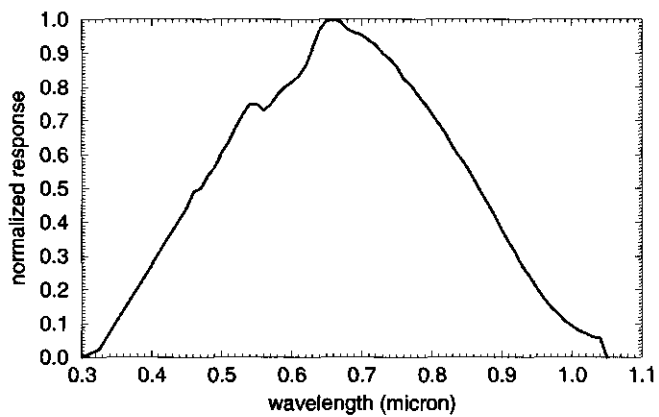


Figure 4.1: Spectral channels of the Meteosat. The visible channels (top); water vapor channel (middle) and the infrared channel (bottom).

disc is scanned. The full disc is completed after 30 minutes and consists of 2500x2500 pixels. The exact time of the measurement depends on the location on earth. The scan starts every half hour in the South. Europe is scanned about 10 to 3 minutes before the whole hour. This matches well with the time of synoptic observations which, according to WMO regulations, are to be made 15-10 minutes before the whole hour.

For quantitative analysis calibration is important. There is no in-flight calibration for the visible channel. There have been various calibration campaigns (Moulin et al., 1996; Desormeaux et al., 1993; Kriebel and Amann, 1993; Koepke, 1982). There is an in-flight infrared calibration instrument. However, until recently this was not used due to technical problems. Calibration was done over known surfaces by matching the signals with radiative transfer calculations.

4.2. The use of NWP model surface temperatures in cloud detection from satellite*

Abstract

An increasing number of satellite cloud detection methods include the use of Numerical Weather Prediction model (NWP) surface temperatures as a threshold for the thermal infrared cloud detection test. The NWP model surface temperature and the satellite apparent brightness temperature are assumed to correlate well for clear sky. Investigations over Europe in April 1997 indicate that the correlation over land is highly dependent on location and time of day. In this paper, it is shown that this variation of the correlation has a distinct impact on the quality of the infrared cloud detection test. As a result, cloud cover fractions which are retrieved using this thermal infrared test are biased by this effect. This can have serious impact on the quality of cloud climatologies, especially with respect to the diurnal variation of cloud cover fraction. A new method is introduced to equalize the quality of the infrared cloud detection test throughout the day. Threshold values are allowed to be smaller than commonly used and therefore the quality of the infrared test is improved. The method may be applied in both climate research and near real-time processing.

***) This section was accepted for publication in this form:**

Feijt A. and P. de Valk, 2000: The use of NWP data in cloud detection from Meteosat imagery. *Int. J. Rem. Sens.* (accepted).

4.2.1. Introduction

In many methods for cloud detection in satellite imagery the surface temperature from atmospheric models is used to define a threshold to the satellite apparent brightness temperature (Derrien et al., 1993; Karlsson, 1996; de Valk et al., 1997). For the future Meteosat Second Generation (MSG), a cloud detection algorithm which includes this test is in preparation (EUMETSAT, 1997). It is assumed that the NWP temperature has a high correlation with the satellite brightness temperature for cloud free conditions. Recent studies by Feijt and De Valk (1998) indicate that the difference between model surface temperature and satellite apparent brightness temperature shows a large spatial and diurnal variation. As a result, the detection efficiency of the infrared test is expected to show the same spatial and temporal signature as the difference between model and satellite temperature. In this paper, this expectation is investigated over Europe in April 1997. The results confirm a distinct diurnal variation in the quality of the infrared detection test. A new method to equalize the detection efficiency of the infrared test throughout the day is tested. The equalization allows for optimization of the threshold values. As a result, the quality of the infrared test was considerably improved.

In section 4.2.2 of this paper, the difference between surface temperatures from the High Resolution Limited Area Model, HIRLAM (Gustafsson, 1993), T_{nwp} , and the satellite apparent brightness temperature measured in the infrared channel of Meteosat-5, T_{sat} , is quantified. Section 4.2.3 describes a method to measure the quality of cloud detection tests. In section 4.2.4, the impact of the variations of the difference of T_{sat} and T_{nwp} , T_{diff} , on the performance of the infrared test is investigated. Section 4.2.5 describes a method to use T_{diff} to equalize the performance of the infrared test throughout the day. Results are interpreted in section 4.2.6. In section 4.2.7, the applicability of the method for use in near real-time applications is described. Conclusions are summarized in section 4.2.8.

4.2.2. The difference between model surface temperature and satellite apparent brightness temperature

In this paper, the results of a study on the difference between model surface temperature and satellite apparent brightness temperature by Feijt and De Valk (1998) are summerized and used here. The area under study is about 25 degrees West to 25 degrees East and 35 to 70 degrees North (Figure 4.2), which corresponds to the area covered by the processing environment for the Meteosat Cloud Detection and Characterization KNMI-scheme, the Metclock-area (de Valk et al., 1997). Cases of cloud free sky are selected from the synoptic observations over land. A synoptic observation is the human estimate of cloud cover following WMO regulations (WMO , 1996, 1997). Each synoptic observation is collocated with an area of 3x3 pixels in the Meteosat image ($15 \times 27 \text{ km}^2$ in the center of our area of study). T_{diff} is calculated for all 9 pixels. For the conversion from counts to temperature we apply the EUMETSAT infrared calibration coefficients, which are provided with the standard infrared product. The HIRLAM grid is about $50 \times 50 \text{ km}^2$. There are about 50 Meteosat pixels collocated with every HIRLAM grid point.

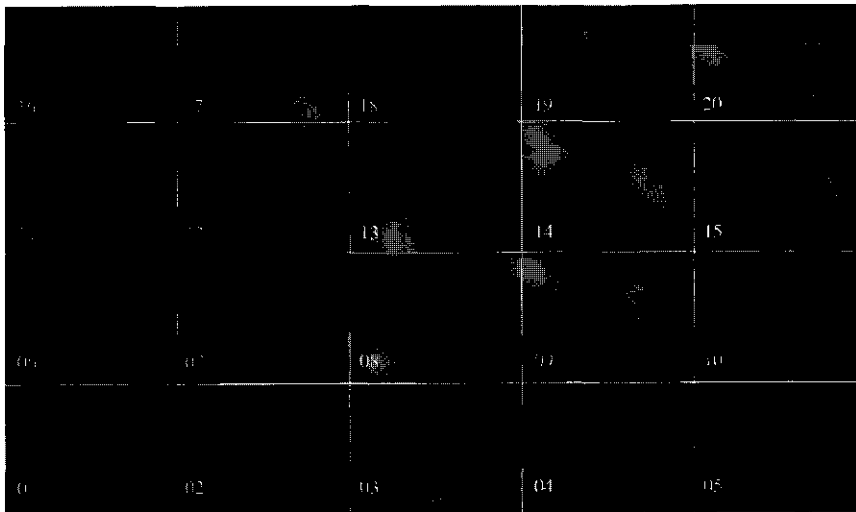


Figure 4.2: The Metclock-area and its segmentation.

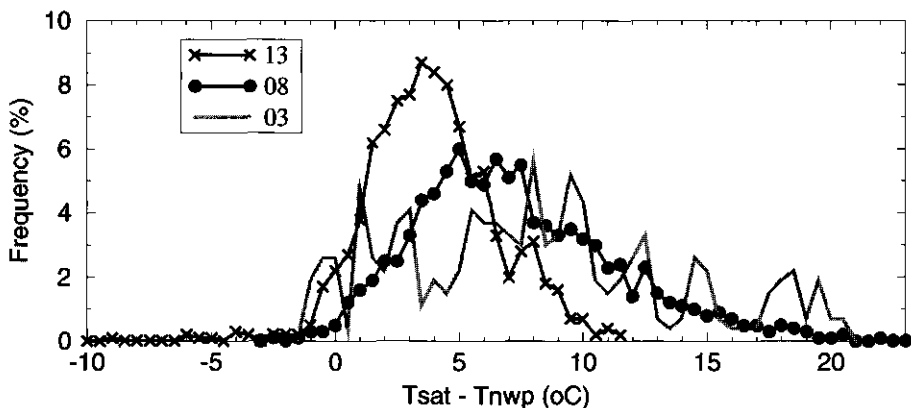


Figure 4.3: Frequency distribution of the difference between T_{sat} and T_{nwp} for April 1997 at 12 UTC for segments 3, 8 and 13.

The Metclock-area is divided into 20 segments, which contain enough synoptic stations, to obtain localized but statistically significant monthly characteristics of T_{diff} over land (Figure 4.2). The median of the frequency distribution of T_{diff} is assumed to be representative of the T_{diff} in a segment. In Figure 4.3 the frequency distributions for April 1997 at 12 UTC for segments 3, 8 and 13 are shown. Segment 3 includes the North African coast and South of

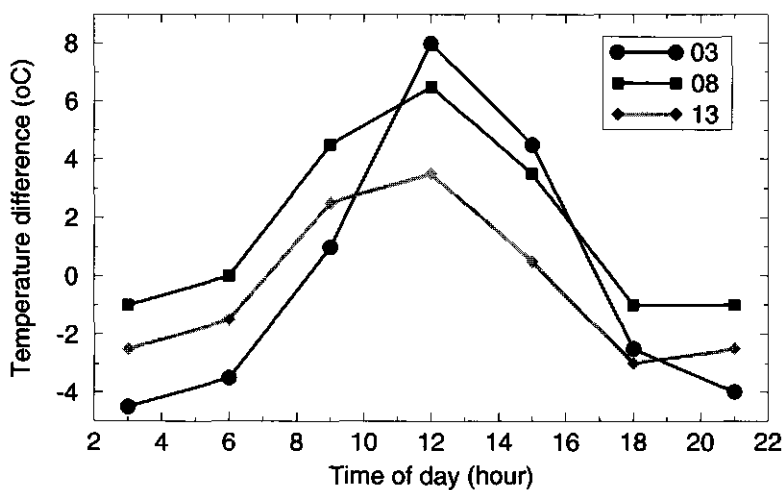


Figure 4.4: Diurnal variation of T_{diff} for segments 3, 8 and 13.

Spain. Segment 8 includes Northeastern Spain and the South of France. Segment 13 includes the North of France, Belgium, the Netherlands and England. Clearly, T_{diff} is higher and the distribution broader at lower latitudes. In Figure 4.4 the diurnal variation of T_{diff} for segment 3, 8 and 13 is shown. T_{diff} for segment 3 ranges from -4.5°C at night up to $+8.0^{\circ}\text{C}$ at noon. The width of the distribution, defined as half the difference between the 84 and 16 percentile temperature differences, ranges from 3°C at night to 6°C at noon. In section 4.2.4 the impact of this diurnal variation on the performance of the infrared test is investigated. In the next section the analysis method will be described.

4.2.3. Measurement method

In this section, synoptic observations of cloud cover over land in Europe are compared to the cloudy/clear sky detection results of the infrared temperature test in Meteosat imagery. The comparisons are made on a three-hourly basis for April 1997 for segments 3, 8 and 13. When making these comparisons, some difficulties are encountered because synoptic observations of cloud cover often have a much larger spatial range than the dimensions of one Meteosat pixel (Barnes J. C. and D. Chang, 1968; Ackerman and Cox, 1981; Schreiner et al., 1993). In paragraph 4.2.3.1 the collocation problem is investigated further. In paragraph 4.2.3.2 a method is introduced to measure the efficiency of cloud and clear sky detection from Meteosat imagery.

4.2.3.1. Collocation

There are three causes of the inaccurate collocation of clouds as reported from synoptic observations and Meteosat pixel positions: 1) mismatch in the geographical coordinates; 2) mismatch in time of synoptic observation and time of satellite measurement; 3) difference in viewing geometry between observer and satellite.

The Meteosat measurements have a spatial inaccuracy of about half a pixel (Diekmann and De Waard, 1992). One pixel is about $5 \times 9 \text{ km}^2$ in Northwest Europe. Furthermore, the synoptic observer is not located exactly in the center of a Meteosat pixel. Therefore, the actual location of the synoptic observation may be shifted by about one pixel in the Meteosat image.

The Meteosat satellite images from Western Europe are available at about six minutes before the hour. The synoptic cloud cover should, according to WMO regulations, be estimated at about 15 until 10 minutes before the hour. The time lapse between synops and Meteosat measurements is about 7 minutes. During this time clouds which move at a speed of 10 m/s will be displaced over a distance of 4 km. The corresponding spatial positioning accuracy of the observed clouds in Meteosat imagery is of the order of half a pixel.

Another source of location mismatch is due to the different field of view of the observer and Meteosat. The field of view of the observer primarily depends on the cloud base height, the cloud fraction, the altitude of the station and the visibility. According to WMO regulations observers should only report clouds if the viewing angle is larger than 10 degrees. This is because, in general, it is not possible to estimate the cloud height accurately at lower viewing angles. Exceptions are made for cumulonimbus, which is always reported, and for low clouds at close range, for which the perspective of features in the landscape enables an accurate estimate of the height. This is illustrated in Figure 4.5. For example, in the case of low stratus, the field of view may only extend over several kilometers. Mid-level clouds may be visible up to a distance of several tens of kilometers. Cumulonimbus may be visible from a distance of a few hundreds of kilometers, which is many times the Meteosat spatial resolution. Obviously, the field of view of the observer is largest in the case of a cloud free sky. In the case of small cloud fractions, some pixels in the vicinity of the synoptic station will contain clouds, while others will be cloud free. For perfect collocation of cloud detection results, it should be

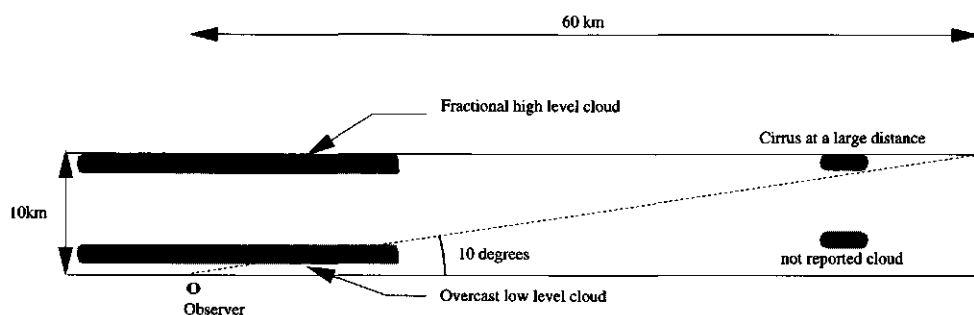


Figure 4.5: Synoptic observational conditions for low clouds and high clouds near by and at a large distance.

known in which Meteosat pixels clouds are observed. Obviously, this information is not at hand. Therefore the probability that a cloud was present in a pixel at a distance from the synoptic station must be estimated.

The number of Meteosat pixels covered by a cloud depends on its location with respect to the Meteosat pixels. For example, one cloud with a physical size smaller than a pixel can extend over four pixels. In conclusion, the relation between cloud fraction and the number of pixels flagged cloudy by a detection scheme is not well defined. From the above it is clear that the largest contribution to the collocation problem is the field of view of the synoptic observer. How this collocation problem effects the definition of the cloud detection criteria is described in the following paragraph.

4.2.3.2. Detection criteria

Detection capability

Each synoptic observation is assumed to correlate to a set of pixels in the Meteosat image, the collocation area. The size of the collocation area depends on the reported cloud cover fraction. The cloud detection test is defined to detect a reported cloud correctly if at least one pixel in the corresponding collocation area is flagged cloudy. The collocation area is chosen as small as possible considering the observed cloud fraction, to prevent an overestimate of the quality of the detection test: e.g. in case of overcast it is probable that all pixels in the vicinity of the synoptic station include clouds. Therefore the minimum size of a collocation area is 1x1 pixel. For small cloud fractions the area is chosen larger to allow for the detection of small amounts of cirrus at a distance from the observer. In the following the synoptic observations are compared with a collocation area in the Meteosat image ranging from 9x5 pixels for cloud free situations to 1x1 pixel for overcast (Table 4.2). The collocation areas should preferably be square. Therefore the collocation areas increase in size with decreasing reported cloud

0	1	2	3	4	5	6	7	8
9x5	5x3	5x3	3x2	3x2	2x1	2x1	1x1	1x1

Table 4.2: Size of the collocation area for each synoptic cloud cover code.

cover fraction: 1x1, 2x1, 3x2, 5x3 and 9x5 pixels. The detection capability, D_c , is the ratio of the number of detected cloudy cases over all collocated reported cloudy cases. Table 4.2.:

Detection efficiency

For most applications the importance of the detection of clouds is proportional to the cloud cover fraction. Overcast situations must be detected, while the detection of small amounts of fair weather cumuli are less important. Therefore the detection capability is weighted with the cloud cover fraction to obtain the detection efficiency, D_e , which is a better measure for the quality of cloud detection tests. The cloud fraction, cf , is derived from the reported synoptic cloud cover code, $sccc$, following Barrett and Grant (1979) and is tabulated in Table 4.3. The detection efficiency is the ratio of the total cloud cover fraction detected and the total cloud fraction observed:

$$D_{e_{cloudy}} = \frac{\sum_{all\ observations} D_c(sccc) * cf(sccc)}{\sum_{all\ observations} cf(sccc)}$$

Another measure of the quality of a detection test is the efficiency of the detection of cloud free area, $D_{e_{clear}}$, which is the fraction of pixels not flagged cloudy in collocation areas of cloud free observations. The infrared test performs perfectly if both $D_{e_{cloudy}}$ and $D_{e_{clear}}$ are 100%.

0	1	2	3	4	5	6	7	8
0	0.0625	0.219	0.375	0.5	0.625	0.781	0.938	1

Table 4.3: Cloud fraction for each synoptic cloud cover code.

4.2.4. Impact of the difference between T_{nwp} and T_{sat} on the detection efficiency

Pixels are flagged cloudy in the infrared test if: $T_{sat} < T_{nwp} - \text{threshold}$. In most algorithms, this threshold is constant over the day and over a large area. In this section, it is shown that the diurnal variation of the difference between model surface temperature and satellite apparent brightness temperature, T_{diff} , has significant impact on the performance of the infrared test.

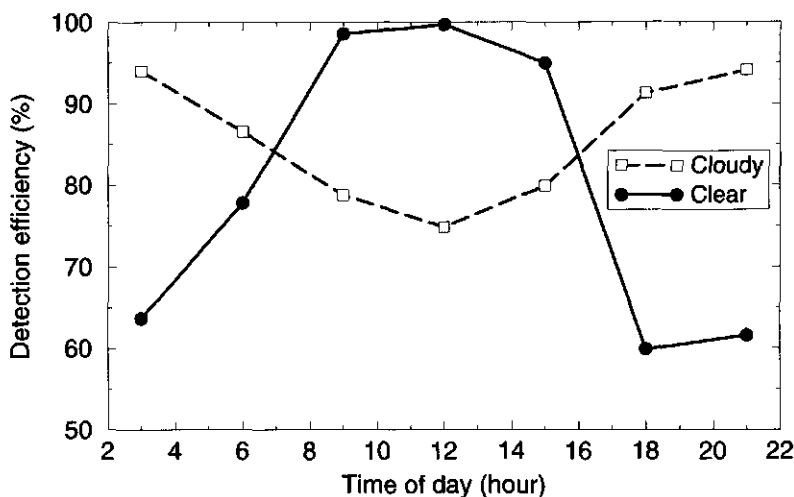


Figure 4.6: Diurnal variation of De_{cloudy} and De_{clear} for segment 8 April 1997 when a fixed threshold of 4.5°C is applied.

In Figure 4.6, the detection efficiency of the infrared temperature test is presented for April 1997 segment 8. Validation is done on a three-hourly basis. Due to gaps in the acquisition of Meteosat data there are no results for 0 UTC. The threshold is set to 4.5°C . The De_{cloudy} ranges from 75% at 12 UTC to 95% at 21 UTC. De_{clear} ranges from 99% at 12 UTC to below 60% at 18 UTC. De_{clear} shows the same diurnal variation as T_{diff} (Figure 4.4), while De_{cloudy} shows the inverse signature. The signature is a result of the diurnal variation of the correlation between model surface temperature and satellite apparent brightness temperature and not of the choice of the threshold.

In Figure 4.7a and b the detection efficiencies for threshold values from 2.5 to 10°C are shown for April 1997 segment 8. The detection efficiency of the infrared test clearly shows a diurnal variation irrespective of the threshold value. As a result, cloud cover fractions which are retrieved using this thermal infrared test are biased by this effect.

The diurnal variation of both detection efficiencies result in the retrieval of lower cloud amounts during the day (not many cloudy scenes are classified as clear and not many clear scenes are classified as cloudy) and higher cloud amounts during the night (not many cloudy scenes are classified as clear and many clear scenes are classified as cloudy). This can have serious impact on the quality of cloud climatologies, especially with respect to the diurnal

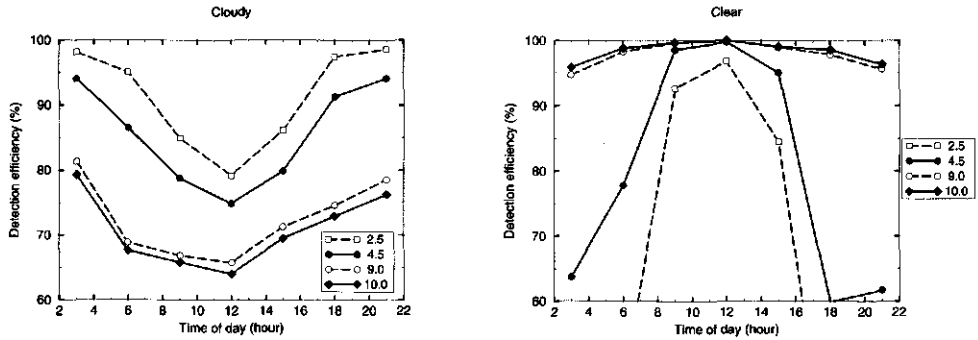


Figure 4.7: Diurnal variation of the detection efficiency for segment 8 April 1997 when a fixed threshold is applied throughout the day ranging from 2.5 to 10.0 °C: a) cloudy cases; b) clear cases

variation of cloud cover fraction. Also in day to day weatherservice practice, a distinct diurnal variation in the detection efficiency is undesirable. In this paper a method is proposed to optimize the performance of the infrared temperature test.

4.2.5. Equalizing the detection efficiency throughout the day

In this section a method is introduced to reduce the diurnal variation of the performance. As stated above, the signature of De_{cloudy} is the inverse of the diurnal variation of T_{diff} . Therefore we propose to include T_{diff} in the threshold; in formula:

$T_{sat} < T_{nwp} - \text{variable_threshold}$, where $\text{variable_threshold} = \text{fixed_threshold} - T_{diff}$. T_{diff} values are obtained for every three hour from statistics over each segment and month as described in Section 4.2.2 (see Figure 4.4). The results of the improved algorithm for April 1997 are presented in solid lines in Figure 4.8. The left hand side, Figure 4.8a shows the diurnal variation of De_{cloudy} for segments 3 (top), 8 (middle) and 13 (bottom). The right hand side, Figure 4.8b, shows De_{clear} . In each figure, the dashed lines show the detection efficiencies with a constant threshold over the day ($T_{diff} = \text{constant}$ in the above equation). Open circles indicate that $\text{variable_threshold}$ is set constant throughout the day to the value at 3UTC, where $\text{variable_threshold}_{3UTC} = \text{fixed_threshold} - T_{diff}(3UTC)$, which for most segments is the diurnal minimum. Open squares indicate that $\text{variable_threshold}$ is set constant to the value at 12UTC, where $\text{variable_threshold}_{12UTC} = \text{fixed_threshold} - T_{diff}(12UTC)$, which for each segment is the diurnal maximum. The curves with open squares are on top in Figure 4.8a, therefore the test yields the best obtainable results for cloudy case

throughout the day for $\text{variable_threshold}_{12\text{UTC}}$. However, the detection of cloud free situations (Figure 4.8b) is unacceptably poor, with De_{clear} below 40% during nighttime.

The open circles are on top in Figure 4.8b, indicating that the test yields the best obtainable results in detection of cloud free situations for $\text{variable_threshold}_{12\text{UTC}}$. However, the detection of cloudy situations is relatively poor (Figure 4.8a). The improved algorithm has the most desirable performance because it has good results for both cloudy and cloud free situations. The performance is nearly constant for segments 3 and 8. Segment 13 shows a concave shape for both $\text{De}_{\text{cloudy}}$ and De_{clear} . It is difficult to further minimize the diurnal variation in both detection efficiencies, because changing threshold values will have opposite effects on $\text{De}_{\text{cloudy}}$ and De_{clear} . Reducing the spread of $\text{De}_{\text{cloudy}}$ will increase the spread of De_{clear} .

4.2.6. Interpretation

For segment 3 and 8 $\text{De}_{\text{cloudy}}$ and De_{clear} show opposite diurnal variations due the difference between model surface temperature and satellite apparent brightness temperature. Therefore both $\text{De}_{\text{cloudy}}$ and De_{clear} can be equalized throughout the day by changing the detection thresholds using an estimate of T_{diff} . The results for segment 13 show a concave shape for both $\text{De}_{\text{cloudy}}$ and De_{clear} . Therefore the diurnal variation cannot be due to the temperature difference alone. In this segment our method can be used to optimize the performance of the thermal infrared cloud detection test, but it is not able to remove the diurnal variation of the detection efficiencies completely.

The method described above has a positive impact on the performance of the infrared temperature test. Still, some improvements can be made especially with respect to the data sampling. The use of synoptic observations of cloud free conditions to obtain information on the correlation between model surface and satellite temperatures sets an upper limit to the obtainable spatial and temporal resolution at monthly values over areas of 150×100 pixels. In some regions with a relatively dense synoptic station network the size of the area or sampling A solution to this sampling problem would be to obtain values at a higher spatial scale, where differences can be resolved within one segment in vegetation, soil type and orography. This would improve the definition of the correlation between model surface and satellite temperature. A possible approach to obtain information at higher spatial resolution could be the use of collocated AVHRR observations. With the AVHRR instrument, a reliable cloud

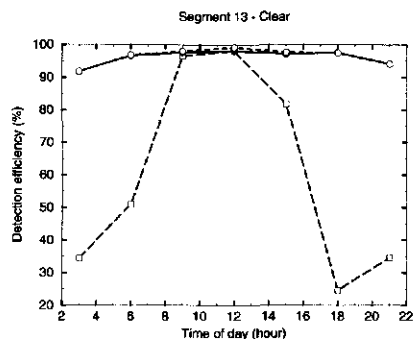
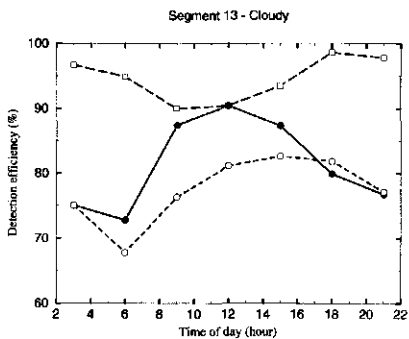
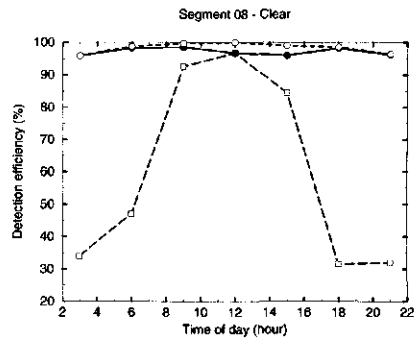
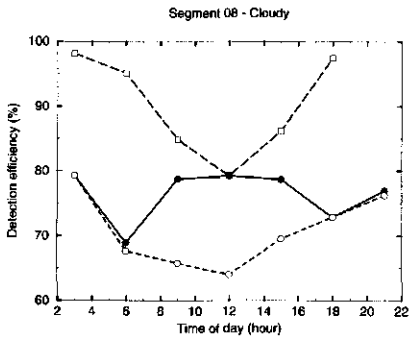
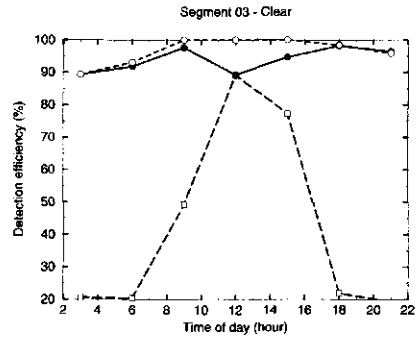
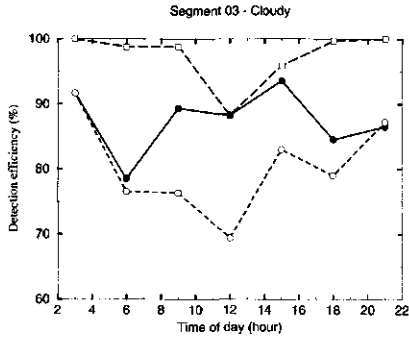


Figure 4.8: Diurnal variation of the detection efficiency for segment 3 (top), 8 (middle) and 13 (bottom) for April 1997, for minimum fixed threshold (open squares, dashed line), variable threshold (filled circles, solid line) and maximum fixed threshold (open circles, dashed line): a) cloudy cases, left; b) clear cases, right

mask could be obtained using a derivative of the APOLLO-scheme (Saunders and Kriebel, 1988, Derrien et al., 1993) at a scale smaller than the Meteosat instantaneous field of view. The correlation between model surface and satellite temperature could be retrieved at the model grid size scale. Unfortunately, in the central part of the Metcloclock-area diurnal sampling is limited, because there are only 4 overpasses of these polar orbiting satellites each day.

Another source of error of the use of synoptic observations is that the quality varies with time of day and region. Especially the synoptic observations of small cloud amounts are less accurate at night than during daytime. However, the situations with high cloud cover fractions, that dominate De_{cloudy} due to their weight in the calculation of De_{cloudy} and their high frequency of occurrence, are relatively well observed during the night. Clear sky observations could be contaminated by situations of small cloud amounts from a distance. However, due to the method of calculation these situations have little influence on De_{clear} .

During daytime there are varying observational conditions, because the optical path of sunlight through clouds depends on the sun elevation. The optical path increases with decreasing sun elevation. Therefore, optically thin clouds can be observed better at dawn and dusk than at noon.

The method presented here in its current form has considerable shortcomings and needs further development. However, it is a tool to optimize the performance of the infrared test. This makes it possible to obtain values for De_{cloudy} between 70% and 90% and values for De_{clear} over 90% throughout the day.

4.2.7. Application in an operational setting

The results shown so far are obtained in an off-line backward processing mode. Therefore T_{diff} can be retrieved from all data for April and then applied to all data for April. So, in the processing of 1 April, data from 30 April is used. In this section the suitability for operational applications is assessed. The month to month change of the correlation between model surface temperature and satellite apparent brightness is investigated. In Figure 4.9a-c T_{diff} for the first 4 months of 1997 is shown.

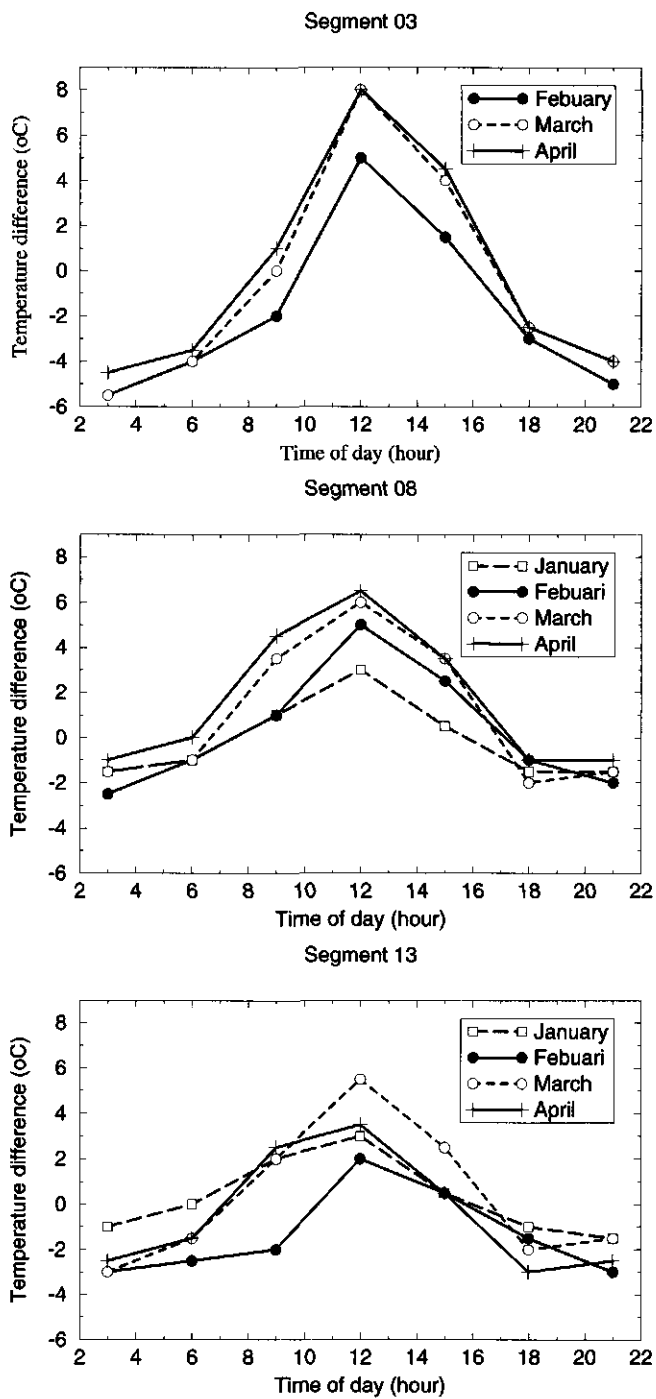


Figure 4.9: Diurnal variation of T_{diff} for segments 3 (top), 8 (middle) and 13 (bottom) for January, February, March and April 1997.

The values for segment 3 in January are missing due to scarce data sampling. The T_{diff} values for segment 3 and 8 show an increasing maximum in time, while the minimum decreases gradually. The correlation between succeeding months is high. For these segments the T_{diff} from the preceding month(s) may be used in defining thresholds for the infrared test in an operational environment. In segment 13 the highest and lowest value at 12 UTC stem from successive months, namely February and March. Therefore the value for February is not representative for March.

In general the diurnal variation of T_{diff} values is much larger than the month to month differences. This observation is supported by the analysis of T_{diff} values for 1996 over an area including segments 13, 14 and the northern parts of segments 8 and 9 (not shown). It was found that the diurnal variation is significantly larger than the month to month changes throughout the year. Therefore, the year average T_{diff} values may be used to optimize the detection efficiencies in an operational environment.

4.2.8. Conclusions

A method is introduced to quantify the difference between model surface temperature and satellite apparent brightness temperature based on synoptic observations of cloud free conditions over Europe for April 1997. The temperature difference shows a distinct diurnal variation with its maximum at noon and its minimum during the night, and a distinct latitudinal variation with minimum values in the North. In cloud detection algorithms the satellite temperature is compared to a model surface temperature in the infrared test. In this paper it is shown that the performance of this test shows a large diurnal variation if one threshold value is applied throughout the day. As a result, cloud cover fractions which are retrieved using this thermal infrared test are biased by this effect. This can have serious impact on the quality of cloud climatologies, especially with respect to the diurnal variation of cloud cover fraction. This observation has a considerable impact on a number of the currently used cloud detection algorithms.

A new method is introduced to optimize the performance of cloud detection using NWP surface temperature data. It is shown that the statistical properties of the measured temperature difference over a month can be applied in the infrared test to equalize and therefore optimize the performance for off-line backward processing. Therefore the method is very suitable for climate research applications. For operational processing, the diurnal

variation of the temperature difference may vary from month to month, but nevertheless retains its diurnal variation. Therefore the method may be applied in near real-time applications, such as for the weather service.

Acknowledgements

We would like to thank Dr. Rose Dlhopsky and Dr. Andre van Lammeren for valuable comments on earlier versions of this paper. Eric Chanvanu is acknowledged for sharing his expert knowledge of synoptic observations. The work presented was partly funded by the Netherlands Remote Sensing Board (BCRS) and the Dutch National Research Program on Global Air Pollution and Climate change (NOP).

4.3 Cloud detection using Meteosat imagery and Numerical Weather Prediction model data*

Abstract

The cloud detection algorithm of the Meteosat cloud detection and characterization KNMI-scheme (Metclock) is introduced. The algorithm analyzes the Meteosat infrared and visible channel measurements over an area from about 25 West to 25 East and 35 to 70 North, encompassing Europe and a small part of northern Africa. The scheme utilizes surface temperatures from a numerical weather prediction model (NWP). Synoptic observations are used to adjust the model surface temperatures to represent satellite brightness temperatures for cloud free conditions. The measured reflected sunlight is analyzed using a minimum reflectivity atlas. Comparison of cloud detection results with synoptic observations of cloud cover at about 800 synoptic stations over land and 50 over sea were made on a three hourly basis for 1997. In total, two million synoptic observations were used to evaluate the detection method. Of the reported cloud cover, Metclock detected: 89% during daytime and 73% during nighttime over land; and 86% during daytime and 80% during nighttime over sea. The fraction of pixels labeled cloud free in reported cloud free conditions was: 92% for daytime and 90% for nighttime over land; and 94% during daytime and 90% during nighttime over sea. The largest contribution to the cloud detection capability is the thresholding of the satellite brightness temperatures with the adjusted model surface temperatures. The cloud detection method is used for the initialization of a short term cloud prediction model and testing of cloud parameterizations of atmospheric models which will be used as an aid to the meteorologists in analyzing Meteosat data.

*) This section was published in this form.

Feijt A., P. de Valk and S. van der Veen, 2000: Cloud detection using Meteosat imagery and numerical weather prediction model data. J. Appl. Met., Vol. 39, No. 7, 1017-1030.

4.3.1. Introduction

Meteosat is a geostationary meteorological satellite that has been operational since the late 1970's. From a technical viewpoint the instrument is old, but many researchers continue working with Meteosat data. The high temporal resolution of 30 minutes, and moderate spatial resolution enable monitoring of fast atmospheric processes, which is extremely important in day to day operational meteorological practice. Furthermore, the technology of these satellites has been preserved over more than two decades, which makes the data suitable for climatological research. In the framework of the International Satellite Cloud Climatology Project (ISCCP), cloud parameters have been derived since 1983 (Rossow and Schiffer, 1991). New parameters derived from Meteosat are still being added to this database (Bishop et al., 1997). Also for real time processing, new applications of Meteosat imagery are still being developed, for example the detection of stratospheric water vapor fields over thick cirrus (Schmetz et al., 1996). Therefore, it is expected that data from this old Meteosat will continue to be used in research even after data from the new instrument, SEVIRI (Woick et al., 1997), becomes available in spring 2001 (scheduled) as part of the Meteosat Second Generation program.

At KNMI, the Meteosat cloud detection and characterization KNMI (Metclock) was developed to suit various applications. The final products, cloud cover fraction and cloud top temperature, are combined with measurements from a network of stations for ground based remote sensing in the KNMI Cloud Detection System (CDS) (Van Lammeren et al., 1999). The aim of the CDS is to reconstruct the 3-dimensional cloud distributions in a form suitable for testing statistical parameterizations of cloud ensembles in atmospheric models, with special attention to sub-grid scale cloud descriptions (Van Meijgaard et al., 1999). The products are also used for the initialization of a short-term cloud prediction model (Van der Veen and Feijt, 1996). In this paper we will focus on the application of the detection scheme in an operational meteorological environment (De Valk et al., 1997). This implies that only historical data can be used and the results must be available in due time. In section 4.3.2 an overview of common approaches to cloud detection is given. The Metclock detection scheme and its ability to discriminate cloudy and clear scenes are presented in section 4.3.3. The validation environment is described in section 4.3.4, and the results for 1997 are presented in section 4.3.5. Conclusions and discussion make up section 4.3.6.

4.3.2. History of cloud detection from Meteosat data

The basic assumptions for most cloud detection algorithms are that clouds are colder and reflect more sunlight than the Earth's surface. The surface properties are derived from frequency analysis of measured reflectivities and temperatures. The surface properties are assumed to be constant over the area of analysis. These methods are well described: asymmetric Gaussian histogram analysis (Simmer et al., 1982); dynamic clustering method (Desbois et al. 1982); hybrid bispectral threshold analysis (Minnis and Harrison 1984a,b,c) and spatial coherence method (Coakley and Bretherton, 1982). The cloud detection results of these methods were intercompared by Rossow et al. (1985). Derivatives of these methods are still being used. For this type of analysis large areas are considered, because it is necessary that within the area of study there is a statistically significant amount of data on both cloud and surface properties. This implies that both surface and cloud properties are derived at low spatial resolution. Furthermore, the results of these algorithms depend on the region and atmospheric conditions (Seze and Rossow, 1991a,b). These statistical methods perform better over ocean than over land.

In the ISCCP cloud algorithm, small areas can be considered because cloud and surface properties are derived from a sequence of images over several days at the same time (WMO, 1988). The spatial resolution is relatively high ($100 \times 100 \text{ km}^2$ over land and $300 \times 300 \text{ km}^2$ over sea). This method is especially suitable for geostationary satellites like Meteosat, because the viewing geometry does not vary from day to day (Wielicki and Parker, 1992). However, the use of statistical information over several days is sensitive to changes of air masses in the 5-10 days period of analysis (Rossow, 1993a, b, c). For climatology purposes this method is sufficiently accurate because these small-scale features average out in monthly average statistics over large areas. For our application however, surface properties at high spatial and temporal resolution are required. Therefore alternate information is used in the Metclock-scheme to estimate the change of surface radiative properties in time and space.

4.3.3. Description of Metclock

The area under study is about 25 degrees West to 25 degrees East and 35 to 70 degrees North encompassing most of the Meteosat B-area, which is widely used by meteorologists in Europe

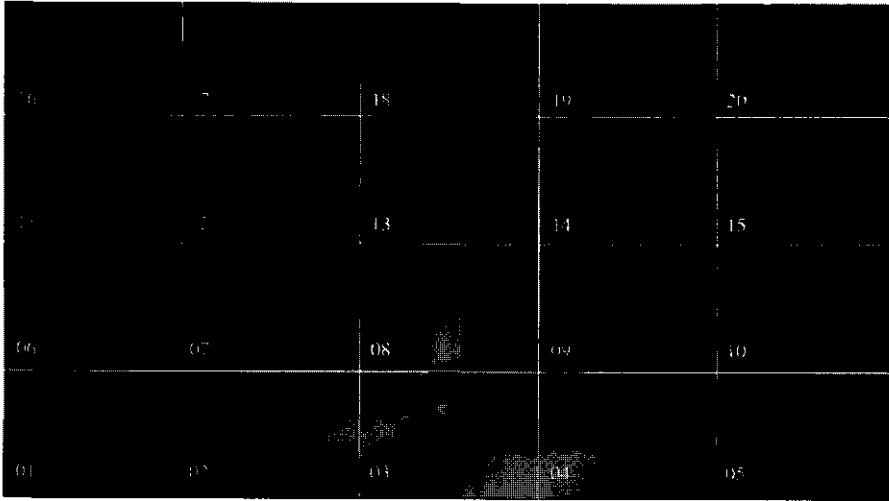


Figure 4.10: The Metlock area and its segments.

(Figure 4.10). The area is divided into twenty segments for analysis. In the algorithm, four surface types are defined: Sea, Land, Coastal (an area of 20km wide on both sides of the coastline) and Mountainous (land of which the pixel averaged height is more than 800m). The height information is obtained from the Gtopo30 database (Gtopo30, 1998). Measurements from both the infrared and visible channel are used in the detection scheme.

The main two tests in the detection scheme are thresholding of the apparent brightness temperature (IR-test) and thresholding the reflectivity (VIS-test). The tests are applied on all pixels. Each test labels a pixel cloudy or cloud free. If a pixel is labeled cloud free for all tests it is detected as cloud free and cloudy otherwise.

4.3.3.1. The IR-test

Discrimination between clear and cloudy pixels is done by comparing the measured brightness temperature with the surface temperature provided by an atmospheric model. For the conversion from counts to temperatures we apply the EUMETSAT infrared channel calibration coefficients, which are provided with the standard infrared products. We use the High Resolution Limited Area Model, HIRLAM (Gustafsson, 1993), which has a 50km horizontal resolution and 32 vertical levels. For our application the main advantages of this model over other models are the relatively high spatial and temporal resolution. Analysis

results are generated every 3 hours and forecast parameter fields are available each hour. In the most simple form, the IR-test is: if the satellite brightness temperature, T_{sat} , is lower than the NWP model temperature, T_{nwp} , by more than a threshold, Δ , then the pixel is labeled cloud contaminated. In formula:

$$T_{sat} < T_{nwp} - \Delta \quad (1)$$

Note, however, that the NWP model surface temperature and the satellite apparent brightness temperature are not expected to match, because neither are representative for the temperature of the radiating surface. The radiation measured from satellite does not match Planck's curve of the surface temperature, because the spectral emissivity of Earth's surface is not equal to unity in the spectral band of Meteosat (Salisbury and D'Aria, 1992; Labed and Stoll, 1991). Furthermore the radiation is affected by atmospheric absorption. The model surface temperature, T_{nwp} , is defined at a lower spatial resolution than the Meteosat measurements (50km versus 7km in the center of the Metclock area), which causes one model value to represent the average temperature of a multitude of surface types and pixels. Furthermore, the model surface temperature is optimized to give correct values for the latent and sensible heat fluxes at the air/surface boundary rather than correct values for the temperature of the radiating surface. As a result there is a temperature difference for clear sky conditions, $T_{dif} = T_{sat} - T_{nwp}$, (Derrien et al., 1993). In the Metclock-scheme T_{dif} is quantified following the method described in detail by Feijt and De Valk (1998, 1999). Thus a pixel is labeled cloud contaminated if:

$$T_{sat} < T_{nwp} + T_{dif} - \Delta \quad (2)$$

There is one threshold value defined per surface type, which is used both day and night and over the whole Metclock area. The thresholds are listed in Table 4.4. A summary is given below of the method we used to quantify T_{dif} .

Cases of cloud free sky are selected from synoptic observations. A synoptic observation is the estimate of cloud cover of a human observer following World Meteorological Organization (WMO) regulations (WMO, 1989, 1996). At the location of a synoptic stations, T_{dif} is derived from 3x3 pixels in the Meteosat image and collocated T_{nwp} values. Detailed checking of the synoptic observations is done to minimize the amount of erroneous synoptic observations in

Surface type	Δ (K)
SEA	4.5
LAND	6.5
COASTAL	10.5
MOUNTANEOUS	8.5

Table 4.4. Threshold values for the IR-test

the analysis. Synoptic stations are not evenly distributed over the Metclock area (see Figure 4.11). Over land there is an elongated area with a high station density which extends from the U.K. to Romania. Over sea we use ship observations, which are largely concentrated around shipping tracks and oil platforms in the North Sea.

In order to obtain a field of T_{dif} values, T_{dif} is derived for each pixel in the Metclock area from the average of T_{dif} values at synoptic stations, which are weighted with the reciprocal of the distance in time and space. Analysis is done for each surface type at every hour of the day on a two-weekly basis. As an example the T_{dif} field over land at noon for two-weekly period in July 1997 is shown in Figure 4.12. In general, the values are higher at lower latitudes. The T_{dif} field is smooth when there are many synoptic observations of cloud free conditions available.

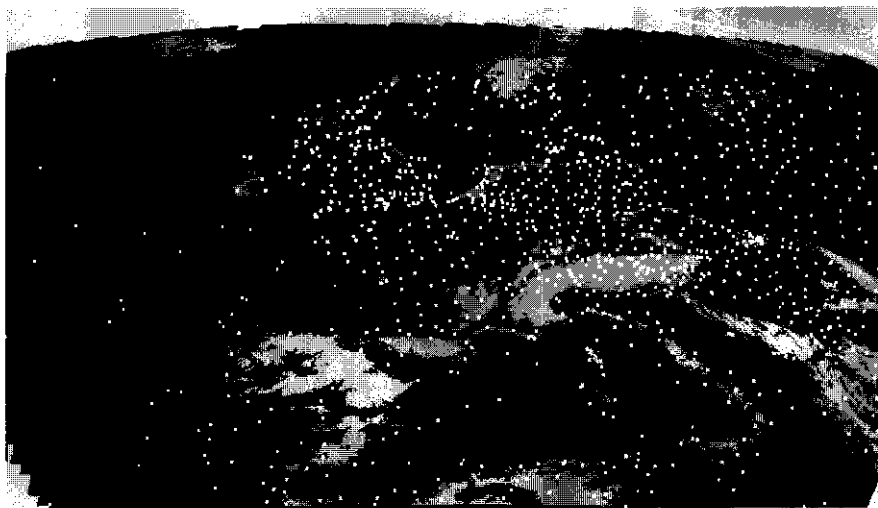


Figure 4.11: Distribution of synoptic stations (white squares) for 10 April 1997. Surface types are indicated: SEA (black), LAND (dark grey), COAST and MOUNTANEOUS (light grey).



Figure 4.12: Spatial distribution of the difference of satellite and model temperatures at 12 UTC for spring 1997. Scaling: dark grey, $-5^{\circ}\text{C} < T_{\text{dif}} < 10^{\circ}\text{C}$, white. Areas without sufficient data are black.

In the Metclock area the maximum values of T_{dif} over land occur in the afternoon and have a median value of 7K in summer. The minimum values occur at the end of the night and have a median values of -3K in summer. In general the diurnal variation of T_{dif} is higher in the South and smaller in the North of the Metclock area. The T_{dif} values thus derived stem from synoptic observations of cloud free situations. The field of view of the observer in cloud free conditions is large and therefore the values are representative for large areas which are cloud free for a long time. In such cases the impact of insolation (and radiative cooling) is at its maximum. Therefore the derived T_{dif} value is biased to extreme values. In cases of alternating cloud free and cloudy conditions T_{dif} is less positive during daytime and less negative during nighttime. In order to obtain a value which is representative for varying cloud conditions we multiply T_{dif} with an empirical factor 0.8. A study for April 1997 (Feijt and De Valk, 1999) shows that the inclusion of T_{dif} in the IR-test yields a remarkable improvement of the cloud detection results over LAND. Especially the diurnal variation of the cloud detection results are reduced considerably.

Over sea it is possible to parameterize the temperature difference between satellite and model temperature because the variability in time and space of surface properties in the infrared is relatively low. We use the parameterization which Singh et al. (1985) developed for AVHRR sea surface temperature retrievals, which correlates the temperature difference to the sea surface temperature and the optical path, e.g. the viewing zenith angle. At 55° viewing angle, which is representative for the Metclock area, the formula reads:

$$T_{\text{dif}} = 23.83 - 0.0978 * T_{\text{nwp}} \quad (3)$$

The remaining difference between model sea surface temperature and satellite brightness temperature for clear sky cases has a standard deviation of about 1K and no significant bias. This implies that the parameterization by Singh is applicable here.

4.3.3.2. The VIS-test

The radiance in the visible channel is converted to scaled reflectivity, R_{sat} , which is the signal in counts (minus the space counts) divided by the cosine of the solar zenith angle. The reflectivity is compared to the surface reflectivity map. The surface reflectivity map is constructed from a time series of two weeks of measured reflectivities and includes a number of tests to increase the chance that the retrieved reflectivity represents a cloud free condition. The IR-test with a high value for Δ is used to identify pixels which are obviously cloudy. These pixels are excluded from the analysis. For each pixel a frequency distribution is generated from which the average, median and the standard deviation is calculated. When the average and median values differ too much, the distribution is assumed to contain values from cloud contaminated pixels. The highest reflectivity value is excluded from analysis. The frequency distribution then is analyzed again. The average value minus the standard deviation is compared to the lowest measured reflectivity. The highest value from these two is accepted as surface reflectivity, R_{surf} . In Figure 4.13, two reflectivity maps are shown. Figure 4.13a shows the values for January 1997 at 12 UTC. The scaled reflectivity values range from 2 to 6 counts in the Mediterranean sea. Bright white pixels indicate the absence of clear sky situations over this time interval. There is a large area which extends over southern Germany to northern Greece where the land is covered with snow, with a scaled reflectivity ranging from 100 to 160 counts. The contrast between land and sea is smaller at higher latitudes partly due to the higher anisotropy of the reflected sunlight over sea compared to land surfaces. Also the larger optical path through the atmosphere at higher latitudes, which causes the scattering by aerosols and molecules to contribute more to the satellite signal, increases the signal over sea and thus decreases the contrast between the dark sea surface and the brighter land surface. The reflection by the Mediterranean Sea is smooth and low. Over the Atlantic Ocean there are structures with higher reflectivity visible which seem to originate from clouds. This suggests that our system failed in generating a surface reflectivity map, but merely generated a

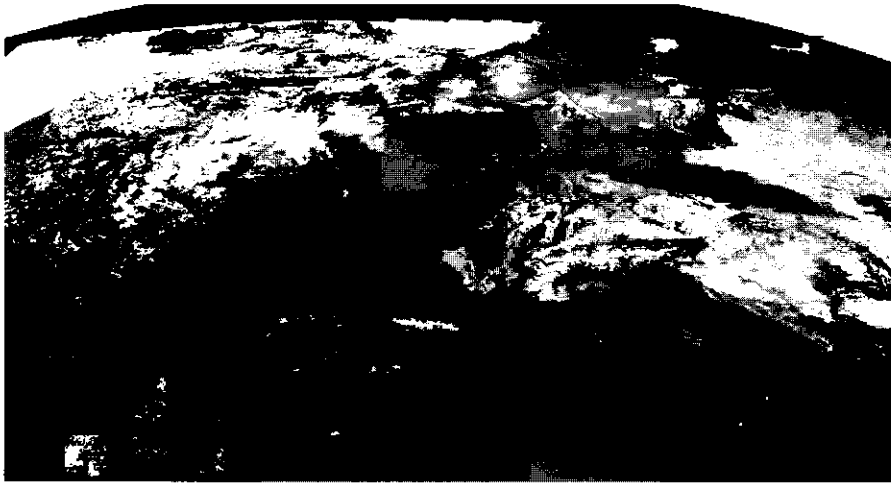


Figure 4.13: Surface reflectivity map at 12 UTC for: a) January; b) July.
Scaling: black, $0 < \text{scaled counts} < 180$, white.

minimum reflectivity map for these cases. The reflectivity map over sea could be improved using histogram analysis over larger areas, because the spatial variability is small. Over land this is not an option due to the high spatial variability. In Figure 4.13b, the reflectivity map for July at 12 UTC, texture features over Spain correlate highly with vegetation and orography.

Also lakes and other small water bodies with low reflectivity can be identified clearly. Over large land areas, like Finland and Poland, there occurred no cloud free situations during the time interval considered.

The VIS-test is the thresholding of the scaled reflectivity to the reflectivity map. A pixel is labeled cloudy if:

$$R_{\text{sat}} > R_{\text{surf}} + 10 + 2 \cos^{-2}(\theta_0) \quad (4)$$

The minimum threshold value is 12, because θ_0 equals 10 degrees for northern Africa at 12 UTC in summer. The maximum value is 56, because the VIS-test is only done when θ_0 is smaller than 78 degrees. In comparison, a perfect reflecting lambertian surface has reflectivity equal to one and scaled reflectivity of about 190 counts. Therefore, in terms of reflectivity the threshold values range from 7% to 30%. The threshold is dependent on the solar zenith angle (θ_0) in order to account for anisotropy effects. If θ_0 is high, the anisotropy is high too (Kriebel, 1978; Koepke and Kriebel, 1978). The exact formula is the result of trial and error.

For each time of day there are 26 two-weekly reflectivity maps per year. In an operational environment only past data can be used, so the age of measurements used to construct the reflectivity map ranges from 1 day to 27 days. This also holds for the T_{dif} fields.

4.3.3.3. Additional tests

In addition to the IR-test and the VIS-test two other cloud detection tests are applied in the Metclock scheme. For the construction of the additional tests we follow the approach of supporting arguments.

In the neighbor-test, the knowledge is used that the chance that the neighbors of a cloudy pixel are also cloudy is relatively large. The neighbor-test is applied only on neighbors of pixels that are classified cloudy in the IR-test. The neighbor-test is similar to the IR-test (equation 2) but with a lower value for Δ , with the result that more pixels are labeled cloudy. The test is expected to improve the detection of optically thin clouds at the edge of cloud fields. Especially frontal zones show gradually increasing optical thickness and emissivity at the edge, which results in gradually decreasing satellite apparent brightness temperatures. If the measured satellite brightness temperature indicates a cloud, there is a high probability that a neighboring pixel contains a cloud of lower optical thickness, which can be detected if the threshold is reduced.

The combined infrared and visible test, termed combined-test, consists of both the IR-test and the VIS-test, but with lower thresholds for both the IR- and VIS-test. The information that the reflectivity is higher than expected for cloud free conditions is used as a supporting argument, which allows a reduction of the threshold in the IR-test. Like the neighbor test, this test is expected also to contribute to cloud detection of small cloud amounts and clouds of small optical thickness, however it can only be applied during daytime.

4.3.4. Validation method

The cloudy/clear sky detection results are compared to collocated synoptic observations of cloud cover. The comparisons are made on a two-weekly and three-hourly basis for 1997. There are large gaps in the acquisition of Meteosat data at 0 UTC for 1997, therefore this time of day is excluded from the validation. There were about 12,000 synoptic observations per two-week period available during daytime (see Figure 4.11) and about 8,000 during the night. Over ocean, synoptic observations from ships are used. There are about 800 observations over sea for each two week period. Because synoptic observations of cloud cover often have a much larger spatial range than the dimensions of one Meteosat pixel, an adjustment must be made before an objective comparison is possible (Barnes J. C. and D. Chang, 1968; Ackerman and Cox, 1981; Schreiner et al., 1993, Karlsson, 1993). Below our approach is briefly described; a full description is given in Feijt and De Valk (1999).

4.3.4.1. Detection capability and detection efficiency

The results of the Metclock algorithm are measured in terms of the detection capability, D_c , and the detection efficiency, D_e . A distinction is made between the efficiency of the detection of cloudy and cloud free areas. For cloudy cases each synoptic observation is assumed to correlate to a set of pixels centered around the location of the synoptic station in the Meteosat image, referred to as the collocation area. A cloud detection test is defined to detect a reported cloud correctly if at least one pixel in the corresponding collocation area is flagged cloudy. The size of the collocation area depends on the reported cloud cover and ranges from 1x1 pixels for overcast situations to 5x3 pixels for situations with small cloud amounts, which corresponds to $5 \times 9 \text{ km}^2$ and $25 \times 27 \text{ km}^2$ respectively, in Central Europe (Table 4.5). The detection capability, D_c , is the fraction of cloudy cases detected per reported cloud cover fraction.

N _{obs}	0	1	2	3	4	5	6	7	8
size	9x5	5x3	5x3	3x2	3x2	2x2	2x1	1x1	1x1

Table 4.5: Size of the collocation area for synoptic cloud cover code.

For most applications the importance of the detection of clouds is proportional to the cloud cover fraction. Overcast situations must be detected, while the detection of small amounts of, for example, fair weather cumuli is less important. Therefore the detection capability is weighted with the cloud cover fraction to obtain the detection efficiency, De , which is a better measure for the quality of cloud detection tests. The observed cloud cover fraction, C_{obs} , is highly correlated with the synoptic cloud cover code, N_{obs} , which is reported by the human observer. However, due to regulations from the World Meteorological Organization there are some distinct differences. For example if the sky is not completely cloud free, the observer must report 1 octa. So, even if there is a cloud cover fraction of only 1% the observer will report 1 octa, which introduces a bias to higher values. Likewise, one single small hole in an overcast cloud field will make the observer report 7 octa, which introduces a bias to lower values. In order to obtain the physical cloud cover fraction from the synoptic cloud cover code we adopted the correlation derived by Barrett and Grant (1979), which is listed in Table 4.6.

N _{obs}	0	1	2	3	4	5	6	7	8
C _{obs}	0	0.0625	0.219	0.375	0.5	0.625	0.781	0.938	1

Table 4.6: Cloud cover fraction for each synoptic cloud cover code.

The detection efficiency is the ratio of the total cloud cover fraction detected and the total cloud fraction observed:

$$De_{cloudy} = \sum_{\text{all cloudy observations}} Dc(N_{obs}) * C_{obs}(N_{obs}) / \sum_{\text{all cloudy observations}} C_{obs}(N_{obs}) \quad (5)$$

Although it is common practice, the quality of a cloud detection algorithm cannot be measured sufficiently by quantifying its capability to detect clouds alone. We also have to quantify its capability to detect cloud free areas. For example: an algorithm which classifies

all pixels cloudy irrespective of the measurements, will have a perfect De_{cloudy} of 100%, but still is not a good algorithm. We therefore define the efficiency of the detection of cloud free area, De_{clear} , to be the fraction of pixels not flagged cloudy in the 9×5 pixels large collocation area of cloud free observations. In formula:

$$De_{clear} = \frac{\sum_{\text{all cloud free observations}} np_{\text{cloud free}}}{(9 \times 5)} \quad (6)$$

where $np_{\text{cloud free}}$ is the number of pixels classified cloud free in the collocation area. Note that there is a difference in the concepts used to measure the detection efficiency for cloudy cases and clear cases. A cloud detection test is perfect if both De_{cloudy} and De_{clear} are 100%.

We compared the results of our validation method to the more common approach to collocate a synoptic observation with one Meteosat pixel irrespective of the cloud cover fraction. The results for both methods are nearly the same. This could be caused by the dominating contribution of (nearly) overcast situations to De_{cloudy} . For (nearly) overcast situations our validation method is the same as the more common approach, because the collocation area is one Meteosat pixel for both methods. The contribution of overcast situations is large due to their high weight in De_{cloudy} and the high frequency of occurrence. Most frequency distributions of cloud cover peak at high N_{obs} , termed J shaped distributions, or at cloud free

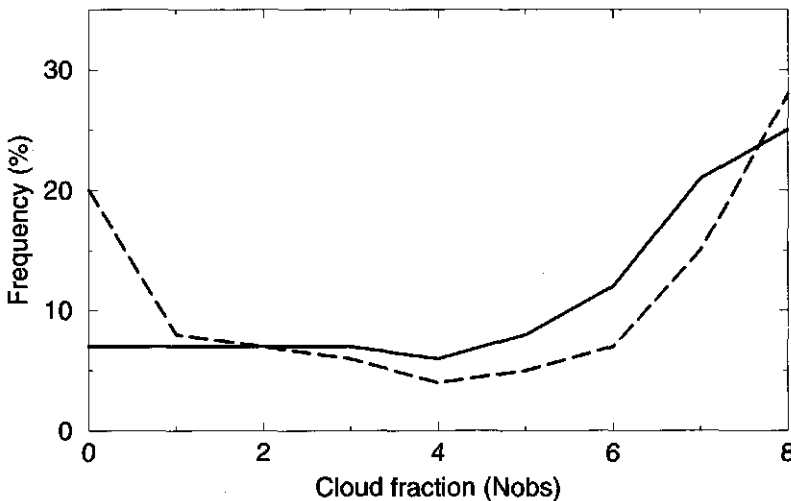


Figure 4.14: Frequency distribution of reported synoptic cloud cover code for 1997 at 12 UTC (solid line) and 21 UTC (dashed line).

and high N_{obs} , termed U shaped distributions, (Jonas, 1991; Henderson-Sellers and McGuffey, 1991). Frequency analysis of the synoptic observations used in our analysis confirm this observation. In Figure 4.14 the annual frequency distributions of N_{obs} over the whole area over all surface types is shown for 12 UTC and 21 UTC. The 12 UTC distribution is clearly J shaped with 3 times more overcast cases than clear cases. At 21 UTC the distribution is U shaped with about equal occurrences of overcast and clear cases. Although the impact on the detection efficiencies is small, we prefer our approach because spatial collocation effects are handled explicitly.

For cloud free conditions, we collocate one synoptic observation with 9x5 pixels, while in the more common approaches a one pixel area is used. The probability that there are unreported clouds in the collocation area increases with its size. Therefore we expect that the results would look better if we would use the more common one pixel collocation area. From our analysis we expect this bias to be below one percent. The advantages of using a large collocation area is the relatively low number of synoptic observations required to obtain statistically significant values and the consistency with the collocation areas for cloudy conditions.

4.3.5. Metclock results for 1997

In this section the cloud detection results of the Metclock scheme for 1997 for the surface types LAND and SEA are presented. The detection efficiency is derived every two weeks for each segment (Figure 4.10). First the results for the two main tests, IR-test and VIS-test, are discussed separately in sub-sections 4.3.5.1 and 4.3.5.2, respectively. The IR-test and the additional neighbor test can be used day and night and are of importance to meteorological practice. However, during daytime optical cloud properties can only be derived from VIS reflectivity. In sub-section 4.3.5.3, the detection efficiencies of the cloud detection scheme using all tests are described. The results over LAND are derived from segments 8, 9, 13 and 14, which encompass Central Europe. Detection efficiencies are derived for each segment and then averaged. To obtain a representative value for the detection efficiencies over SEA we average the results over segments 7, 8, 12 and 13. The number of observations in other SEA containing segments is too low to be statistically significant. The results for COASTAL and MOUNTAINEOUS are not presented because they show large variations with location and therefore cannot be regarded as representative for any coastal or mountainous area. Each

mountain area has its own peculiarities and is worth separate analysis. We prefer to present results which have a wider range of applications and therefore we restrict ourselves to the presentation of results over the surface types LAND and SEA.

4.3.5.1. IR test

In this subsection, we will describe the results of the IR-test in terms of two-weekly averaged detection efficiencies, De_{cloudy} and De_{clear} . From the distribution of two-weekly values the year average and the standard deviation, σ , is calculated for each time of day and presented in one graph to show the diurnal variation. The standard deviation is defined to be the root of the mean of the square of the difference between two-weekly values and the yearly average. The variation of the detection efficiencies throughout the year is also presented. The yearly variation causes part of the spread, as represented by the standard deviation. Therefore the day to day results show a smaller spread.

LAND

Figure 4.15a shows the year averaged diurnal variations of De_{cloudy} and De_{clear} over LAND. The time indicated is UTC, which matches local time for England in the western part of our validation area, but differs 1 hour with Poland in the eastern part. The quality of the detection of cloud free areas is nearly constant over the day: On average De_{clear} is about 95% and σ is 4% for all hours indicating a very stable quality of the detection algorithm with respect to discrimination of cloud free areas throughout the year. The quality of the detection of cloudy areas shows a diurnal variation of 14%. De_{cloudy} ranges from 69% during the night to 82% at noon. The standard deviation is about 7%. The standard deviation is larger during the night than during the day.

In Figure 4.15b the detection efficiencies at 12 UTC over LAND are presented as a function of daynumber since 1 January 1997. There are 5 two-weekly values missing, because not all information used in the Metclock scheme was available during these periods. The broken line indicates a second order polynomial fit to the two-weekly averaged De_{clear} values, which are indicated by circles. The year average value of De_{clear} is 95%. The best results are obtained during spring, 98%. During autumn De_{clear} decreases again to about 90%. The spread is relatively small in the beginning of the year. At day 200 a dip occurs. During this period our data acquisition system failed, so synoptic data were obtained from other sources. The

alternate data was processed with a different quality control mechanism. From day 250 until the end of the year the spread of values is relatively large. We found that also the spread of values in the T_{dif} is relatively large in fall and winter 1997. The source of this deviation is probably the surface parameterization scheme in the HIRLAM operational forecasting model, which is not able to correctly model the surface temperature during short periods of fair weather during autumn, when the surface is wet and there is little vegetation to evaporate the moisture. Investigations over De Bilt show a bias of the modeled screen temperature of several K (Moene, 1998). The impact of this sensitivity of the model is partly compensated

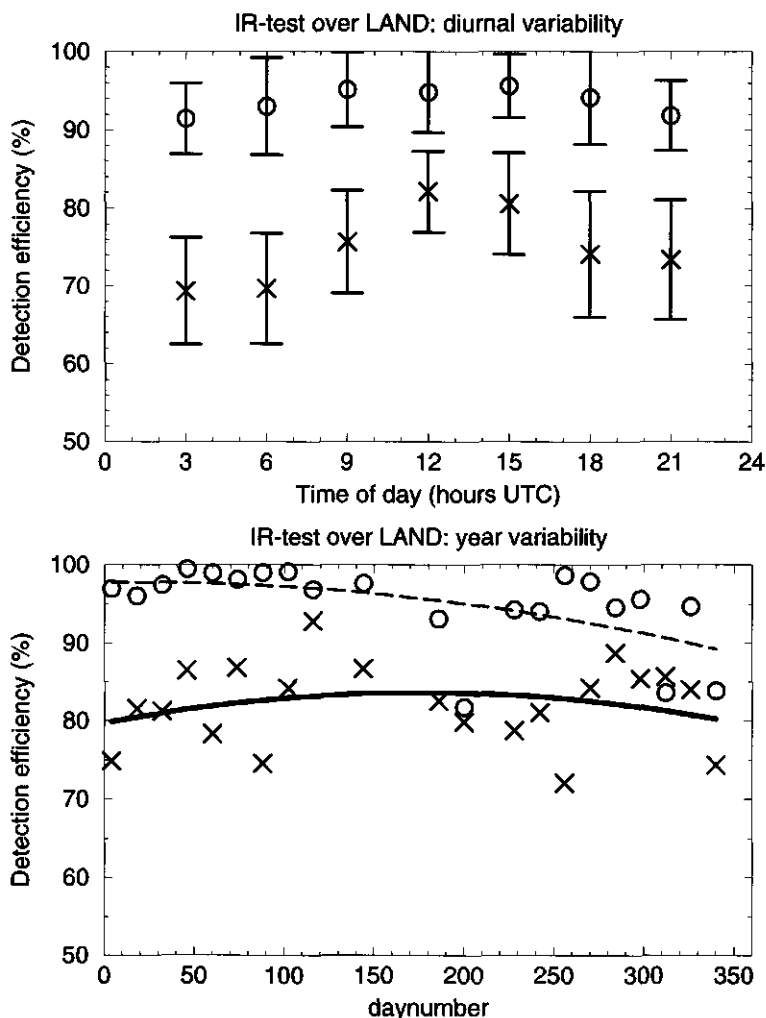


Figure 4.15: De_{clear} (circles) and De_{cloudy} (crosses) for the IR-test over LAND: a) diurnal variability. The bars indicate the standard deviation; b) year variability at 12 UTC: dashed line is the second order fit of De_{clear} values; solid line is the second order fit of De_{cloudy} values.

because the temperature bias is quantified in T_{dif} . However, T_{dif} is calculated for each two week time-interval, so variations in the bias of T_{nwp} at a higher temporal frequency are not compensated. The yearly variation of De_{clear} for the IR-test is not symmetric, the values at the beginning and end of the year do not match. This is probably due to variations in atmospheric conditions from one year to another.

The year average value for De_{cloudy} is 79%, with a standard deviation of 6%. There is no significant change in the quality during the year. Remarkably, the dip at day 200 does not show here. This could be due to the fact that De_{clear} is much more sensitive to the quality of the synoptic observations than De_{cloudy} .

The year variation of detection efficiencies for the IR-test at 3 UTC resemble year variation of the detection efficiencies at 12 UTC described above but with lower values: De_{clear} 90% and De_{cloudy} 66%. This result emphasizes that the IR-test over LAND discriminates cloudy and clear pixels with a constant quality throughout the year irrespective of the time of day.

SEA

Over SEA there are less observations than over LAND and also the quality is lower. Still, the many people who do meteorological observations on ships provide us with valuable

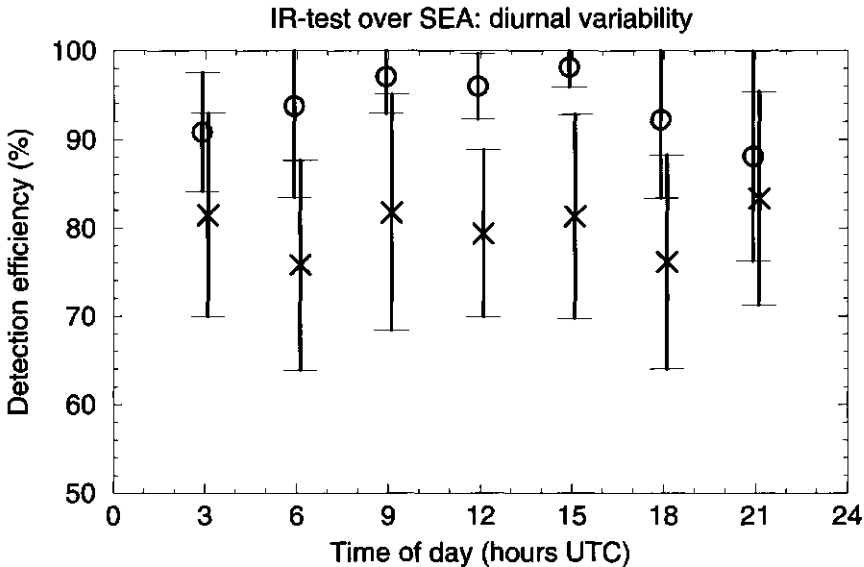


Figure 4.16: De_{clear} (circles) and De_{cloudy} (crosses) for the IR-test over SEA: diurnal variability. The bars indicate standard deviation.

independent comparison material. In Figure 4.16, the diurnal variations of the detection efficiencies of the IR-test over SEA are shown. De_{clear} is about 94% on average and De_{cloudy} 80%. De_{clear} shows a diurnal variation from about 90% at night to about 96% during daytime. There is no diurnal variation in De_{cloudy} . The diurnal variation in De_{clear} could partly be caused by the different observational conditions during day and night. Especially during night over SEA the number of observations is small which makes the validation method extra sensitive to erroneous observations.

At 12 UTC the cloud detection results over LAND and SEA are similar. However, during the night Metclock cloud detection results are better over SEA than over LAND. This was expected, because the surface temperature is much more sensitive to insolation conditions over land surface than over sea surface.

4.3.5.2. VIS test

LAND

The VIS-test is applied if the solar zenith angle, θ_0 , is smaller than 78° . This implies that the applicability depends on the time of year and the geographical location. Figure 4.17a shows the average diurnal variation of detection efficiencies for July 1997. De_{clear} values range from 95% at 6 UTC to 99% at 18 UTC. The σ difference between year average and two-week value is 2 to 4%. The De_{cloudy} is about 65% for all hours except 18UTC. At the boundary between segments 8, 9, 13 and 14 the solar zenith angle at 6 UTC is 20° and at 18 UTC 11° in July, so the 18 UTC values are for the extreme low sun elevation conditions. We find that the relation between threshold value and the solar zenith angle works well, since the detection efficiencies are about constant during daytime. During twilight the threshold becomes so high, that the test loses impact without decreasing De_{clear} .

In Figure 4.17b the detection efficiencies at 12 UTC over LAND are presented for the VIS-test as in Figure 4.15b for the IR-test. The broken line indicates a second order polynomial fit to the two-weekly averaged De_{clear} values, which are indicated by circles. The year average value of De_{clear} is 97%. The changes throughout the year resemble those of the IR-test: from 96% in the beginning of 1997 to 99% in spring, than slowly decreasing to about 95% in

winter 1997. Also in concert with the results of the IR-test, the variability of De_{clear} is small at the beginning, but increases to the end of the year.

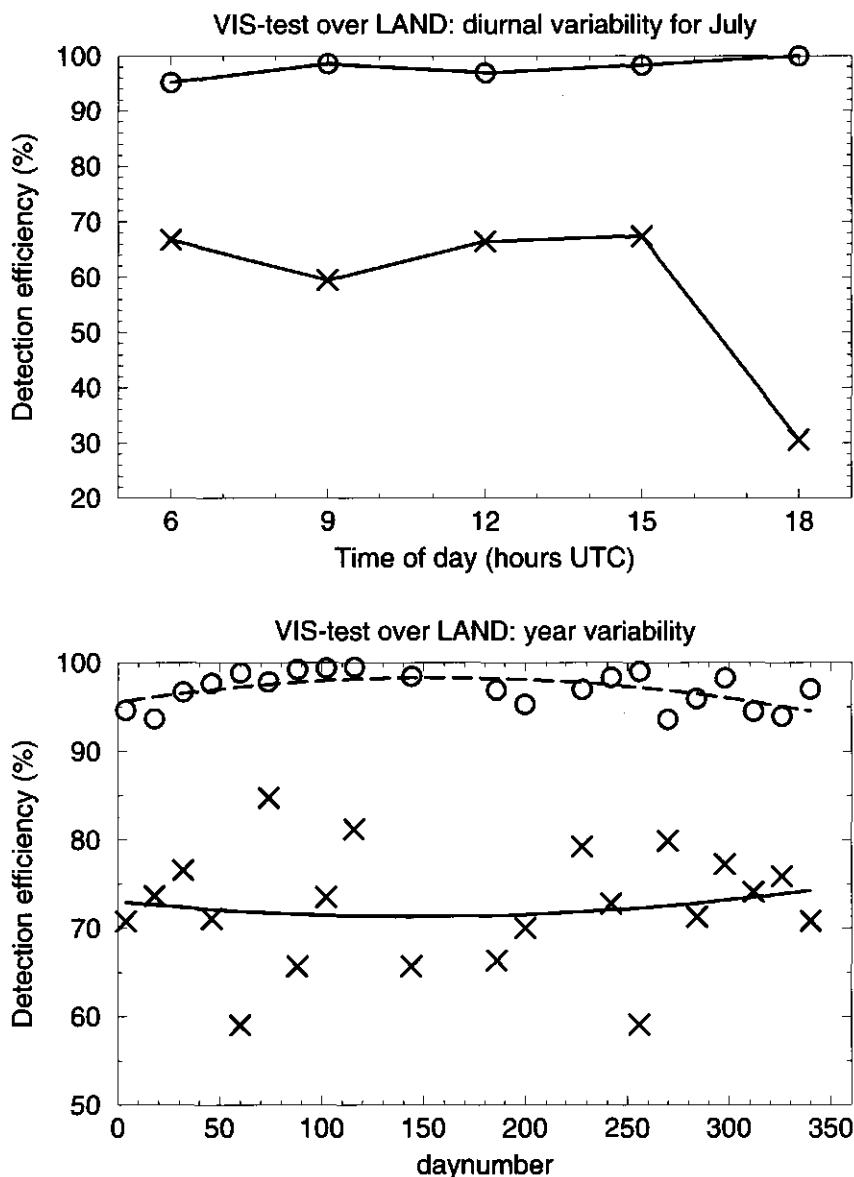


Figure 4.17: De_{clear} (circles) and De_{cloudy} (crosses) for the VIS-test over LAND: a) diurnal variability for July 1997. b) year variability at 12 UTC: dashed line is the second order fit of De_{clear} values; solid line is the second order fit of De_{cloudy} values.

The year average value for De_{cloudy} at noon is 73%, with a σ of 7%. De_{cloudy} shows a large yearly variability, indicated by the distance of the two-weekly values (crosses) from the second order polynomial fit represented by the solid line in Figure 4.17b. The variability cannot be ascribed to the variability of surface reflectivity, because in general this surface property varies relatively slowly. Therefore the results suggest that the quality of the reflectivity map is varying widely. This suggestion is supported by inspection of a number of reflectivity maps. Often the residues of cloud structures appear (like in Figure 4.13b over sea). Furthermore, there are relatively many pixels for which no cloud free situation has occurred during the two week analysis interval, in which case the reflectivity map is not defined (indicated by white pixels in Figure 4.13a and 4.13b). This leaves some room for improvement.

SEA

There is no significant diurnal variation of the detection efficiencies for SEA except for a extremely low De_{cloudy} at 18UTC as was also obtained over LAND (Figure 4.17a). At noon De_{clear} is about 96% on average throughout the year. De_{cloudy} ranges from 70% during summer to 80% at the beginning and end of the year. This signature suggests that the correlation between detection threshold value and solar zenith angle could be improved to make the results more constant throughout the year.

4.3.5.3 Results of total of all tests

The basis for the Metclock-scheme is the IR-test. In this section the contributions of the VIS-test and the additional tests to the cloud detection results for 1997 is described. The presentation is analogous to the previous sections. First the results over LAND are presented than the results over SEA.

LAND

Figure 4.18a shows the diurnal variation. During nighttime the values differ less than 1% from those of the IR-test. De_{clear} varies between 90% and 94% with a standard deviation of 4%. At 12 UTC the VIS-test adds 4% to De_{cloudy} and reduces De_{clear} by 1%. De_{cloudy} has a diurnal variation of 20% due to cumulative impact of the better results for the IR-test during daytime and the use of the VIS- and combined-test. The standard deviation is about 7%.

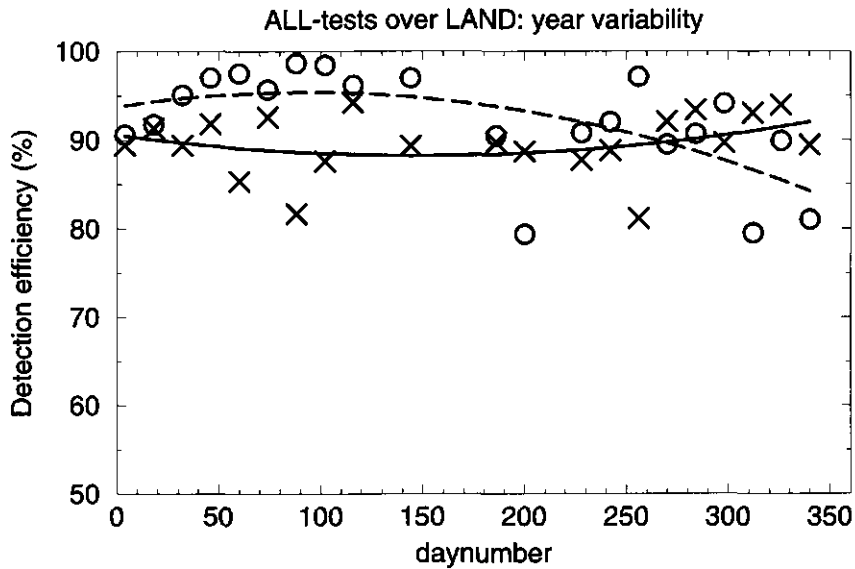
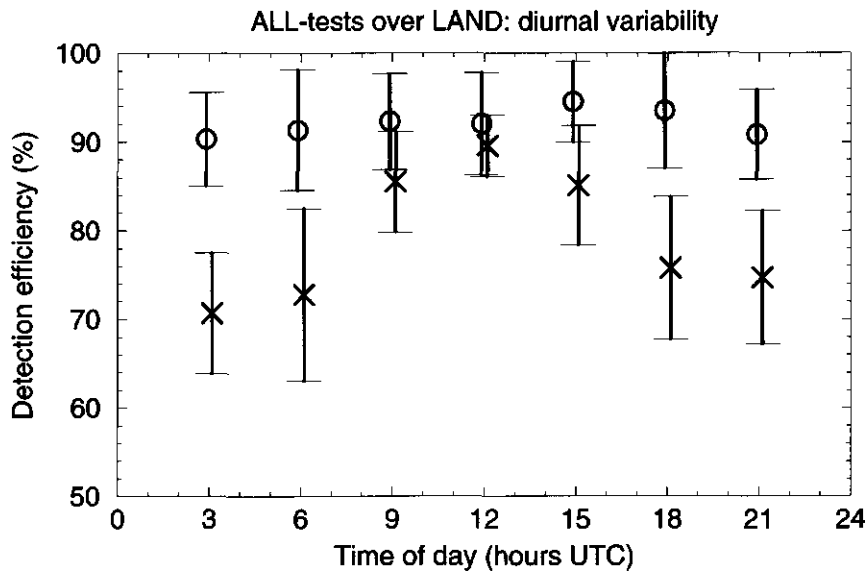


Figure 4.18: De_{clear} (circles) and De_{cloudy} (crosses) for the ALL-tests over LAND: a) diurnal variability. The bars indicate standard deviation; b) year variability at 12 UTC: dashed line is the second order fit of De_{clear} values; solid line is the second order fit of De_{cloudy} values.

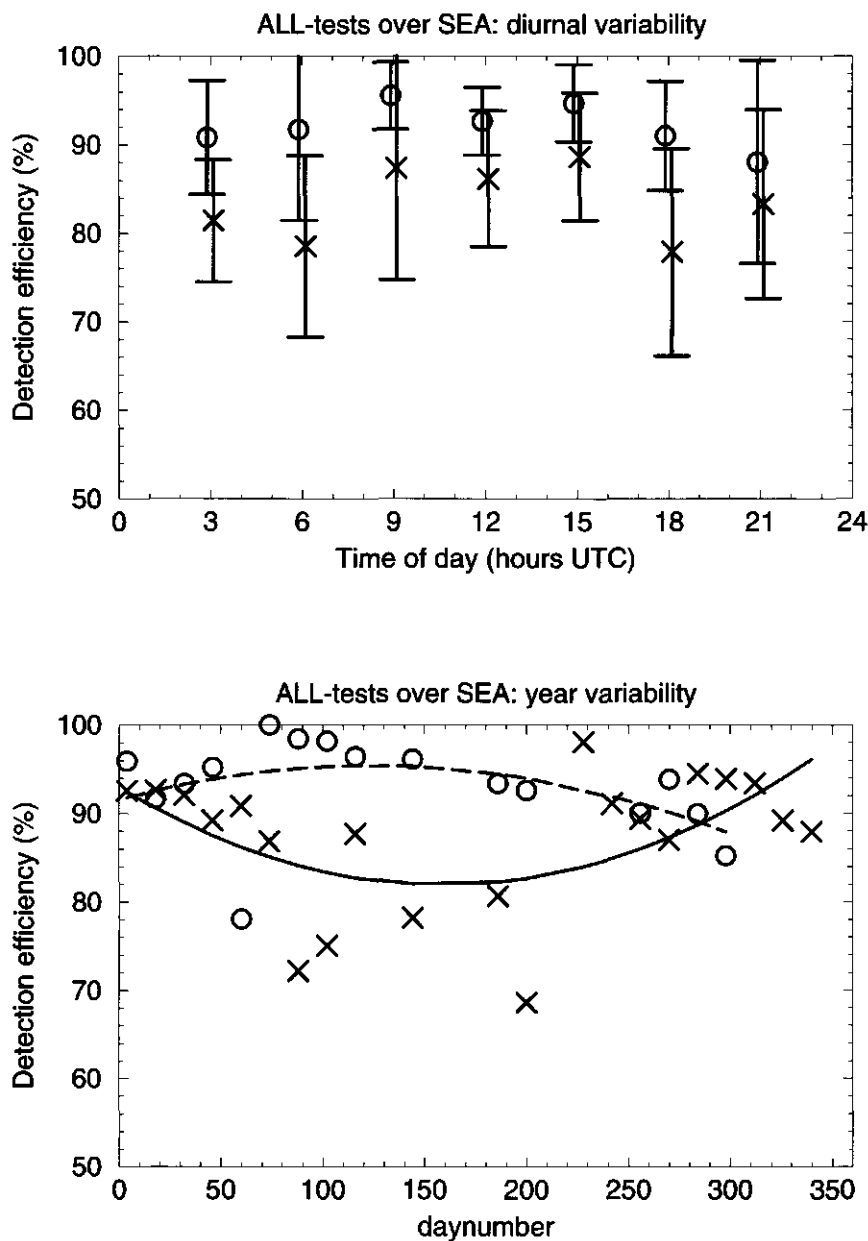


Figure 4.19: De_{clear} (circles) and De_{cloudy} (crosses) for the ALL-tests over SEA: a) diurnal variability. The bars indicate standard deviation; b) year variability at 12 UTC: dashed line is the second order fit of De_{clear} values; solid line is the second order fit of De_{cloudy} values.

In Figure 4.18b the change of the detection efficiencies at 12 UTC during the year are presented for all tests. The De_{clear} values range from 96% in spring to 86% at the end of the year. The yearly average value of De_{clear} is 92%. De_{cloudy} shows a nearly constant value of about 89% throughout the year, slowly increasing to 92% at the end. The variability is high.

During nighttime the impact of the neighbor test is less than 1% for both detection efficiencies. During daytime the additional tests add about 2.7% to De_{cloudy} while decreasing De_{clear} by about 1%. The combined test has a larger impact than the neighbor test. Although 2.7% does not seem large, it indicates a 25% decrease in the amount of clouds not detected, which is significant. Furthermore, the neighbor test enables a better definition of the edge of a cloud field, which is of importance to meteorological practice.

SEA

In Figure 4.19a the diurnal variability of the detection efficiencies is presented. During daytime De_{cloudy} is about 88% and De_{clear} 94%, while during nighttime De_{cloudy} is about 80% and De_{clear} 90%. At 12 UTC the VIS-test adds 6% to De_{cloudy} and reduces De_{clear} with less than 1%. The VIS-test has more impact over SEA than over LAND, probably because the sea surface has a lower reflectivity and a smaller variability. The variability of two-weekly values as shown by the σ bars is high, which is also true for the year variability (Figure 4.19b). At 12 UTC De_{cloudy} is about 90% in winter and spring and about 10% lower during summer. De_{clear} shows the opposite signature being high (95%) in summer and relatively low (90%) in winter. Especially during summer there is a high month to month variability in De_{cloudy} . Part of this is due to the use of various sets of synoptic data and gaps in the acquisition of Meteosat and HIRLAM data.

4.3.6. Discussion and conclusions

The main difference between Metclock and other cloud detection schemes is the method with which the temperature threshold in the infrared is obtained. Most algorithms utilize frequency analysis of the spatial distribution of temperatures measured from satellite. The resulting threshold has the spatial resolution of the area analyzed to obtain it. Over sea this approach works well because the spatial variability is relatively low. Over land, however, high temperature gradients occur due to variability of surface types, vegetation, orography and others characteristics over small distances. The threshold in the IR-test from Metclock is

derived from model surface temperatures, which are available at 50km resolution. In order to account for the different purpose and nature of model and satellite temperatures a processing environment was set-up to quantify the difference between model surface temperatures and satellite temperatures for cloud free conditions. This temperature difference, which varies widely with geographical location, time of day and time of year, enables us to use only one threshold value for an area ranging from 25 degrees West to 25 degrees East and 35 to 70 degrees North for day and night, the whole year through. We find that the IR-test is very efficient in discriminating cloudy from cloud free pixels. The results show relatively little diurnal variation and the detection efficiencies are stable throughout the year. The IR-test is the basis for the Metclock algorithm.

We added a more commonly used VIS reflectivity test with conservative thresholds, such that the fraction of cloud free conditions classified cloudy was small compared to the results of the IR-test. Consequently, the additional contribution to the identification of cloudy pixels by the VIS-test is also limited to about 4%. The detection efficiency shows large variations which are probably due to the varying quality of the reflectivity map in cases where there are no cloud free situations during the two weeks of analysis. We find that there is room for improvement of the reflectivity maps especially over sea.

The two additional tests, which are based on supporting arguments, the neighbor test and the combined visible-infrared test, contribute about 2.7% percent to the detection of cloudy pixels. This seems little, but it is a reduction of the fraction of cloudy pixels not identified by about 25%, which is significant. However, the amount of pixels classified cloudy in clear sky conditions increases with 1%.

The most difficult part of the processing scheme is the handling of synoptic observations, which vary in spatial extent, location (especially over sea), spatial density, temporal frequency and quality. The synoptic observations are used for quantifying the temperature difference between model surface temperatures and satellite brightness temperatures and for validation. The method is relatively sensitive to the quality and amount of clear sky observations. In general there are about 6 times as many (nearly) overcast situations reported at 12 UTC in 1997 over the Metclock area than cloud free. If 1% of the overcast situations is reported incorrectly as cloud free this will result in an error of 1% in the detection efficiency for cloudy cases, which is not significant. But the detection efficiency for cloud free situations

will be reduced by 6%. Currently De_{clear} ranges from about 85% to 100%, so a 6% reduction is significant. From these values one may conclude that the quality of the synoptic observations is sufficiently accurate, and that our environment for identifying erroneous reports functions well. However, it is possible that the variability of De_{clear} values, especially over sea and during the night, is partly caused by the irregular occurrence of erroneous synoptic reports. In the Metclock algorithm, synoptic observations of cloud free sky are also used in quantification of T_{dif} , which makes the whole method extra sensitive to the quality of these reports.

The Metclock processing scheme depends on a stable operational atmospheric model. We use HIRLAM because it has a relatively high spatial and temporal resolution, but other models can also be used. A crucial part of the processing is the quantification of the difference between model and satellite temperature. If the temperature difference varies at time scales smaller than our two week analysis interval, the method will not be able to account for it and the quality of the cloud detection results will vary likewise.

We balanced the thresholds such that the amount of pixels labeled incorrectly cloudy is relatively small, at the expense of a lower detection efficiency for cloudy cases. For each application the thresholds can be optimized to balance the importance of identifying cloud free areas and the importance of identifying cloudy areas.

The cloud detection results generated by the Metclock detection scheme are used in the KNMI Cloud Detection System to reconstruct the 3-dimensional cloud distributions in a form to improve parameterizations of cloud ensembles in atmospheric models. The cloud detection results are also used for the initialization of a short term cloud prediction model and will be used in an operational weatherservice environment.

The characterization part of Metclock, which is used to retrieve cloud cover fraction, optical thickness, emissivity and correct cloud top temperature from the reflected sunlight as measured from the VIS channel, is in development. At this stage there are three candidate data sets on reflectivities of cloudy atmospheres considered for the interpretation of the measured reflectivity: the sets by Minnis et al. (1993a,b, 1995, 1998), Taylor and Stowe (1984) and Koелеmeijer et al. (1995). The results will be validated using the KNMI cloud detection system measurements (Feijt and Van Lammeren, 1996) and cloud characteristics as measured

during the Cloud and Radiation intensive measurement campaigns, CLARA (Van Lammeren and Feijt, 1997; Feijt et. al, 1999).

Acknowledgements

We would like to thank Rose Dlhopsky, Robert Koelemeijer and Andre van Lammeren for helpful comments on this work. The work presented was partly funded by the Netherlands Remote Sensing Board (BCRS) and the Dutch National Research Program on Global Air Pollution and Climate Change (NRP).

References

- Ackerman S.A., S. K. Cox, 1981, Comparison of satellite and all-sky camera estimates of cloud cover during GATE. *J. Appl. Met.*, **20**, 581- 587.
- Barnes J. C. and D. Chang, 1968, Accurate cloud cover determinations and its effect on albedo computations . Final report, Contract No. NA55-10478, Aracon Inc., Concord, Mass., 82 pp.
- Barrett E. C. and C. K. Grant, 1979, Relations between frequency distribution of cloud over the UK based on conventional observations and imagery from Landsat 2, *Weather*, **34**, 416-424.
- Bishop J.K.B., W.B. Rossow and E.G. Dutton, 1997: Surface solar irradiance from the International Satellite Cloud Climatology Project 1983-1991. *J. Geophys. Res.*, **102** (D2), 6883-6910.
- Coakley J.A. and F.P. Bretherton, 1982: Cloud cover from high-resolution scanner data: Detecting and allowing for partially filled fields of view. *J. Geophys. Res.*, **87**, 4917-4932.
- Derrien, M., Farki B., Harang L., LeGleau H., Noyalet A., Pochic D. and Sairouni A.; 1993, Automatic cloud detection applied to NOAA-11/AVHRR imagery. *Rem. Sens. Environ.*, **46**, 246-267.
- Desbois M, G. Seze and G. Szejwach, 1982: Automatic classification of clouds on METEOSAT imagery: Application to high-level clouds. *J. Appl. Meteor.*, **21**, 401-412.

- Desormeaux, Y., W. Rossow, C. Brest and G. Campbell, 1993: Normalization and calibration of geostationary satellite radiances for the International Satellite Cloud Climatology Project. *J. Atmos. and Ocean. Techn.*, 10, 304-325.
- Diekmann F.J. and J de Waard; 1992, New concepts of Meteosat image data resampling. *Proc. of the EUMETSAT Meteorological Satellite Data Users' Conference*, Locarno, Eumetsat, 401-407.
- EUMETSAT; 1997, MSG ground segment: Meteorological products extraction facility algorithm specification document. Eumetsat Doc. No. EUM/MSG/SPE/022., EUMETSAT, Darmstadt.
- Feijt A. and P. de Valk, 2000: The use of NWP data in cloud detection from Meteosat imagery. *Int. J. Rem. Sens.* (accepted).
- Feijt A., H. ten Brink, S. Jongen, A. van Lammeren and H. Russchenberg, 1999: Validation of cloud parameter retrieval methods with objective ground based measurements. *Phys. Chem. Earth*, **24**, 173-176.
- Feijt A. and P. de Valk, 1998: Quantifying the difference between NWP surface temperatures And cloud free satellite apparent brightness temperatures. *Contrib. Atmos. Phys.*, 71, 455-460.
- Feijt A. and A. van Lammeren, 1996: Ground-based and satellite observations of cloud fields in the Netherlands. *Monthly Weather Review*, **124**, 1914-1923.
- Gustafsson N., 1993: HIRLAM 2 Final Report. SMHI Technical Report 9., 129pp.
- Gtopo30, 1998: Gtopo30: Description of world topography data set. On Internet:
- Henderson-Sellers A. and K. McGuffey, 1991: An investigation of the burger distribution to characterize cloudiness. *J. of Clim.*, **4**, 1181-1209.
- <http://edcwww.cr.usgs.gov/landdaac/gtopo30/gtopo30.html>, EROS data center, Sioux Falls, SD
- Karlsson, K-G.; 1996: Cloud classification with the SCANDIA model. SMHI report RMK 67., SMHI, Norrkoping.
- Jonas P., 1991: Cloud cover distributions and correlations. *J. Appl. Met.*, **31**, 732-741.
- Karlsson K-G., 1993: Comparison of operational AVHRR-based cloud analysis with surface observations. *Proc. 6th AVHRR data users'meeting*, EUMETSAT, Darmstadt, 223-229.
- Koelemeijer R. B. A., P. Stammes and A. Feijt, 1995: Cloud optical thickness retrieval from AVHRR-data. *Proc. Symposium on Atmospheric Sensing and Modelling II*, SPIE vol. **2582**, 284-293.

- Koepke, P., 1982: Vicarious calibration of the Meteosat visible channel. *Appl. Opt.*, 21(15), 2845-2854.
- Koepke P. and K.T. Kriebel, 1978: Influence of measured reflection properties of vegetated surfaces on atmospheric radiance and its polarization. *Appl. Optics*, 2, 260-264.
- Kriebel, K.T. and V. Amann, 1993: Vicarious calibration of the Meteosat visible channel. *J. Atmos. and Ocean. Techn.*, 10(2), 225-232.
- Kriebel K.T., 1978: Measured spectral bidirectional reflection properties of four vegetated surfaces. *Appl. Optics*, 2, 253-259.
- Labeled J. and M.P. Stoll, 1991: Spatial variability of land surface emissivity in the thermal Infrared band: spectral signature and effective surface temperature. *Rem. Sens. Environ.*, 38, 1-17.
- Lammeren A. van, A. Feijt, J. Konings and E. van Meijgaard, 1999: Combination of ground Based and satellite cloud observations on a routine basis. *Contr. Atmos. Phys.* (in press).
- Lammeren, A. van and A. Feijt, 1997: Cloud research in the Netherlands: CLARA. *Change*, 34, NRP, Bilthoven, 10-13.
- Meijgaard E. van, J. Konings, A. Feijt and A. van Lammeren, 1999: Comparison of model predicted cloud cover profiles with observations from ground and satellite. *Contr. Atmos. Phys.* (in press).
- Minnis P., D.P. Garber, D.F. Young, R.F. Arduini, Y. Takano, 1998: Parametrizations of reflectance and effective emittance for satellite remote sensing of cloud properties. *J. Atmos. Sci.*, 55, 3313-3339.
- Minnis P., W.L. Smith Jr., D. P. Garber, J.K. Ayers and D.R. Doelling, 1995: Cloud properties derived from GOES-7 for the spring 1994 ARM intensive observing period using version 1.0.0 of the ARM satellite data analysis program. *NASA Rep.* 1366, 59pp.
- Minnis P., K-N Liou and Y Takano, 1993a: Inference of cirrus cloud properties using satellite-observed visible and infrared radiances. Part I: Parametrization of radiance fields, *J. Atmos. Sci.*, 50, 1279-1304.
- Minnis P., P.W. Heck and D.F. Young, 1993b: Inference of cirrus cloud properties using satellite-observed visible and infrared radiances. Part II: Verification of theoretical cirrus radiative properties, *J. Atmos. Sci.*, 50, 1305-1322.

- Minnis P. and E.F. Harrison, 1984a: Diurnal variability of regional cloud and clear sky radiative parameters derived from GOES data. Part I: Analysis method, *J. Climate Appl. Meteor.*, **23**, 993-1011.
- Minnis P. and E.F. Harrison, 1984b: Diurnal variability of regional cloud and clear sky radiative parameters derived from GOES data. Part II: November 1978 cloud distributions, *J. Climate Appl. Meteor.*, **23**, 1012-1031.
- Minnis P. and E.F. Harrison, 1984c: Diurnal variability of regional cloud and clear sky radiative parameters derived from GOES data. Part III: November 1978 radiative parameters. *J. Climate Appl. Meteor.*, **23**, 1032-1051.
- Moulin, C., C.E. Lambert, J. Poitou and F. Dulac, 1996: Long term (1983-1994) calibration of the Meteosat solar (VIS) channel using desert and ocean targets. *Int. J. Rem. Sens.*, **17**, 6, 1183-1200.
- Moene A., 1998: Personal communication.
- Rossow W.B. and L.C. Garder, 1993a: Cloud detection using satellite measurements of infrared and visible radiances for ISCCP, *J. Climate*, **6**, 2341-2369.
- Rossow W.B. and L.C. Garder, 1993b: Validation of ISCCP cloud detection, *J. Climate*, **6**, 2370-2393.
- Rossow W.B., A.W. Walker and L.C. Garder, 1993c: Comparison of ISCCP and other cloud amounts, *J. Climate*, **6**, 2394-2418.
- Rossow W.B. and R.A. Schiffer, 1991: ISCCP cloud data products. *B.A.M.S.*, **72**, 2-20.
- Rossow W.B., F. Moshier, E. Kinsella, A. Arking, M. Desbois, E. Harrison, P. Minnis, E. Ruprecht, G. Seze, C. Simmer and E. Smith, 1985: The ISCCP cloud algorithm intercomparison, *J. Climate Appl. Meteor.*, **24**, 877-903.
- Salisbury J.W. and D.M. D'Aria, 1992: Emissivity of terrestrial materials in the 8-14 μ m atmospheric window. *Rem. Sens. Environ.*, **42**, 83-106.
- Saunders, R.W. and K.T. Kriebel, 1988, An improved method for detecting clear sky and cloudy radiances from AVHRR data. *Int. J. Rem. Sens.*, **9**, 123-150.
- Schmetz, J., P. Menzel, C. Velden, X. Wu, L. van de Berg, S. Nieman, C. Hayden, K. Holmlund, 1995: Monthly mean large-scale analyses of upper-tropospheric humidity and wind field divergence derived from three geostationary satellites. *Bull. Amer. Meteor. Soc.*, **76**(9), 1578-1584.
- Schmetz J. and L. van de Berg, 1994: Upper tropospheric humidity observations from Meteosat compared with short-term forecast fields. *Geophys. Res. Letters*, **21**, 573-576.

- Schreiner A.J., D.A. Unger, W.P. Menzel, G. P. Ellrod, K.I. Strabala and J.L. Pellet, 1993, comparison of ground and satellite observations of cloud cover. *B.A.M.S.*, **74**, 1851-1861.
- Seze G. and W.B. Rossow, 1991a: Time-cumulated visible and infrared histograms used as description of surface and cloud variations, *Int. J. Remote Sensing*, **12**, 877-920.
- Seze G. and W.B. Rossow, 1991b: Effects of satellite data resolution on measuring the space/time variations of surfaces and clouds, *Int. J. Remote Sensing*, **12**, 921-952.
- Simmer C., E. Raschke and E. Ruprecht, 1982: A method for determination of cloud properties from two-dimensional histograms. *Ann. Meteor.*, **18**, 130-132.
- Singh S.M., A.P. Cracknell and A. F. G. Fiuza, 1985: The estimation of atmospheric corrections to one-channel (11 μ m) data from the AVHRR; simulation using AVHRR/2. *Int. J. Rem. Sens.*, **6**, 927-945.
- Taylor V. and L. L. Stowe, 1984: Atlas of reflectance patterns for uniform earth and cloud Surfaces (NIMBUS-7 61 days). NOAA Tech. Rep. NESDIS 10, 66 pp.
- Valk de P, Feijt A. and Roozkrans H.; 1997, The application of NWP data and Meteosat imagery in the retrieval of cloud parameters. Proc. of the EUMETSAT Meteorological Satellite Data Users' Conference, Brussels, Eumetsat, 139-146.
- Veen S. van der, and A. Feijt: Liquid water initialization in a cloud prediction model using Meteosat imagery. Proc. of the 1996 EUMETSAT Meteorological Satellite Data Users'Conference, EUMETSAT, Darmstadt, 257-264.
- World Climate Program, 1988: International Satellite Cloud Climatology Project (ISCCP) documentation of cloud data. WMO/TD-No. 266, 76 pp.
- Wielicki B.A. and L. Parker, 1992: On the determination of cloud cover from satellite sensors: The effect of sensor spatial resolution, *J. Geophys. Res.*, **97**, D12, 12799-12823. WMO; 1996, Guide to meteorological instruments and methods of observations, WMO 8, WMO, Geneva.
- WMO, 1996: Guide to meteorological instruments and methods of observations. WMO 8, WMO Geneva.
- WMO, 1989: Guide on the global observing system. WMO 488, WMO, Geneva.
- Woick H., J. Schmets and S. Tjemkes: An introduction to Meteosat Second Generation imagery and products. Proc. of the 1997 EUMETSAT Meteorological Satellite Data Users'Conference, Brussels, EUMETSAT, Darmstadt, 395-400.

5. Case studies of ground based and satellite observations of cloud fields

Case studies of cloud observations are valuable to understand measurement techniques and cloud processes. In this chapter, a number of cloud fields are studied in detail. Cloud field characteristics are measured both from ground and space. In order to relate the two types of measurements, the atmospheric conditions and cloud processes involved have to be understood. *The physical phenomena involved are identified from the measurements: the atmospheric conditions, the related cloud processes, the cloud-radiation interactions, and the sensor response.* Each bit of information contributes to the analysis and allows for a better understanding. This enables a comparison of the measurements with the conceptual model that is the basis to the retrieval algorithms.

The information on cloud properties is of a statistical nature, because clouds are highly variable in time and space. It is not possible to exactly calculate the evolution of a volume of cloudy air in time. The evolution of an individual cloud cannot be predicted in detail. A comparison of ground based and satellite based measurements is difficult, because the statistical cloud field parameters have to be mapped from time to space.

Section 5.1 describes measurements from ground based lidar and infrared radiometer and satellite based Meteosat and AVHRR. The atmospheric conditions studied are a frontal zone and a field of fair weather cumuli in June and August 1993. The study is mainly phenomenological, because *the satellite analysis environments that were described in chapter 3 and 4, were not yet available at that time.* Measurements from the CLARA intensive measurement campaigns are studied in section 5.2. The studies include evaluation of the AVHRR retrieval methods for water clouds and ice clouds.

5.1 Ground-Based and Satellite Observations of Cloud Fields in the Netherlands*

Abstract

A study is performed on the combination of ground-based and satellite observations for the derivation of cloud properties. Ground-based measurements from a lidar ceilometer and an infrared radiometer were combined with measurements of the NOAA Advanced Very High Resolution Radiometer and Meteosat satellite instruments. Two case studies are presented: a case with streets of fair weather cumuli and a case with a weak cold front involving cumulus, stratus, and cirrus clouds. From the combination of ground-based and satellite observations, a much better description of the cloud field geometry, cloud base, and cloud top can be obtained than with satellite or ground-based observations alone. The combination of satellite retrievals and lidar-ceilometer measurements is promising. This concept is widely applicable because lidar ceilometers are available on airports all over the world and the used infrared sensors are relatively cheap and can easily be installed. This opens the way for a much improved automatic detection of clouds and their properties.

*) This section was published in this form.

Feijt A. and A. van Lammeren, 1996: Ground-based and satellite observations of cloud fields in the Netherlands. *Monthly Weather Review*, 124, 1914-1923.

1. Introduction

Clouds play an important role in our climate. They produce precipitation, which is an essential ingredient of the hydrological cycle, and they modify the earth's radiation budget. Thin cirrus clouds have a warming effect, while low clouds have a distinct cooling effect (Ramanathan et al. 1989). Clouds dominate the vertical transport of energy, momentum, and trace gases in the free troposphere. Despite their importance, clouds are represented only rudimentary in climate as well as weather forecast models. The representation of clouds in climate models has a major impact on model predictions for climate change. Cess et al. (1989) showed that cloud feedback is a major source of uncertainty in model responses to climate forcing. There are two main reasons why the uncertainties with respect to clouds are so large. The first reason is that cloud processes are extremely complicated. A proper representation of clouds requires parameterization of sub-grid processes both on macro-scale (centimeters to kilometers) and on micro-scale (much smaller than centimeters). The second reason is the lack of accurate quantitative observations of cloud characteristics (cloud cover, cloud structure, optical thickness, droplet size spectra). This lack of accurate data hampers the development and validation of models. Satellites have proven to provide useful data on global cloud statistics and corresponding radiation budgets. Projects like the International Satellite Cloud Climatology Project (ISCCP) (Schiffer and Rossow, 1983) and the Earth Radiation Budget Experiment (ERBE) (Barkstrom and Smith 1986) have contributed greatly to the understanding of cloud processes and cloud-radiation interaction. These datasets are used by climate modelers. Evaluation of the ERBE results is still ongoing (Cheruy and Kandel, 1991; Feijt, 1992). Rossow and Garder (1993a,b) and Rossow et al. (1993) recently published a validation study of the ISCCP algorithm and its results for cloud cover. The derived mean annual global cloud fraction was 63%, which is at the very high end of frequently used estimates. The estimate of cloud fraction depends on the remote sensing instrument and the applied retrieval technique (Wielicki and Parker, 1992). This makes it virtually impossible to measure a change in cloud climatology using ISCCP data (Klein and Hartmann, 1993). New attempts to measure cloud climatology are made using better remote sensing instruments and more refined algorithms (Kastner et al., 1993). The problem of interpretation of satellite data is in essence caused by the concept of remote sensing itself (Rossow, 1989). The radiance received by the detector contains contributions from various sources: surface, atmosphere, and clouds. The radiative properties of these sources vary with location, time, and wavelength. Within one field of view (FOV) the surface may have a distribution of radiative

properties depending on soil type, vegetation, humidity, and viewing and solar geometry. Our object of study, clouds, are highly variable in time and space. The description of the variability of cloud fields is a field of study in itself (Lovejoy and Schertzer, 1990; Cahalan and Snider, 1989). However ingenious cloud detection and characterization algorithms may be, there is always a lack of information to separate all contributions to the detector signal. In general, one can state that the more information there is available the better the cloud detection algorithm will work. This basic thought has led to the concept of cloud field analysis using a combination of ground-based and satellite observations. The aim of the present paper is to assess the strength of this concept. A study was performed to obtain a configuration of instruments suitable to measure geometrical cloud properties accurately over a small area for validation of cloud parameterizations in models. In section 2 of this paper a description of the experimental setup is given. In section 3 two cases are analyzed. The results are discussed in section 4.

2. Experimental setup

Ground station

Measurements are performed at the meteorological tower at Cabauw in the Netherlands at 52°N, 5°E. The area is characterized by a moderate marine climate with a prevailing westerly circulation. In the tower the mean vertical profiles of temperature, humidity, visibility, and wind speed and direction are measured up to 200 m. On the ground, the following instruments are installed:

- lidar ceilometer (910 nm),
- narrowband IR radiometer (9.6- 11.5 μm),
- pyranometer (0.3-3 μm),
- precipitation detector, and
- rain gauge.

Also a video camera (color S-VHS system) is installed, which takes an image of the sky each 3.2s. The recordings are a valuable aid in interpreting the other measurements. For interpretation of the measurements data on the actual atmospheric conditions and radiative transfer models are available. The High-Resolution Limited Area Model (HIRLAM), which is

an operational weather forecast model at KNMI, provides information on temperature and humidity profiles, and wind speed and direction on a 50-km grid (Gustafsson, 1993). The 6-h radiosonde data from De Bilt are available. Radiative transfer calculations are performed using LOWTRAN-7 (Kneizys et al., 1988) for longwave and the KNMI doubling-adding model (DAK) for shortwave radiation (Stammes, 1992). DAK calculates the multiple scattering by atmosphere, ground and plane-parallel cloud as a whole. In DAK the user may define a cloud by its droplet size distribution, optical thickness, and height.

b. Satellites

In the experiment both NOAA Advanced Very High Resolution Radiometer (AVHRR) and Meteosat images are analyzed. The polar satellites, NOAA-10 and NOAA-11, pass the measurement site twice per day (spatial resolution 1 km x 1 km sub-satellite). Meteosat data is available every half hour with a spatial resolution of 5 km x 9 km. The AVHRR processing scheme over clouds, land, and ocean (APOLLO) (Saunders 1986; Saunders and Kriebel 1988; Gesell et al. 1993) is used for detection of cloud contaminated and fully cloudy pixels from AVHRR measurements. Local implementations of the APOLLO retrieval methods of cloud properties are used for validation and development purposes. A bi-spectral cloud detection algorithm, inspired by the ISCCP cloud detection scheme (WCP, 1988), has been developed to analyze the Meteosat measurements. A basic assumption in the ISCCP algorithm is that the radiative properties of clouds have a higher temporal variability than the underlying surface (Seze and Rossow, 1991a,b). The KNMI bi-spectral cloud detection algorithm uses information on the actual atmospheric conditions from weather forecast model analysis to calculate dynamic-detection thresholds. In our analysis, Meteosat data is mainly used to monitor the temporal variability of cloud fields.

3. Combining ground and satellite observations

a. Case study: 20 June 1993

On 20 June 1993, it was a nice summer day in the Netherlands. The meteorological conditions were dominated by a high pressure area over the British Isles, causing a west-northwesterly wind over the Netherlands. Subsidence transported air downward and dried it out. The boundary layer was lightly unstable, causing water vapor to condense right below the inversion. Fair weather cumuli were formed. The clouds persisted through the day from 7:00 until 17:00 UTC (7:20 until 17:20 LST), when insolation had decreased too much.

1) ANALYSIS OF SATELLITE OBSERVATIONS

Figure 5.1 shows the Netherlands as observed from NOAA-11 by AVHRR channel 1 ($0.63\ \mu\text{m}$) at 15:27 UTC. The cumuli are organized in cloud streets that are parallel to the wind. Figure 5.2 shows the Meteosat vis image of 15:30 UTC. It shows a speckle pattern indicating cumulus clouds.



Figure 5.1.: AVHRR channel 1 image of 1527 UTC 20 June 1993. Arbitrary scale.

The spatial structure of the cloud fields can hardly be recognized. The contrast between clouds and surface is much lower than in the AVHRR image due to the lower spatial resolution and the larger band width of the vis channel. The AVHRR cloud mask is obtained from the APOLLO scheme. According to Saunders and Kriebel (1988), fully cloudy pixels

must be selected to obtain cloud properties. However, the cumulus clouds are so small that there are no fully cloudy pixels detected in the fair weather cumulus field. Further analysis of the cloud field is not possible without extra information. The Meteosat cloud mask is obtained from the KNMI bi-spectral method. The spatial resolution of the Meteosat image is much lower than that of the AVHRR image, so no further information on cloud properties can be derived.

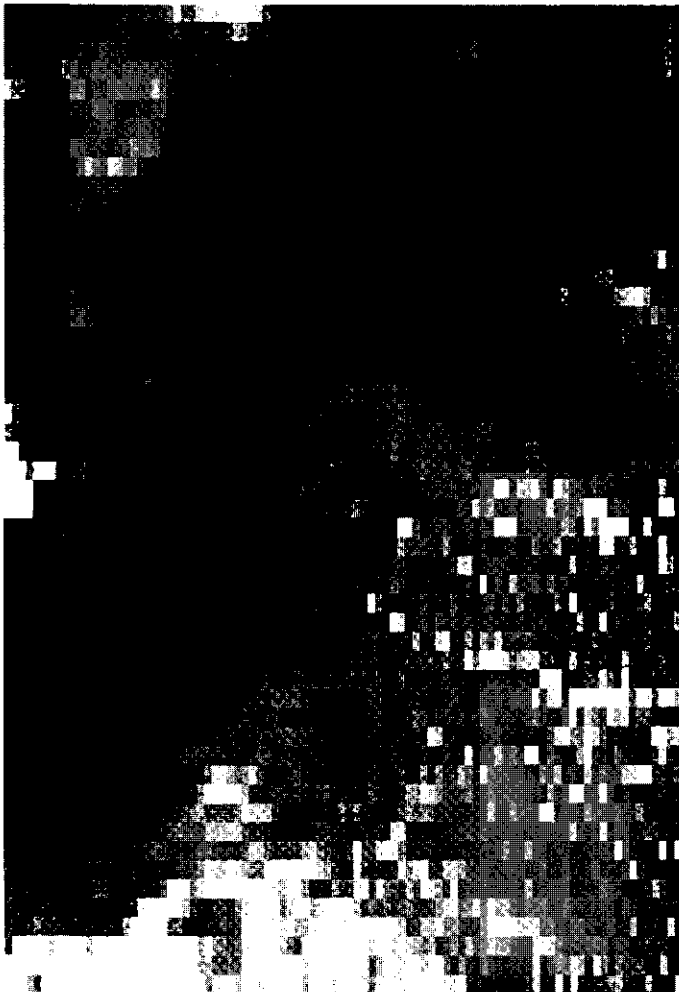


Figure 5.2: Meteosat visible image of 15:30 UTC 20 June 1993. Arbitrary scale.

2) ANALYSES OF GROUND-BASED OBSERVATIONS

According to lidar measurements the typical cloud-base height at Cabauw at noon is 1100m. The infrared radiometer measured the maximum sky temperature to be 9°C. The sky temperature is highest when an opaque cloud fills the FOV of the radiometer. In order to convert the measured equivalent black body temperature to cloud-base temperature, the signal must be corrected for radiation absorbed and emitted by the atmosphere between the radiometer and the cloud. Radiosonde temperature and humidity profiles and the cloud-base altitude derived from lidar measurements are input to

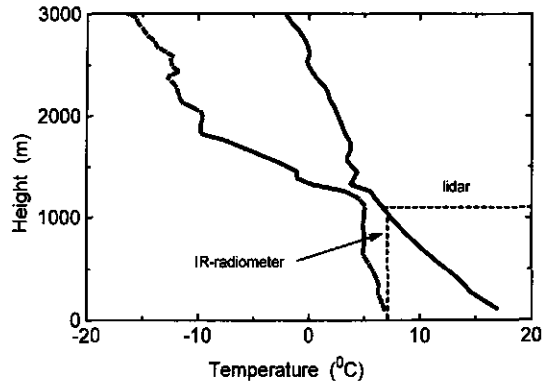


Figure 5.3: The radiosonde air (solid) and dewpoint (dashed) temperature profiles from 12:00 UTC 20 June 1993 at De Bilt.

LOWTRAN-7 for calculation of the atmospheric correction in the band of the infrared radiometer. The correction

in this case was -2°C, so the cloud-base temperature is 7°C. We are now able to plot the measured cloud-base height and cloud-base temperature in the radiosonde temperature profile of 1200 UTC at De Bilt (Figure 5.3). The cloud temperature and height measurements coincide well with the temperature and humidity profile. The lines of dew-point and air temperature meet at the measured cloud-base height. Lidar measurements are further used to obtain the horizontal cloud size distribution. If two successive measurements of cloud-base height do not differ more than a specified threshold, they are assumed to originate from the same cloud. The product of the time that the cloud is detected and the wind speed at the cloud-base yields the cloud size. A correction is applied because clouds in general pass the lidar off center (Van Lammeren and Feijt, 1994). The distribution is shown in Figure 5.4. According to this distribution, most clouds are smaller than 450 m. A small number of clouds is larger than 1500 m. The average AVHRR pixel area over the Netherlands for this case was 1 km x 1.7 km². So, there could be clouds, which completely fill an AVHRR pixel. However, generally a cloud of the same size as the pixel area will be spread out over four neighboring pixels.

3) COMBINING GROUND AND SATELLITE OBSERVATIONS

From the ground-based measurements we have information on a scale smaller than the FOV of the satellite instruments, which can be used to interpret the satellite images. In one FOV there are contributions from the ground and from clouds. The cloud fraction can be derived from the measured radiance if surface and cloud temperature are known (Saunders and Kriebel, 1988). The ground temperature can be derived from pixels that are not cloud contaminated, provided the derived surface temperature are representative for the area of interest. The surface temperature does not vary much over the Netherlands due to both the limited extent of the area and the little orographic diversity¹. However, the surface temperature is not

representative for pixels that are part of small water bodies like lakes and rivers. The cloud-top temperature is derived from ground-based IR-radiometer measurements of the cloud-base temperature. We introduce a bias here because the cloud top is colder than the cloud base. However, as the clouds considered are small the bias is expected to be accordingly small. When deriving the cloud cover fraction from the surface and cloud temperature, the emissivity and transmissivity of the atmosphere between source (surface or cloud) and satellite instrument has to be taken into account. Figure 5.5a shows the cloud fraction per pixel derived from the Meteosat infrared image at 15:30 UTC. In the south there is a large overcast area. This is caused by a thin layer of cirrus, which is not clearly visible in the shortwave but which alters the infrared radiances considerably. The results are compared with the AVHRR cloud mask of 15:27 UTC, which shows the cloud field in greater detail (Figure 5.5b). The AVHRR cloud mask is obtained from the APOLLO scheme. The cloud fraction is derived as described above for Meteosat. Analysis of synoptic observations acknowledges the presence of cirrus in the South. On the other hand, low-level cumulus clouds were reported in the "cloud-free" area near the coast. Further analysis showed that near the coast cloud-base height is about 600 m, which is considerably lower than measured at Cabauw.

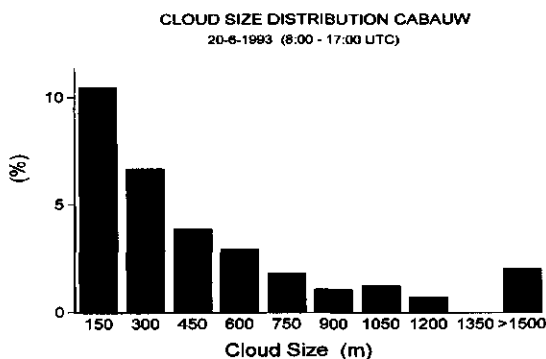


Figure 5.4: The measured cloud size distribution in Cabauw for 06:00 – 15:00 UTC 20 June 1993.



Fig 5.5: Cloud fraction derived from Meteosat image of 15:30 UTC 20 June 1993; b) Cloud fraction derived from AVHRR of 15:27 UTC; c) Cloud fraction derived from AVHRR of 15:27 UTC mapped to the Meteosat grid.

Apparently, these low-level clouds cause too little contrast with the surface to be detected by either Meteosat or AVHRR algorithms. Figure 5.5c shows the AVHRR-derived cloud fractions mapped on the Meteosat pixels. We are now able to compare the Meteosat-derived (Figure 5.5a) and AVHRR-derived (Figure 5.5c) cloud amounts quantitatively. The Meteosat cloud detection algorithm is capable of detecting the broader cloud streets. However, smaller phenomena are not present in the cloud mask. The cloud fraction as derived from Meteosat data does hardly show pixels with less than 30% cloud cover. Obviously, for lower cloud fractions the contrast between cloud free pixels and cloudy pixels is too low to exceed the cloud detection threshold. The cloud fraction derived from Meteosat data is in general higher than the AVHRR-derived values.

According to synoptic observations, the cloud-base height varied between 600m near the coast to 1500m near the German border. At Cabauw the cloud-base height was about 1100m. From the radiosonde profile we estimate the cloud-top temperature to be about 3°C higher near the coast than at Cabauw. As a result the cloud-cover fraction as derived from combined groundbased and satellite observations is about 20% too low near the coast. The cloud-cover fraction is about 20% to high near the German border. Synoptic observations of cloud-cover fraction confirm that the cloud-cover fraction was underestimated near the coast and overestimated near the German border. This case study shows that a coherent picture of a cloud field of fair weather cumuli can be obtained from a combination of ground-based and satellite measurements. The measurements are complementary in the sense that ground-based observations yield detailed information of cloud properties on a specific location continuous in time: cloud-base temperature and height and the cloud size distribution. Satellite images yield the spatial distribution of cloud properties. The cloud streets are visible from the AVHRR only. The cumulus clouds in this study are too small to be detected individually using the AVHRR instrument. As a result there are no fully cloudy pixels in the AVHRR image. Still cloud-cover fraction could be derived using ground-based measurements. From the Meteosat only the broader cloud streets could be detected.

b. Case study: 4 August 1993

On 4 August 1993 there was a high pressure system over eastern Europe and a low pressure system over Norway. There was a weak cold front over the Netherlands. The front moved slowly to the west. Surface pressure during the passage of the front was relatively high at 1020hPa.

1) ANALYSIS OF SATELLITE OBSERVATIONS

The AVHRR channel 4 image of 7:20 UTC shows the frontal cloud band (Figure 5.6). When running the APOLLO scheme, the scheme labels nearly all pixels as cloud contaminated. Natural and anthropogenic cirrus clouds are observed in single and mixed layers. Streaky patterns are identified as contrails. The contrails are generated by airplanes that visit Amsterdam airport. The frontal cloud band is labeled fully cloudy. In our analysis of the frontal cloud layer, the AVHRR channel 4 radiances are corrected for atmospheric absorption and emission using LOWTRAN-7 and the radiosonde profile of 6:00 UTC at De Bilt. The

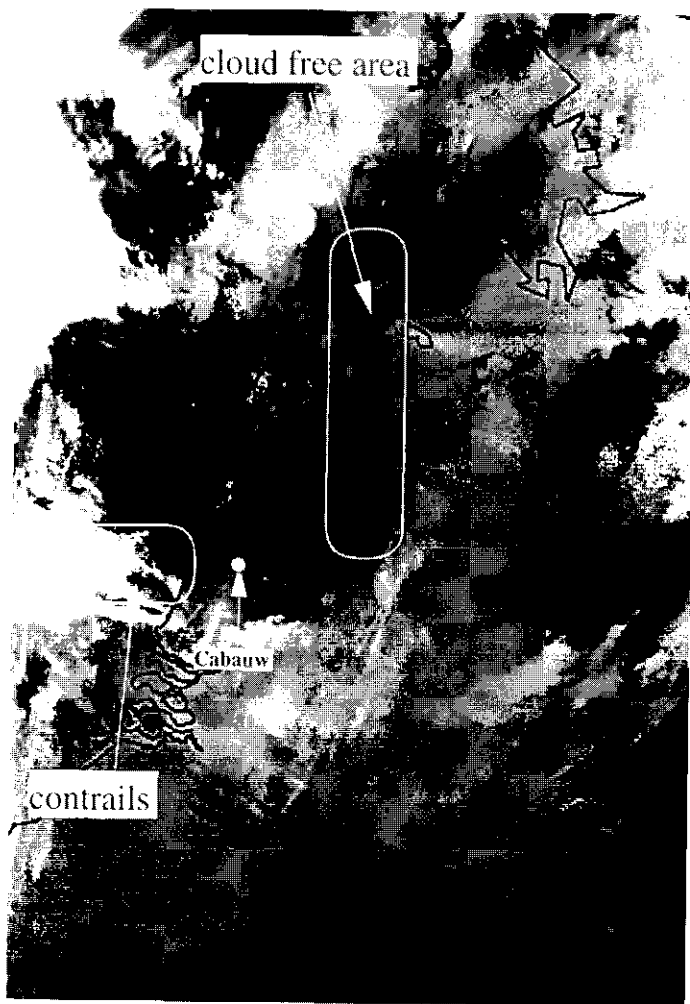


Figure 5.6: AVHRR channel 4 image of 7:20 UTC 4 August 1993.
Scaling: black, $T > +15^{\circ}\text{C}$, white $T < -15^{\circ}\text{C}$.

cloud-top temperatures ranges from 0° to 5°C . Reflectivity of the whole system of atmosphere, cloud layer, and surface as derived from AVHRR channel 1 measurements, according to preflight calibration and assuming isotropic reflection, varies between 40% and 80%. The solar zenith angle is 60° and the mean viewing zenith angle is 30° . The mean relative azimuth between sun and satellite is about 15° , so the single-scattering angle is 150° . According to Taylor and Stowe (1984) and DAK, the anisotropy factor is close to unity for this viewing geometry. Although this result was derived from much coarser data, this indicates that we are not in a problem area. There is a cloud-free band that runs from north to south near the Dutch-German border. From this band we derive the reflectivity of the atmosphere-ground system to be about 8%.

2) ANALYSIS OF GROUND BASED OBSERVATIONS

From the lidar measurements we conclude that between 6:00 and 12:00 UTC there are at least two cloud layers (Figure 5.7). The lower layer is at 0.5km at 9:00 UTC. The height increases during the day to 1.2km at 1500 UTC. The upper layer is at 2.7km. The lower layer could not be identified from satellite measurements. The cloud-cover fraction is estimated from time series of lidar measurements. The time fraction that a cloud in the height range of the cloud layer is detected is equal to the cloud-cover fraction. Isotropic spatial distribution of clouds (no cloud bands) is assumed. The mean cloud fraction of the lowest cloud layer at Cabauw was 35% for the time

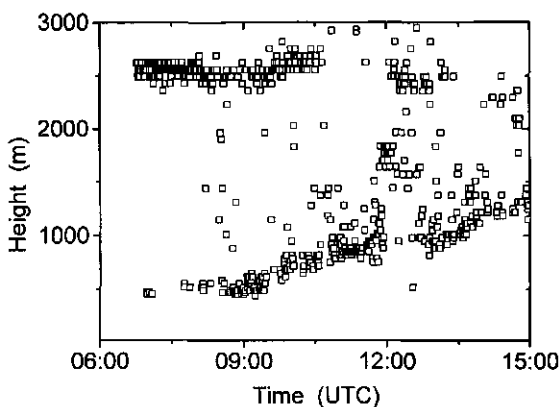


Figure 5.7: The measured cloud base height in Cabauw for 6:00 – 15:00 UTC 4 August 1993.

period from 6:00 to 15:00 UTC. Since the second cloud layer is masked by the lowest layer, the

cloud-cover fraction of the second layer cannot be measured from the ground. Figure 5.8 shows the cloud size distribution at Cabauw for the lower cloud layer from 6:00 to 15:00 UTC. The distribution is dominated by small (<150 m) clouds. Between 150 m and 1 km, the frequency of occurrence decreases. For larger clouds the distribution is random due to the small frequency of occurrence.

From the infrared radiometer data (not shown) both cloud layers can be identified. The lower layer has a cloud-base temperature of about 10°C, while the higher layer has a base temperature of about 0°C. These temperatures are corrected for the atmosphere using LOWTRAN-7 and radiosonde data. Comparison of the lidar cloud-base height and radiometer cloud-base temperature with the radiosonde air temperature and dewpoint profiles show good agreement (Figure 5.9). The reflectivity of the cloud field south-southwest of Cabauw as derived from AVHRR channel 1 measurements ranges from 40% to 50%. Radiative transfer calculations using the DAK model indicate that 40% reflectivity in this viewing geometry corresponds to a cloud optical thickness on the order of 8. The methods developed by Stephens (1978) and Rossow et al. (WCP, 1988) yield comparable results.

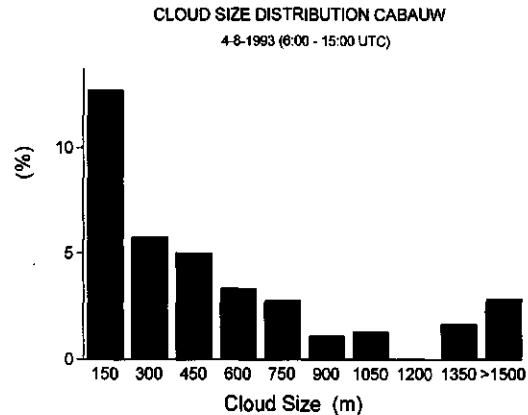


Figure 5.8: The measured cloud size distribution for the lower cloud layer in Cabauw for 6:00 – 15:00 UTC 4 August 1993. Total cloud cover fraction is 37%.

3) COMBINING GROUND AND SATELLITE OBSERVATIONS

The infrared radiometer measurements from the ground are consistent with the AVHRR and Meteosat measurements, characterizing a relatively uniform cloud layer at 2.7km. Ground-based lidar measurements reveal a lower cloud layer, which is invisible from the satellite. A cloud size distribution is derived for this cloud field. The average cloud cover fraction for the lower layer can be derived from ground-based measurements. The second layer, however, is masked from the ground instruments by the lower layer. Analysis of the AVHRR images shows

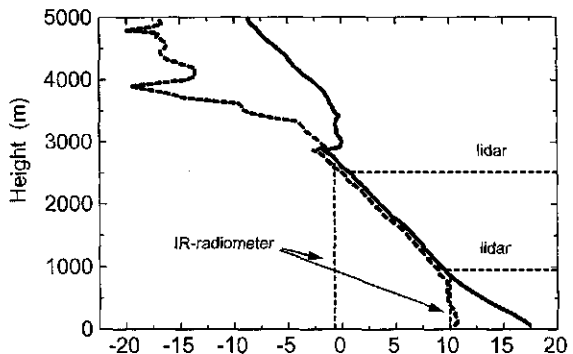


Figure 5.9: The radiosonde air (solid) and dewpoint temperature (dashed) from 6:00 UTC 4 August 1993 at De Bilt.

that all pixels of the second layer are fully cloudy. This is in agreement with synoptic observations. Meteorological reports of two synoptical stations near Cabauw, namely, Rotterdam and De Bilt, show 7/8-8/8 cloud-cover fraction for the midlevel cloud layer. The AVHRR channel 1 image (Figure 5.6) shows a large variation in cloud properties over the Netherlands. Analysis of the sequence of half-hourly Meteosat images reveals large variation of cloud properties with time. This implies that the values as derived from ground-based instruments can only be combined with satellite images that are nearby in both location and time. One single ground station is not enough to characterize cloud properties accurately over the Netherlands.

4. Discussion

A study was performed to assess the merits of the concept of combining ground-based and satellite observations to analyze cloud fields. Two cases were presented. Characterization from only ground-based or satellite measurements yields ambiguous results. We find that from the combination of lidar ceilometer, infrared radiometer, and NOAA AVHRR, or Meteosat measurements, it is possible to find a more unique characterization of the cloud field geometry. Using AVHRR data increases the accuracy of the results significantly in comparison to using Meteosat data. Also the AVHRR is capable of detecting features of a smaller scale. Comparison with synoptic observations revealed that variability of cloud height within a 150km area caused errors in derived cloud cover fraction of 20%. In future research we will use a network of ground stations for cloud characterization to quantify this variability better. A large number of airports all over the world operate ceilometers day and night. It would be very advantageous to use this data for meteorological applications. The combination of lidar ceilometer and satellite measurements has a large potential.

5.2 Validation of Cloud parameter retrieval methods with objective ground based measurements

Abstract

To understand and model the radiative transport in a cloudy atmosphere information on the cloud height and optical thickness is indispensable. Therefore retrieval techniques for cloud parameters are developed for the AVHRR, ATSR and the future MSG. Mainly synoptic observations are used for validation despite their subjective nature and varying quality. To validate advanced cloud parameter retrieval methods objective physical measurements are necessary.

At KNMI retrieval methods of cloud fraction, cloud top temperature, optical thickness and LWP from AVHRR observations are developed. Much effort is put in building an infrastructure for validation. The retrieval methods are validated with a two-year data set from the KNMI Cloud Detection System (CDS). Detailed analysis is done with observations from the Clouds and Radiation measurement campaigns (CLARA), when a number of advanced remote sensing and in-situ instruments were added to the CDS. The collocated lidar, radar, microwave radiometer and aircraft measurements from the CLARA data set allow for the evaluation of the assumptions in cloud parameter retrieval methods. Furthermore, the study presented here shows that combining measurements from lidar, radar and AVHRR provide information on cloud properties that cannot be retrieved from any of these instruments alone.

*) This section is adapted from a journal paper:

Feijt, A., H. ten Brink, S. Jongen, and A. van Lammeren, 1999: Validation of satellite cloud parameter retrieval methods with objective ground based measurements, *Phys. and Chem. of the Earth*, 24, 173-176.

5.2.1 Objective ground based measurements

5.2.1.1 The KNMI Cloud Detection System

The CDS consists of a network of 10 ground stations for remote sensing, which are distributed over an area of about 120x120 km² (Figure 5.10) and a processing environment for AVHRR and Meteosat measurements. The complete CDS was operational from October 1994 until December 1996 (Stammes et al.,1994). The instruments at each ground station are listed in Table 5.1.

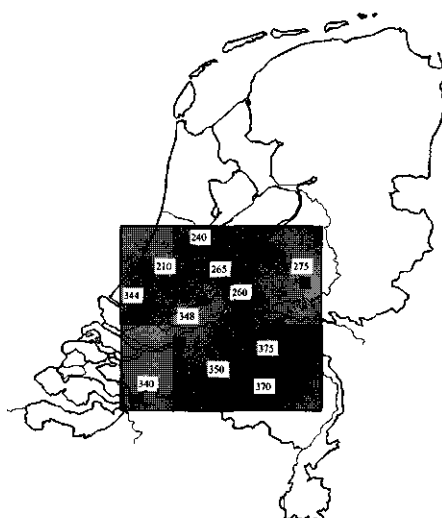


Figure 5.10: The distribution of stations for ground based remote sensing over the Cloud Detection System area

Instrument	Wavelength	Product
Lidar-ceilometer	904-911 nm	Cloud base height
Narrow beam Infrared-radiometer	9.6 - 11.5 μ m	Cloud base temperature
Pyranometer	0.3 - 3.0 μ m	Downwelling solar flux
Precipitation detector		Occurance of precipitation
Rain gauge		Precipitation amount

Table 5.1: KNMI Cloud Detection System ground station instruments

The statistical characteristics of the measured values of each 10 minute interval are obtained. The ground based instruments yield the following cloud properties directly: cloud base temperature, cloud cover fraction and cloud base height. Algorithms were developed to obtain cloud size distribution (Feijt and Van Lammeren, 1996), broadband optical thickness (Boers et al., 2000), emissivity in the infrared window and LWP for clouds of low optical depth (Bloemink et al., 2000).

5.2.1.2 Clouds and Radiation measurement campaigns

During the CDS-operational phase the CLARA-project (Van Lammeren and Feijt, 1997), an intensive measurement campaign of cloud properties, was held. The aims of CLARA were to improve retrieval methods of cloud properties for the involved remote sensing instruments. Care was taken to optimize collocation. Nine institutes were involved. The ground instruments listed in Table 5.2 were operated from Delft nearly continuously for over 50 days divided over three measurement periods in April, August and November 1996. The measurement site is indicated in Figure 5.10. Also measurements from ATSR-2, GOME and GPS were obtained. Microphysical properties were measured in situ from an aircraft during 15 flights of, in total, 40 hours. Radiosondes were launched from the Delft measurement site at 6, 12 and 18 UTC each day and every 3 hours during measurement flights.

Instrument	Wavelength	Parameter
Radar	FM-CW; 3.315GHz	Backscatterprofile
		Dopplershift
Lidar	1064nm	Backscatterprofile
	532nm	Backscatterprofile
	906nm	Backscatterprofile
microwave radiometer	20/30/50GHz	Emitted radiation
IR radiometer	9.6 - 11.5 μ m	Emitted radiation
S-VHS video camera		Sky images
IR video camera		Emitted radiation
Meteo-measurements		Temperature
		Humidity, Wind

Table 5.2. Ground instruments located in Delft during CLARA

5.2.2 Case study 1: APRIL 26, 1996; Stratocumulus

On April 26 1996 a frontal zone passed the Netherlands in the North. In Figure 5.11 the AVHRR channel 2 image at 7:44 UTC (about 7:24 LST) is presented, showing thick convective clouds in the North, a Stratocumulus field in the South and broken cloud fields in between. The Stratocumulus field is chosen for detailed analysis, because it appears to be homogeneous over a large area. This has two main advantages:

- collocation of satellite and ground based observations is relatively good
- the cloud field to a high extent resembles a homogeneous plane-parallel cloud, which is assumed in the radiative transfer calculations

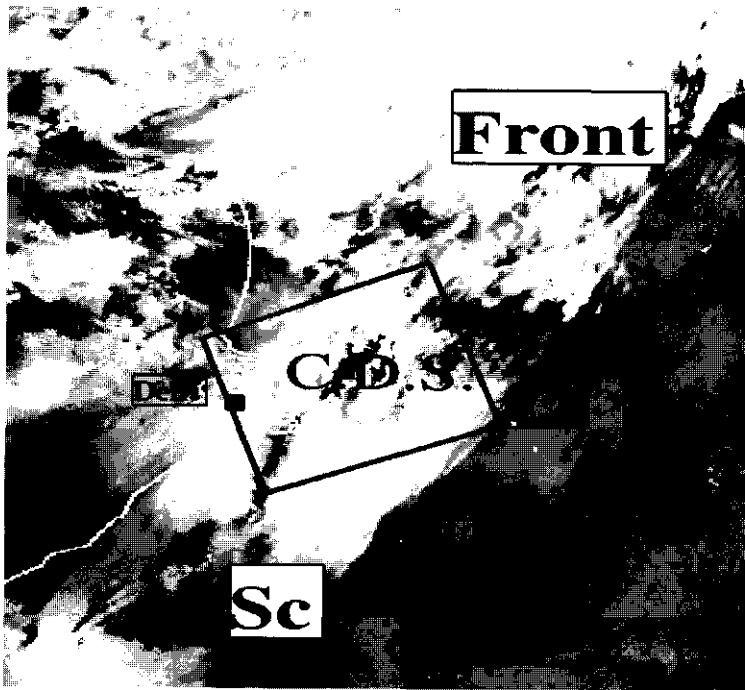


Figure 5.11: AVHRR channel 2 image at April 26, 1996: 7:44 UTC. Scaling arbitrary.

The KLAROS scheme was employed to derive cloud top temperature, optical thickness and liquid water path. At the geo-location of the measurement site at Delft, the solar zenith angle is 60° , the viewing zenith angle is 33° and the relative azimuth 9° . The cloud top temperature is compared with CDS data. Detailed analysis of LWP is done with observations from the CLARA-campaigns.

5.2.2.1 Comparison with CDS data

Cloudy pixels are identified from the AVHRR measurements using the tests described in chapter 3. A histogram of equivalent black body temperatures of cloudy pixels within the CDS-area shows values between -14 and $+11^{\circ}\text{C}$ (Figure 5.12). From these values one would expect that the cloud height is

highly variable. However, the spread can also result from sub-pixel fractional cloud cover or semi-transparency. As part of KLAROS, a test is available to select those pixels for which the $T_{10.8\mu\text{m}}$ is not expected to be affected by semi-transparency (see chapter 3.4.2). If $T_{10.8\mu\text{m}}$ minus $T_{11.9\mu\text{m}}$ is close to zero, the equivalent black body temperature at $10.8\mu\text{m}$ is likely to be representative for a cloud layer. The frequency distribution of these pixels peaks at -11 and -2°C (Figure 5.12), which indicates that there are actually two layers of limited vertical extent. From the frequency distribution, we may conclude that only a small part of the higher, colder layer is optically thick.

The cloud temperatures as obtained from AVHRR can now be compared to measurements from the CDS. Analysis of the lidar measurements at the 10 ground stations reveals two cloud layers at 1500 and 3600 m respectively. An example of the lidar measurements is given in Figure 5.14. From the ground based infrared radiometer temperatures,

the highest value in a 10 minute interval is assumed to be representative of the

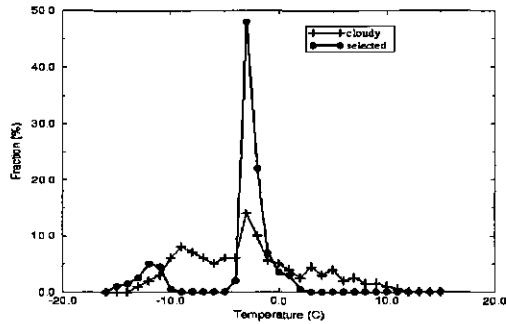


Figure 5.12: Frequency distribution of AVHRR channel 4 temperatures: all cloudy (plus); selected (dot).

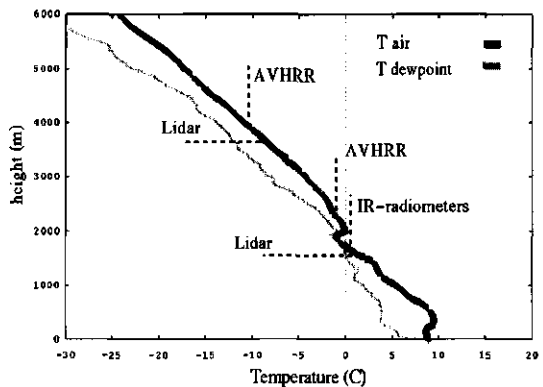


Figure 5.13: Ground versus satellite observed cloud parameters

temperature of the lowest cloud layer. The analysis of IR-radiometer measurements shows a peak at 0°C . The ground and satellite measurements can be correlated through the radiosonde temperature profile (Figure 5.13). The identified layers from ground and satellite observations coincide well. The AVHRR cloud top temperatures tend to be a little higher. This is probably caused partly by the different point of view of the instruments (the satellite measures the cloud top and the lidar the cloud base) and partly because there was no atmospheric correction applied to the measured equivalent black body temperatures. This makes the clouds appear colder in the AVHRR measurements. Automatic atmospheric correction for the whole AVHRR image is not feasible, because the calculation of the atmospheric absorption requires exact information on the height of the cloud in the atmosphere. The impact of the atmospheric absorption above the clouds was estimated from Modtran calculations on radiosonde profiles to be about 0.5°C .

5.2.2.2 Comparison with CLARA measurements

The AVHRR-measurements of 7:44 UTC were analyzed and compared with time series of the CLARA ground based instruments. In Figure 5.14 the lidar measurements for Delft are presented. The stratocumulus at 1500m, which was identified in the CDS data, is clearly visible. The layer is nearly overcast and shows low variability in time. The optical thickness as estimated from the lidar backscatterprofiles is of the order of 5 to 10. There is a second layer at about 3600m. According to radiosonde profiles the temperatures are 0°C and -10°C for the cloud layers at 1500m and 3600m, respectively. From the lidar measurements alone it cannot be decided what the cloud cover fraction of the higher layer is because the lower layer may be thick enough to fully extinguish the laser signal. At about 9 UTC the stratocumulus over Delft dissolves. After about 10:30 UTC fair weather cumuli are formed.

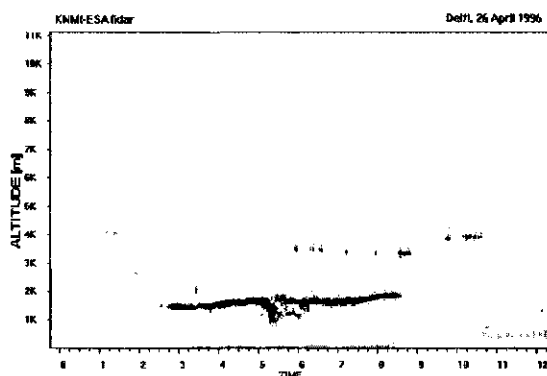


Figure 5.14: Lidar backscatter profile from 26 April.

The 3GHz radar hardly detects the lower cloud layer. From the ratio of the radar reflection and the lidar reflection the mean dropsize is estimated to be below $20\mu\text{m}$, which may be expected from non-precipitating water clouds. The higher layer is also barely visible in the

radar reflection. As the radar is very sensitive to large particles, the low reflection indicates that, although the temperature is well below the freezing point, the layer does not include large ice crystals. If there are no large crystals it is expected that there are no ice crystals at all. This is because small crystals would grow fast due to the high absolute amount of water content low in the atmosphere (Pruppacher and Klett, 1978; Heymsfield and Platt, 1984). Therefore, the higher layer is assumed to consist of supercooled water droplets.

The KLAROS scheme was employed to obtain an estimate of the optical thickness and LWP. The re-calibration of the signal (see chapter 3 for details) is a special topic here, because the measurements were done from NOAA-12, a morning orbiter, for which Rao and Chen (1996) do not give re-calibration coefficients. Therefore, the degradation rates of the sensors on board of NOAA-7, 9, 11 and 14 were applied to the NOAA-12 signal to obtain a range of values for optical thickness and LWP. The AVHRR's on these platforms are copies of the same instrument and thus their degradation rates may be expected to be similar. The cloud water model was used, because the combined information from lidar and radar indicates two layers of (supercooled) water droplets. In the vicinity of the Delft measurement site an area of about $20 \times 20 \text{ km}^2$ was selected for statistical analysis. Assuming an effective radius of $10 \mu\text{m}$ and using equation 3.10, the average LWP value was found to range from 60 to 86 g/m^2 , for the various degradation rates.

The retrieved LWP values were compared to the time-series of the microwave-radiometer of the Technical University Eindhoven that was installed at the campaign site in Delft. The microwave radiometer has a 35m wide sample area at the height of the cloud. An integration time of 5s was chosen. The collocation of time series and spatial distributions are in

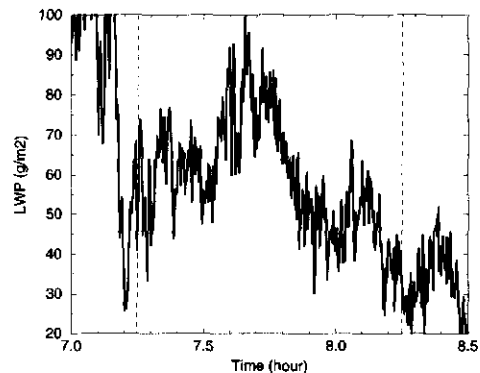


Figure 5.15: Time series of LWP as measured from ground based microwave radiometer.

general a problem to such comparisons, however, in this case the variability (in space and time) is relatively low. Values

from half an hour before until half an hour after the satellite overpass ranged from 30 to 90

g/m^2 with an average of 59g/m^2 (Figure 5.15). The accuracy of the microwave radiometer is about 10g/m^2 for this case. This is at the lower end of the range of values retrieved from AVHRR.

The frequency distribution of LWP values from the spatial distribution of the AVHRR and the time-series is shown in Figure 5.16. A moderate degradation rate is assumed. The microwave radiometer distribution is broader. This can be explained from the difference in spatial resolution of the measurements. The high resolution from the microwave radiometer enables the detection of small areas of relatively high and low values. Whereas the signal is smoothed in the IFOV of the AVHRR. Furthermore, multiple scattering of sunlight in the cloud induces horizontal smoothing, which further enlarges the AVHRR sampling area.

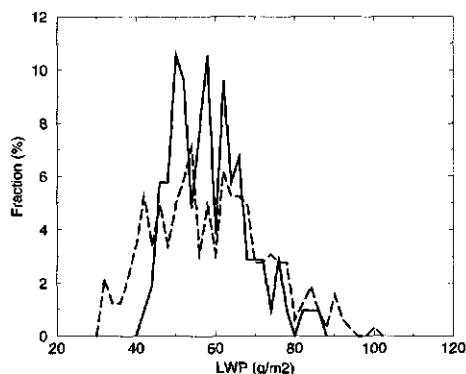


Figure 5.16: Frequency distribution of LWP as measured from AVHRR (dashed) and from microwave radiometer (solid).

On average the AVHRR retrieved values are higher than the microwave radiometer values. This cannot be caused by inhomogenities in the IFOV of the AVHRR, because that would induce the opposite effect. Inhomogeneous cloud layers reflect less light than homogeneous plane parallel clouds (Cahalan et al., 1994). The latter are assumed in the radiative transfer calculations. Therefore, the KLAROS retrieved values are expected to show a bias towards lower values of LWP instead of higher. Furthermore, as the cloud field under study is relatively homogeneous, this bias would be small. Obviously, one or more assumptions in KLAROS is not valid for the cloud field under study. In the following we will discuss the micro-physical measurements, which were done during this day.

Aircraft measurements were done from 7:10 until 9:30 UTC. Tracks were flown near Delft and through the stratocumulus South of Delft. In Figure 5.17 the droplet size distribution, as measured with the FSSP on board of the aircraft, is shown. The distribution is narrow with a mode radius of $4\mu\text{m}$, and effective radius of $6.3\mu\text{m}$. The drop sizes are in agreement with the

estimate from the ratio of radar and lidar reflectivity. Along the flight track the droplet size distribution is extremely homogeneous. Also in this respect the stratocumulus field does resemble the model homogeneous plan parallel cloud to a high extent. The number of droplets per volume however, varies considerably, which implies vertical or/and horizontal water content variations.

The measured drop size distribution is similar to the Deirmendijan C1-type, which was used in the radiative transfer calculations. This gives some confidence in the results. However, the measured effective radius differs considerably from the one used in the LWP retrieval (equation 3.10). The

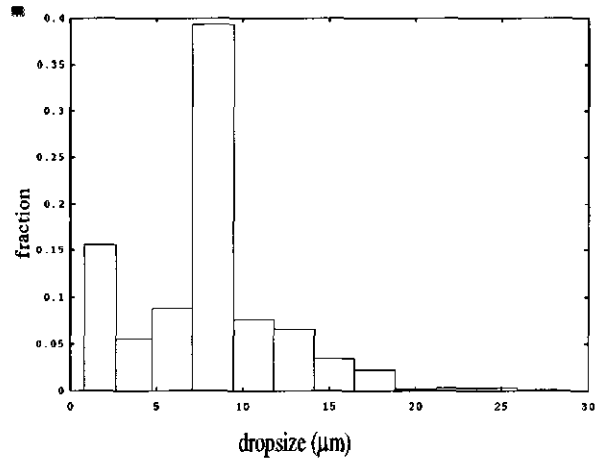


Figure 5.17: Drop diameter distribution of the stratocumulus field as measured from aircraft based FSSP on April 26 1996.

measured effective radius is $6.3\mu\text{m}$, whereas $10\mu\text{m}$ is used in the retrieval. If the measured values are

used in the LWP retrieval, the values range from $38 - 54 \text{ g/m}^2$, with an average of 46g/m^2 , instead of $60 - 86\text{g/m}^2$. The microwave radiometer measurements have an average of 59g/m^2 . So, the AVHRR retrieved value is 9 to 36% too low depending on the re-calibration coefficients used.

5.2.2.3 Discussion and Conclusions

Cloud properties as measured from AVHRR and ground are compared for a stratocumulus field. Cloudy pixels were identified from the AVHRR image. It was found that the distribution of equivalent black body temperatures at $10.8\mu\text{m}$ is not representative for the vertical distribution of cloud layers in this case. The semi-transparent test (equation 3.3), was successfully applied, which yielded the identification of two cloud layers, which were also observed from the 10 CDS stations for ground based remote sensing. This study shows that the semi-transparency test functions well.

Also the retrieval of LWP was evaluated. In this particular case the real world cloud field resembles the assumptions in our model calculations to a high extent. The droplet size distribution as measured from aircraft is similar to the one used in the calculations and is very homogeneous along the flight track. However, there are considerable number density variations.

The distribution of retrieved LWP values from AVHRR and microwave radiometer are similar except for the extreme high and low values. The average value retrieved from AVHRR is significantly higher than that from the microwave radiometer if the effective radius is assumed to be $10\mu\text{m}$. If the measured effective radius is used in the retrieval, the AVHRR values are significantly lower than the microwave radiometer. However, a small bias towards lower values was expected due to the horizontal variability of LWP within one IFOV of the AVHRR.

The two largest sources of uncertainty in this analysis originate from the collocation of ground based and satellite data and the calibration of the AVHRR $0.6\mu\text{m}$ channel. The latter causes the lowest estimate (38g/m^2) to be 70% of the highest estimate (54g/m^2). This limits the validation of the retrieval method considerably.

Within the limitation of the comparison of ground based and satellite based observations the results give confidence in the methods for retrieving cloud presence, cloud top temperature and optical thickness. The retrieval of LWP is proven to be very sensitive to the assumed effective drop size. Furthermore, this study shows that accurate comparisons of ground based and satellite based measurements are difficult due to the high variability of cloud properties both in time and space.

5.2.3 Case study 2: April 17, 1996: cirrus

On this day a front passed the Netherlands from the Southwest to the Northeast. In Figure 5.18. the Meteosat infrared images of the area at 6, 9, 12 and 15 UTC are shown. Between 6 and 15 UTC the cloud cover over the Netherlands increases to overcast. There is one single AVHRR overpass at 13 UTC, which we analyse. The AVHRR image from the $10.8\mu\text{m}$ channel is displayed in Figure 5.19. The AVHRR image shows the same features as the Meteosat, but in much greater detail. The temperatures seem to vary smoothly in the Meteosat image, whereas small structures can be identified in the AVHRR image. This difference is mainly due to the higher spatial resolution of the AVHRR, since the spectral response functions of the infrared channels of Meteosat and AVHRR are similar.

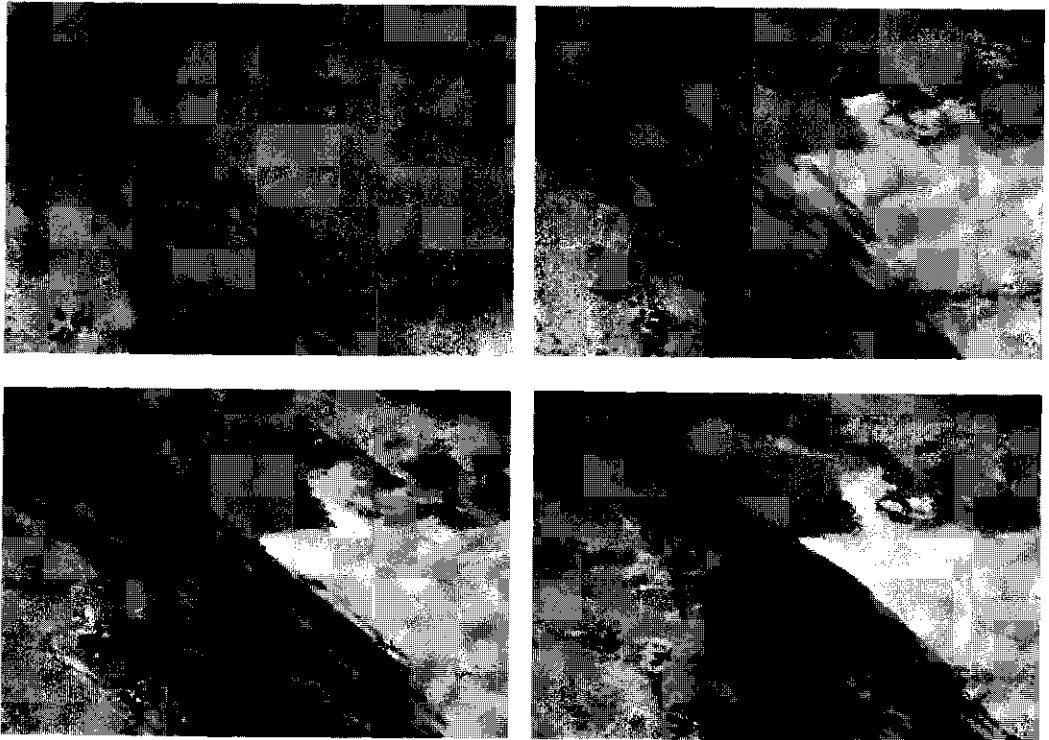


Figure 5.18: Meteosat infrared images from April 17 1996 at 6, 9, 12 and 15 UTC respectively. Scaling: 240K < , black < T < white, 300K



Figure 5.19: AVHRR channel 4 image from April 17 at 13 UTC.
Scaling: black, $240\text{K} < T < 300\text{K}$, white.

The vertical profiles of the 3GHz radar at Delft are shown in Figure 5.20. From the edge of the front at 8UTC until the time of overpass of the AVHRR (13UTC) the cloud base height decreases from about 7km to 5.5km. The radar measurements support the conceptual model of a front for this case. The clouds at the edge are expected to have a high altitude and a relatively small vertical extent.

If the clouds at the edge are thin, they are expected to be semi-transparent in the $10.8\mu\text{m}$ channel of the AVHRR. As these clouds have a much lower temperature than the surface, we may expect the $10.8\mu\text{m}$ channel temperatures to be much higher than the actual cloud top temperatures. In the following we use KLAROS to retrieve the emissivity of the clouds and make an estimate of the actual cloud top temperature, thus correcting for the semi-

transparency. The retrieved cloud parameters are compared to estimates from collocated radar and radiosonde measurements over Delft.

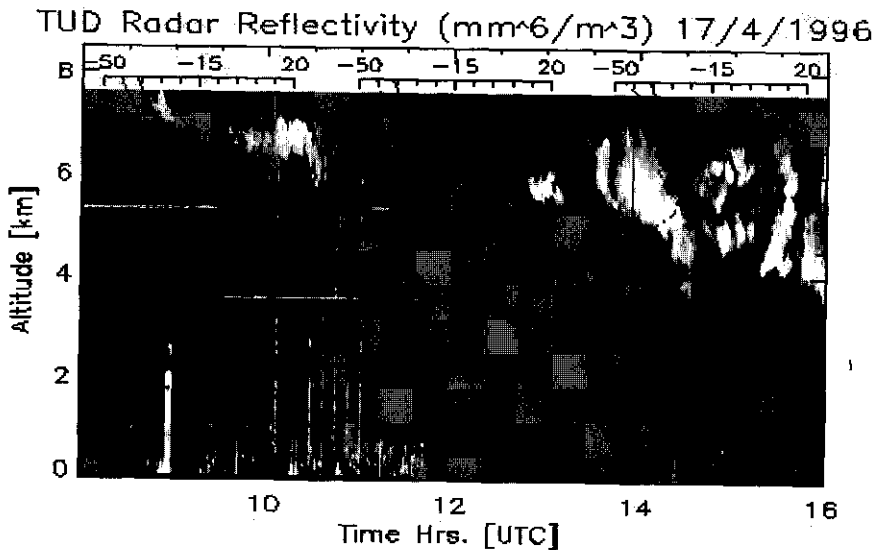


Figure 5.20: CLARA radar measurements from April 17, 1996.

The KLAROS scheme is employed to identify cloudy pixels. The viewing zenith angle is 25° , the solar zenith angle is 45° and the relative azimuth 72.5° . The scheme does well for cirrus and is capable of detecting both large and small cloud amounts, because the temperature test and the semi-transparency test are complementary. Cirrus with low optical thickness is well identified with the semi-transparency test (equation 3.3), whereas optically thick cirrus is well identified by the low temperatures. The reflectivity test does not add much to the detection efficiency, because thin cirrus do not contribute much to the reflection of sunlight. The results of the cloud detection test are visualized in Figure 5.21.

In KLAROS, the reflectivity at $0.6\mu\text{m}$ from the cloudy pixels are matched with tabulated results from radiative transfer calculations for cirrus clouds to obtain estimates for the optical thickness at $0.6\mu\text{m}$. This information is used to derive:

- optical thickness at $10.8\mu\text{m}$ (equation 3.5),
- cloud emissivity (equation 2.4)
- cloud temperature (equation 3.6).

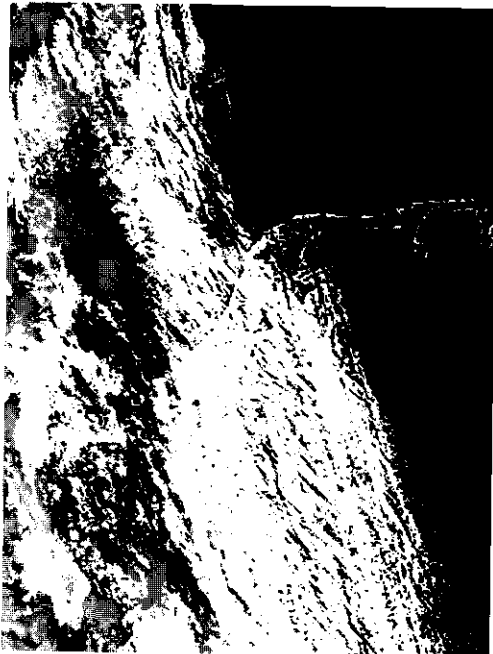
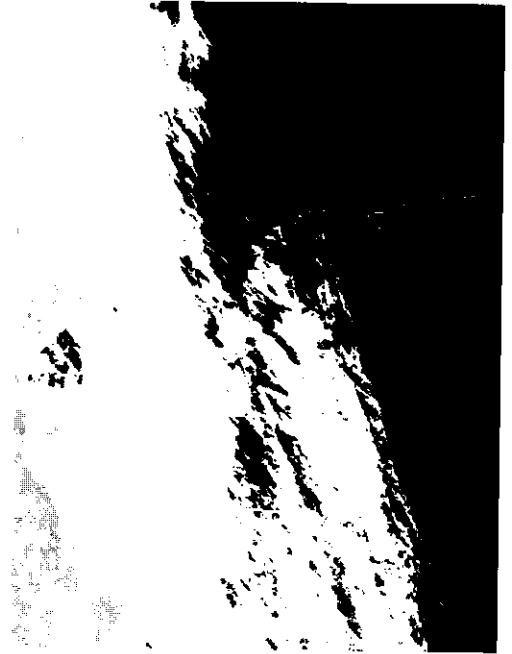
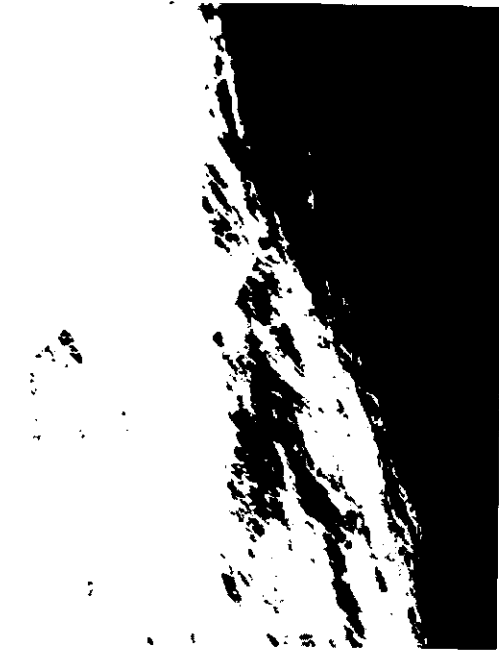


Figure 5.21: Cloud masks from: a) temperature test; b) reflectivity test; c) semi-transparency test.

The surface temperature is estimated from visual inspection of the AVHRR $10.8\mu\text{m}$ image, and information from the HIRLAM numerical weather prediction model. The surface reflectivity is estimated using a 2 year data base of AVHRR measurements, and visual inspection of the AVHRR $0.6\mu\text{m}$ image of the same day and other recent overpasses. The estimates of the surface radiative properties are described in more detail in chapter 3.

5.2.3.1 Comparison with CLARA data

In order to compare AVHRR and radar retrieved parameters, an area in the AVHRR image is chosen for which it may be expected that it corresponds to the ground based measurements from 9 until 13UTC (Figure 5.20). In general, the selection of an area in a satellite image, which is to be compared with a part of a time series is a subjective and difficult choice. This requires understanding of the atmospheric conditions. In this particular case, the frontal zone is chosen as a reference. It may be expected that the cloud processes are mainly driven by large scale lifting and do not strongly interact with the surface because they take place at 6 – 8km height. In the first stage, clouds are formed at high altitudes. As the front evolves, cloud base height decreases. Thus, the stage of the front at one location and time can be identified by the cloud base height. The movement of air-masses is indicated by the advection of the whole front. The edge of the front is always in the first stage. Therefore, we compare the time series of ground based measurements at one location with an area in the AVHRR image which is elongated in the direction of the movement of the front. The advection of the front from 9 to 13UTC is estimated from the time series of Meteosat images. The analysis area is indicated in Figure 5.19.

5.2.3.2 Emissivity

In this paragraph the results of two retrieval methods of emissivity are compared. The first method is part of KLAROS and is described in chapter 3. It uses the measured reflectivity at $0.6\mu\text{m}$ to obtain the optical thickness at $0.6\mu\text{m}$, from which the emissivity is derived. The method is most sensitive to assumptions regarding: surface reflectivity, ice crystal phase function and calibration.

The second method uses measurements at $10.8\mu\text{m}$ and requires the actual cloud top temperature and surface temperature. The equivalent blackbody temperature as measured at $10.8\mu\text{m}$ is the weighted average of contributions from the surface and the cloud. The emissivity is the weighting factor that can be obtained using the inverse of equation 3.6. The

results from this method are most sensitive to the assumptions regarding cloud top temperature and surface temperature (Van Lammeren and Feijt, 1997). The results of this method will be called the reference values. The two methods are sensitive to different assumptions and thus are to a high extent independent.

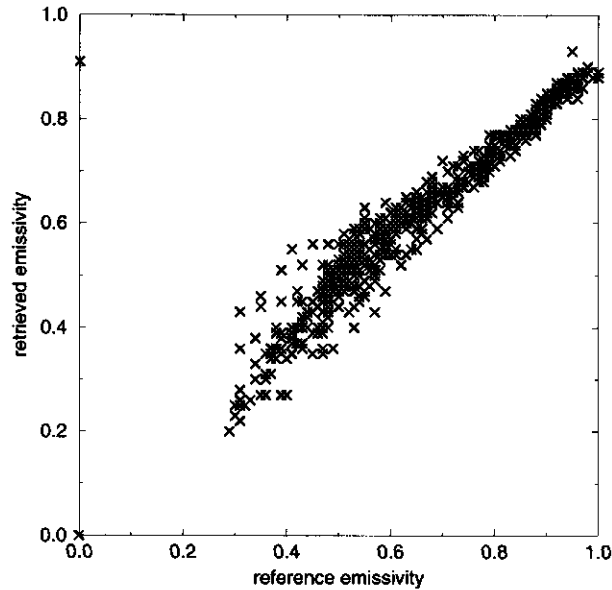


Fig 5.22: Retrieved emissivity versus reference emissivity

The actual cloud top temperatures, which are required for the reference method, are obtained from the radar and radiosonde data. From the radar data we estimate a minimum and maximum cloud top height to be 6 and 8km respectively, which correlate to cloud top temperatures of 248K and 233K. For each pixel the estimate of the minimum reference emissivity is obtained from the minimum reference temperature (233K) and the estimate of the maximum reference emissivity is obtained from the maximum reference temperature (248K). Therefore, the emissivity derived from KLAROS for each individual pixel is considered correct if the retrieved emissivity is between the minimum and maximum estimates.

The retrieved optical depths at $0.6\mu\text{m}$, $\tau_{0.6\mu\text{m}}$, range from 0.5 to 4. The absorption optical thickness at $10.8\mu\text{m}$, $\tau_{10.8\mu\text{m},\text{abs}}$, is half of $\tau_{0.6\mu\text{m}}$ and ranges from 0.25 to 2. The corresponding emissivity ranges from 0.3 to 0.9. In Figure 5.22 a scatter plot of retrieved and reference emissivity is given. The center of the temperature range, 241K, is chosen as the reference temperature and is assumed to be the best estimate. The scatter plot shows that the retrieved emissivity values are smaller than the reference values for larger values. The points in this part of the scatter plot are well organized along a line, with high density and low scatter. For small emissivities the retrieved values and reference values are similar. However, the scatter is significantly higher. This shows the limitations of the detection test. Apparently, it is not possible to detect clouds with $\tau_{10.8\mu\text{m},\text{abs}} < 0.25$ in this case. The larger value, 0.9, indicates that according to our analysis there are no optically thick clouds in the selection area. This is confirmed by the selection test (equation 3.4), which indicates that there are no pixels within the area for which the measured equivalent black body temperature is representative for the cloud layer. So, even the lowest measured temperature is higher than the actual cloud top temperature.

On the other hand, we may expect that the retrieved emissivity is an underestimate, because only the absorption at $10.8\mu\text{m}$ is taken into account, while actually the emissivity is enhanced by scattering (section 2.3). According to Minnis (1991) the underestimate is small (1 to 10%) and even negligible for $\tau_{10.8\mu\text{m},\text{abs}} < 1$, but can be significant for $1 < \tau_{10.8\mu\text{m},\text{abs}} < 4$. The scatterplot of reference and retrieved emissivities (Figure 5.22) has such a signature. However, it may very well be that the signature of the scatter plot reflects the structure of the cloud field studied. There may be a correlation between cloud top temperature and emissivity. For example, cold clouds may be relatively optically thin in the selected area. This limits the extent of our conclusions.

The large scatter for optically thin clouds can be explained from the larger contribution of the surface to the signal both in the $0.6\mu\text{m}$ and the $10.8\mu\text{m}$ channels. If the assumed values of surface reflectivity and temperature are in error this will contribute to the error in both the retrieved and the reference emissivity. Small sheets of water that are not included in the land/sea mask, for example, have surface properties that deviate from the average values, which are used in the retrievals. This affects the results of both retrievals. The $0.6\mu\text{m}$ reflectivity is relatively low for small sheets of water, and thus the first method gives an

underestimate of the optical thickness and emissivity. As small sheets of water are relatively cold, the second method gives an overestimate. These effects contribute to the scatter for optically thin clouds.

The average retrieved emissivity is 0.64. The reference emissivities are 0.61, 0.68 and 0.71 for reference temperatures of respectively 233, 241 and 248K. Figure 5.23 shows histograms of the difference between retrieved and reference emissivities. All retrieved values are within 0.25 of the reference values. The retrieved emissivity shows a bias of -0.03 , 0.04 and 0.07 for the maximum, best and minimum estimate respectively. The root mean square (rms) of the differences between retrieved and reference emissivity are 0.04, 0.06 and 0.12, with an average of 0.07.

The values presented here are indications of the upper boundaries of the emissivity error, because the width is partly due to errors in the reference temperatures and partly due to errors in the retrieval. In case of small sheets of water the methods have opposite biases, which results in an overestimate of the error. However, it is possible that in some conditions both methods have the same bias, which results in an underestimate of the error. Therefore, we

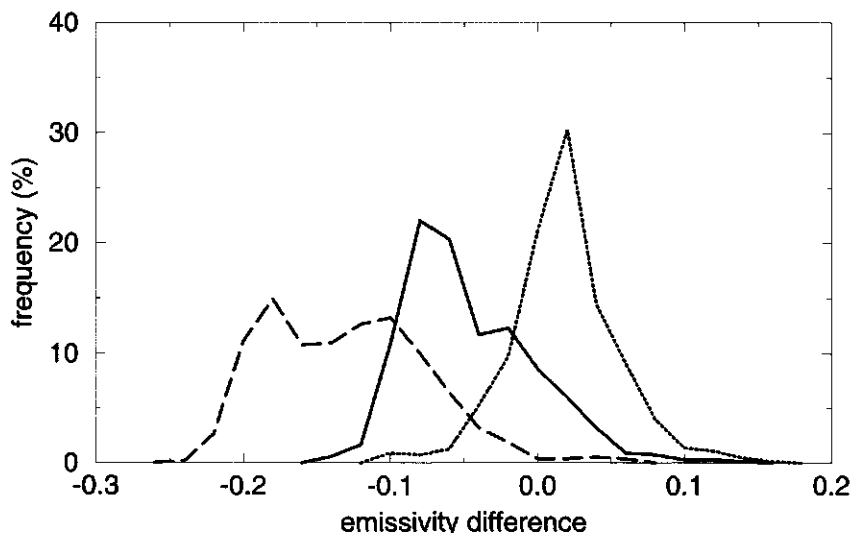


Figure 5.23: Distribution of the difference between emissivity retrieved from reflectivity at $0.6\mu\text{m}$ and from the equivalent black body temperature for a reference temperature of: 233K (dashed), 242K (solid) and 248K (dotted).

may conclude that the accuracy of our estimate of emissivity from AVHRR is better than 0.1 for this case study.

5.2.3.3 Cloud top temperature

From the cloudy pixels in our collocation area a frequency distribution of equivalent black body temperatures at $10.8\mu\text{m}$ is made (Figure 5.24). The temperatures range from 240 – 270K. The average temperature is 257.4K, which is well outside of the range of the reference temperatures (233 to 248K). The measured temperatures indicate clouds that occur at altitudes from the ground up to 6.5km height. Obviously, the $10.8\mu\text{m}$ equivalent black body temperatures are not representative for the cloud layer. From the selection test results, it is clear that all, even the lowest measured temperatures, are higher than the actual cloud top temperatures.

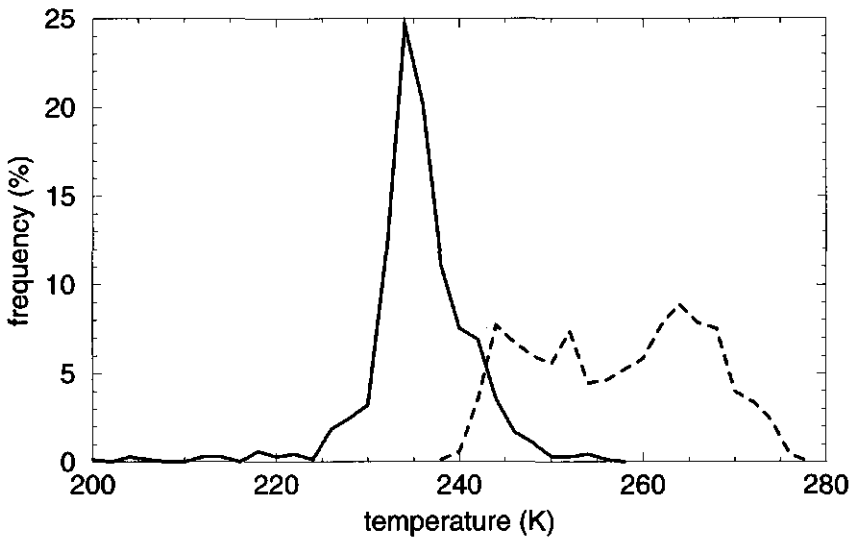


Figure 5.24: Distribution of temperature as retrieved from KLAROS (solid) and as measured (dashed).

The distribution of corrected cloud temperatures is shown in Figure 5.24. The values range roughly from 230 to 250K, with an average of 235.6K. The average is relatively low in the range of reference temperatures (233-248K). Note that the average temperature is sensitive to the selection area and thus the similarity of reference and average retrieved temperature is

only an indication of the accuracy. The peak of the distribution is at 233K, which is at the low end of our reference values. Probably, the retrieved temperatures are a few degrees too low. This could be due to the neglect of scattering effects in our retrieval. It could also be that the scattering phase function applied, is not accurate for this case. We found that, if the water cloud phase function is used, the retrieved optical thickness is significantly higher and thus the retrieved cloud top temperatures are higher. It would take in situ measurements of the crystal shape and size to clarify this issue.

A number of extremely low values are present. Inspection of the measurements show that these originate from measurements over small lakes with low reflectivity, which are not included in the land/sea mask. These outliers are not removed from the analysis of the quality of the retrieval.

Another cloud field characteristic is the variability of the cloud top temperature, which can be estimated from the width of the distribution. The width of the distribution of equivalent black body temperatures as measured from satellite gives an overestimate, because it is broadened by semi-transparency. The spread is partly caused by the variability of optical thickness and partly by the variability of cloud height. The optical thickness is variable at small scales because it is subject to small scale cloud processes. The cloud height variability is limited by the physical phenomena that caused the clouds to condense. Therefore, we may expect that the variability of the measured temperatures is higher than that of the corrected temperatures. This indeed is the case. The width of the distribution as defined by the root mean square difference between value and average is 9.1 for the measured temperatures and 7.3 for the corrected temperatures, even though the outliers were not excluded.

5.2.3.4 Conclusions

Ice clouds are often optically thin, semi-transparent. Therefore, it is difficult to estimate the actual cloud top temperature directly from the measured radiances. In this section it is shown that with the KLAROS scheme it is possible to improve the estimate of cloud temperature through the retrieval of optical thickness and emissivity from $0.6\mu\text{m}$ radiances. The quality of the retrieved cloud properties is evaluated using combined information from radar and radiosondes from the CLARA campaigns. The retrieved emissivity values ranged from 0.3 to 0.9. The bias relative to the reference emissivities can be positive or negative, with a maximum of 0.07. The rms difference between retrieved and reference emissivity varies

between 0.04 and 0.12. The retrieved emissivity values are used to obtain a corrected cloud top temperature. On average the difference between measured and retrieved cloud top temperature is 17K. Probably, the retrieved temperatures are a few degrees too low. Still, this largely improves the estimate of the cloud temperature. In conclusion, the KLAROS scheme enables retrieval of values for emissivity and cloud top temperature, which are accurate within the accuracy of our reference values.

5.3 Concluding remarks

The studies presented in this chapter give an indication of the quality of the satellite retrieval methods. Furthermore, it shows that information from ground based remote sensing instruments is required to get a full description of the cloud field. The Meteosat detection scheme does well for most conditions. However, low clouds during the night and scattered clouds (cloud fraction of 1-3 octas) are sometimes not identified. The measured thermal radiance is not representative for a cloud layer in case of semi-transparent clouds and partly cloudy cases. The Meteosat visible channel is not suitable for detailed quantitative analysis due to its broad spectral band and the corresponding high surface reflectivity. The AVHRR detection scheme does well for semi-transparent clouds, mainly due to the split window channels. However, even at the scale of the AVHRR instantaneous field of view, scattered clouds may be missed.

The rather narrow spectral band of the 0.6 μ m channel enables estimates of optical thickness for both water and ice clouds. The studies show that for ice clouds the estimate of cloud temperature can be improved significantly. Whereas the retrieval of liquid water content of stratiform water clouds seems feasible, provided that the correct effective radius is applied. The comparison of ground based and satellite measurements also shows that clouds have a high variability both in time and space. Therefore, the collocation of time-series at one location and spatial distributions at one moment in time, requires interpretation of the atmospheric conditions and the signature of the cloud fields. In the next chapter, an attempt is made to quantify the signature in both time-series and spatial distribution using the spectral analysis formalism. The AVHRR analysis environment is employed to obtain the spatial distribution of liquid water path, whereas ground based microwave radiometer measurements were analyzed to obtain time-series.

References

- Barkstrom, B. R., and G. L. Smith, 1986: The Earth Radiation Budget Experiment: Science and implementation. *Rev. Geophys.*, 24, 379-390.
- Bloemink, H.I., A.C.A.P. van Lammeren, A.J. Feijt and S. Jongen, 1999. Active-passive sensor synergy for cloud observation; IR cloud properties and cloud liquid water. *J.Geophys.Res.* (submitted).
- Boers R, A. Van Lammeren and A. Feijt, 1999: Accuracy of cloud optical depth retrievals from ground based pyrometers. *Journal of Atmospheric and Oceanic Technology* (accepted)
- Cahalan, R.F., W. Ridgeway, W.J. Wiscombe, S. Gollmer and Harshvardhan, 1994: Independent pixel and Monte Carlo estimates of Stratocumulus albedo. *J. Atmos. Sci.*, 51, 3776-3790.
- Cahalan, R.F. and J.H. Snider, 1989: Marine StratoCumulus structure. *Remote Sens. Environ.* 28, 95-107.
- Cess, R. D., et al., 1989: Interpretation of cloud-climate feedback as produced by 14 atmospheric general circulation models. *Science*, 245, 513-516.
- Cheruy, F., and R. S. Kandel, 1991: Use of Meteosat data for validation of the diurnal variation of the outgoing longwave radiation produced by ERBE. *Dyn. Atmos. Oceans*, 16, 73-84.
- Feijt A. and A. van Lammeren, 1996: Ground-based and satellite observations of cloud fields in the Netherlands. *Monthly Weather Review*, 124, 1914-1923.
- Feijt, A. J., 1992: The earth radiation budget: Overview of data-processing and error sources. KNMI TR-146, 31 pp.
- Gesell G., T. Konig, H. Mannstein, and K. T. Kriebel, 1993: SHARK-APOLLO quantitative satellite data analysis based on ESRIN/SHARP and DLR/APOLLO. *Proc. of the Sixth AVHRR European Data Users' Meeting*, Belgirate, Italy, Eumetsat, 583-587.
- Gustafsson, N., 1993: HIRLAM 2 Final Report. SMHI Tech. Rep. 9, 126 pp.
- Heymsfield, A.J. and C.M.R. Platt, 1984: A parametrization of the particle size spectrum of ice clouds in terms of the ambient temperature and the ice water content, *J. Atm. Sci.*, 41, 846-855.
- Kastner, M., K. T. Kriebel, and H. P. Schickel, 1993: Alpine cloud climatology--First results. *Proc. Sixth AVHRR European Data Users' Meeting*, Belgirate, Italy, Eumetsat, 253-257m

- Klein, S. A., and D. L. Hartmann, 1993: Spurious changes in the ISCCP dataset. *Geophys. Res. Letters*, 20, 455-458.
- Kneizys, F. X., E. P. Shettle, W. O. Gallery, J. H. Chetwynd, L. W. Abreu, J. E. A. Selby, S. A. Clough, and R. W. Fenn, 1988: Users guide to Lowtran-7. Air Force Geophysics Laboratory AFGL-TR-88-0177, 200 pp.
- Lammeren, A.C.A.P. van and A.J. Feijt, 1997. The emissivity of Cirrus clouds derived from LITE and Meteosat measurements. Selected Papers of the 18th International Laser Radar Conference (ILRC), Berlin 22-26 July 1996, published by Springer Verlag New York Berlin-Heidelberg (ISDN 3-540-61887-2) pp. 201-204.
- Lammeren A.C.A.P. van, and A.J. Feijt, 1997: Cloud research in the Netherlands: CLARA, *Change*, 34, NRP, Bilthoven, 10-13.
- Lovejoy, S., and D. Schertzer, 1990: Multifractals, universality classes and satellite and radar measurements of cloud and rain fields, *J. Geophys. Res.*, 95, 2021-2034.
- Pruppacher, H.R. and J.D.Klett, 1978: Microphysics of clouds and precipitation, D. Reichel Publ. Co, Dordrecht, Holland, 714pp.
- Ramanathan, V., R. D. Cess, E. F. Harrison, P. Minnis, B. R. Barkstrom, E. Ahmad, and D. Hartmann, 1989: Cloud radiative forcing and climate: Results from the Earth Radiation Budget Experiment. *Science*, 243, 57-63.
- Rao, N.C.R. and J. Chen, 1996: Post launch calibration of the visible and near-infrared channels of the Advanced Very High Resolution Radiometer on the NOAA-14 spacecraft. *Int. J. Rem. Sens.*, 17, 14, 2743-2747.
- Stammes, P., A. Feijt, A. van Lammeren and G. Prangma, 1994: TEBEX observations of clouds and radiation – potential and limitations. KNMI TR-162, KNMI, De Bilt.

6. Comparison of scaling parameters from spatial and temporal distributions of cloud properties

In chapter 5 cloud field characteristics from time-series of ground based measurements and spatial distributions from satellite were compared. A part of the time-series is compared to an area in the satellite image. For a one-to-one comparison the only data available is the ground based measurement at the time of satellite overpass compared to the one pixel in the satellite image that includes the location of the ground based station. Even this single direct comparison is not unambiguous, because the integration area of the satellite instrument is much larger than the sampling volume of the ground based instrument. The instruments do not measure the same volume of the cloud field. Therefore, the comparison is of a statistical nature. The choice of the period in the time-series and area in the satellite image that are compared is made on qualitative reasoning. For each case study the cloud field is analyzed. The horizontal extent and the evolution of the cloud field in time are estimated. If the signature of both data sets is similar the comparison is allowed.

In this chapter an attempt is made to quantify the signature of the cloud field in term of its scaling properties. It is investigated for two cases if the scaling properties from time-series and satellite images are comparable. It is a first step towards automated selection of periods in time-series and areas in satellite images that correspond to the same cloud field.

6.1. Comparison of scaling parameters from spatial and temporal distributions of cloud properties*

Abstract

The most common method to evaluate the quality of cloud parameter retrievals from satellite data is comparison with time series of ground based measurements. For highly variable cloud parameters like liquid water path (LWP), however, a direct comparison of spatial and temporal distributions has limited value. It is questionable which period in the time series is representative of an area in the satellite image. A necessary but not sufficient boundary condition for statistical analysis is that the variability of both sub-sets is similar.

In this paper, we study the variability in terms of scaling properties of both spatial distributions and time-series of LWP and focus on the relation between them. The time-series are obtained from ground based microwave radiometer measurements at 1Hz. The spatial distributions are derived from AVHRR 0.6 μ m radiances. It is shown that the scaling properties of both distributions are similar for a Stratocumulus field, which exhibits scale invariance, and for a Cumulus field for which scales of preference were identified. A double logarithmic representation was appropriate to obtain the spectral exponent. A log-linear representation was appropriate to identify a scale of preference. In the Cumulus case it was possible to calculate a feasible conversion factor to map variability in time to variability in space. This enables an estimation of the spatial variability at very high resolutions.

*) This section was accepted for publication in this form.

Feijt, A. and H. Jonker, 2000: Comparison of scaling parameters from spatial and temporal distributions of cloud properties. *J. Geophys. Res.* (in press)

6.1. Introduction

Cloud processes act on a wide range of spatial scales, from micrometer scale (radiative cooling) to 100km for large scale lifting in a frontal zone. In general, the spatial scales and temporal scales of cloud related processes are linked by the underlying physical process. Depressions are of the order of 1000km and have a life cycle of several days, while turbulence of 1 km scale has a life cycle of the order of tens of minutes. Cloud parameters also show variability on all scales in time and space. As a consequence, when interpreting time series from ground based measurements, we should be aware of the time scale of analysis relative to the natural variability of the cloud field parameter. For example: The cloud top temperature of a field of boundary layer clouds changes gradually through the day, because it is limited by the boundary layer height. Therefore a single instantaneous value is sufficient to characterize this cloud field parameter. However, the water content of fair weather cumuli changes from zero to its maximum value in only a few minutes. Therefore, an instantaneous measurement is not representative for the cloud field [Stull, 1988]. The natural variability of cloud processes also shows in measurements of spatial distributions. If the cloud field parameter has a low spatial variability, like cloud top temperature of boundary layer clouds over flat grassland, the measurement at one location is representative for a large area. However, in a Cumulus field the water content is highly variable. The measured water content at one location at one moment in time is not representative for any other location or time. Therefore, for direct comparison of values from a time series of ground based measurements and a spatial distribution at one moment in time there is only one value available. A time to space conversion, as in the concept of Taylor's hypothesis of an advected frozen atmosphere, has limited validity here, because condensation and evaporation cause variability of liquid water content at small time and space scales. However, we may expect that the variability as measured in time is reflected in the variability in space since both quantities relate to the same cloud processes. This may give us a handle on comparisons of time series and spatial distributions.

In this paper we compare cloud field parameters as measured from satellite with time series of ground based measurements. The time series of vertical integrated liquid water under study are derived from microwave radiometer measurements at one second resolution as measured during the Clouds and Radiation intensive measurement campaigns (CLARA), which took place in April, August and December 1996 in the Netherlands. The spatial distribution is

derived from the Advanced Very High Resolution Radiometer (AVHRR) on board of the NOAA polar platforms 12 and 14, which has a maximum sub-satellite resolution of 1 km.

In order to get insight into the variability, we study the variance spectrum, which is a complete decomposition of the variance in terms of contributions per temporal or spatial scale. Analysis of the scaling properties of a signal reveals whether it is scale invariant, exhibits a scale break, or whether there is a distinct scale of preference. The scaling properties convey useful information of the underlying physical process, and could be regarded as its signature, which manifests itself both in time series and spatial distributions. If the scaling properties of the two measured distributions are similar, a comparison of statistical properties may be possible.

In section 6.1.2, scaling parameters, as derived from the spatial and temporal distributions, will be presented in a double logarithmic representation for two cases: a StratoCumulus field in which the cloud field properties reveal scale invariance (no scale of preference), and a Cumulus field for which there is no scale invariance. In section 6.1.3, the Cumulus case will be analyzed in depth using a log-linear representation. Scales of preference are identified in both the time series and the spatial distribution and their values are compared. A conversion factor to link time scales to spatial scales is derived. The results are discussed in section 6.1.4. In section 6.1.5 the conclusions are summarized.

6.1.2. Comparison of scaling parameters from spatial and temporal distributions

6.1.2.1 The CLARA data set

CLARA is an intensive measurement campaign on clouds and cloud-radiation-interactions held in the Netherlands in 1996. Nine institutes from the Netherlands and the U.K. were involved [Van Lammeren et al., 1998]. During 50 days in three different seasons, instruments for ground based remote sensing were operated continuously from a location in Delft (52 North, 4 East). Great care was taken to optimize collocation between the ground instruments. Microphysical properties were measured in situ from an aircraft during 15 flights yielding 40 hours of data. Radiosondes were launched from the Delft site at 6, 12 and 18 UTC each day and every 3 hours during aircraft flights. The instruments involved are listed in Table 1.

Instrument	specification	parameter
Radar	3.315 GHz	Reflectivity, Doppler shift
Lidar	532, 906 and 1064nm	Reflectivity
Microwave radiometer	20, 30 and 50GHz	Water Vapor Column Liquid Water Column
Infrared radiometer	9.6 – 11.5 μm	Cloud base temperature
Infrared video camera	8-12 μm	Qualitative
Visible S-VHS video camera	Visible	Qualitative
Meteorological instrumentation		Temperature, humidity and wind

Table 6.1: Instruments involved in CLARA

6.1.2.2 AVHRR analysis

The KNMI environment to retrieve LWP from AVHRR 0.6 μm radiances consists of two steps: discrimination of cloud free and cloudy pixels, the cloud detection step, and the interpretation of reflectances of cloudy pixels in terms of liquid water path. The cloud free areas are identified with a cloud detection algorithm. A derivative of the widely used APOLLO-scheme [Saunders, 1986; Saunders and Kriebel, 1988] is applied here. The reflectivity of cloudy pixels is compared to pre-calculated values from a doubling-adding type radiative transfer model [Koelemeijer et al., 1995; Feijt et al., 1999]. The calculations were performed for a large number of values of optical thickness, solar zenith angle and surface reflectivity. The results were stored in look-up tables. The model assumes fully cloudy pixels with plane parallel homogeneous water clouds of a fixed optical thickness. The size distribution of the water droplets is modeled with a gamma distribution with a mode radius of 6 μm following [Deirmendjian, 1972]. The cloud is assumed to be at 2 km height in a Midlatitude Summer atmosphere [McClatchey, 1969]. The best matching reflectivity in the look-up tables is assumed to represent the best estimate of the optical thickness.

6.1.2.3 Spectral analysis

We study the variance spectrum of the cloud properties. The variance spectrum provides an exact decomposition of the variance in terms of contribution per scale either in time, denoted by the frequency (f), or in space, denoted by the wave number (k). If the variance is

dominated by a scale, this can be identified by a peak in the variance spectrum. The variance is defined to be the average of the square of the deviation from the mean. The measured time dependent variable is denoted, $p(t)$ where $\langle p(t) \rangle$ denotes the mean. The departure from the average is $\Delta_p(t) = p(t) - \langle p(t) \rangle$.

The variance is:

$$\langle [\Delta_p(t)]^2 \rangle \sim \int [\Delta_p(t)]^2 dt = \int E_p(f) df \quad (1)$$

where $E_p(f)$ represents the variance spectrum, which is the squared modulus of the Fourier transform of $\Delta_p(t)$. The decomposition of a spatial distribution, $q(x,y)$, in contributions at specific spatial scales in terms of Fourier components, $E_q(k)$, is analogous to equation (1). The variance spectrum, $E_q(k)$, is then derived from the squared modulus of the Fourier transform of $\Delta_q(x,y)$ followed by an angular integration in Fourier space [Lovejoy et al., 1993].

The distribution is scale invariant if, in the plot of $\log(E_p(f))$ to $\log(f)$, the values exhibit a straight line. This implies that $E_p(f)$ obeys a power law and is of the form f^β . The spectral exponent, β , governs the contribution of a scale to the variance. In experimental studies of cloud properties β is often found to be about $-5/3$ [Cahalan et al., 1989; Lovejoy et al., 1993].

We calculate the variance spectra from the time series and spatial distributions of LWP in order to compare the scaling properties. If we cannot find a similarity of the variance spectra, then the time series cannot be representative for the spatial distribution and therefore a comparison of cloud properties, as measured from the time series and from space, is not useful. Similarity of scaling properties is necessary, but not the only requirement for the comparison of data sets.

6.1.2.4. April 26: Stratocumulus field

On this day a frontal zone passed over the Netherlands in the North. The spatial distribution of reflected sunlight at $0.6\mu\text{m}$ at 7:44 UTC (about 7:30 LST at Delft) is shown in Figure 6.1, showing thick convective clouds in the North, a StratoCumulus field in the South and broken cloud fields in between. From lidar measurements, we know that the StratoCumulus field was first detected over Delft at 2:30 UTC and vanished at about 8:40 UTC. The mean cloud height is 1500m and the geometrical thickness is 200m. We selected an area (indicated by a box in Figure 6.1) to calculate the variance spectrum of AVHRR derived LWP values of the StratoCumulus field. The area consists of 128×128 pixels, which gives us 7 octaves or 2 decades. The variance spectrum is presented as the top solid line in Figure 6.2. In order to investigate possible scale invariance, we fitted a straight line to the curve, which is depicted with the dotted line. The fit was made by calculating the contribution to the variance per

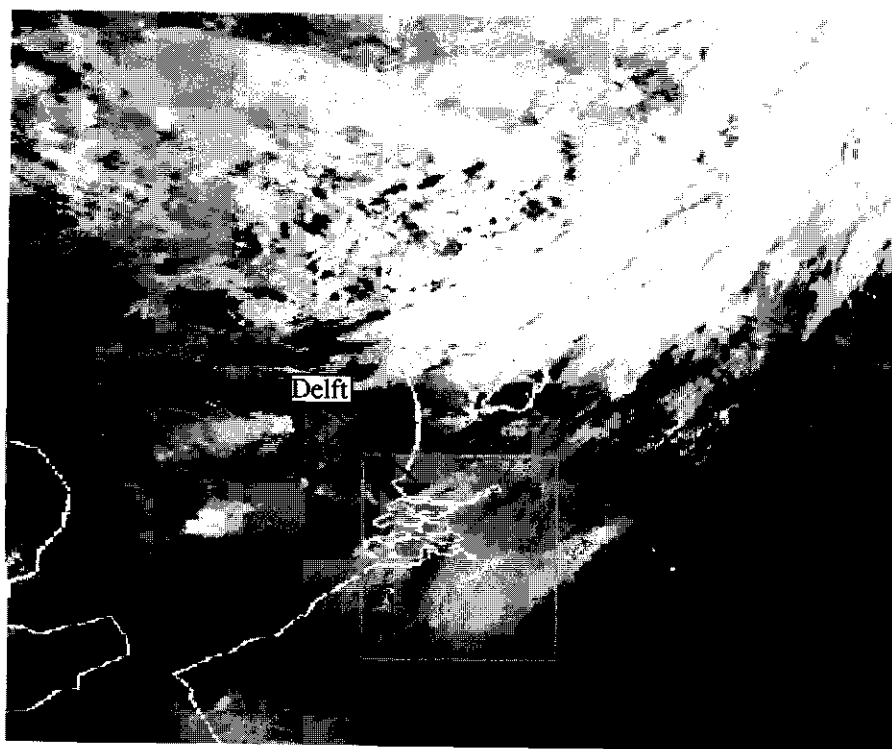


Figure 6.1: Spatial distribution of radiance at $0.6\mu\text{m}$ as measured from AVHRR image of the Netherlands on April 26 at 7:44 UTC. The location of the microwave radiometer at Delft is indicated.

octave with an assigned error based on the internal dispersion. The slope is -1.92 . The Goodness of fit (G) is 0.8 , an indication that the fit is convincing. According to Bevington [1969] a fit is evidently representative if G is larger than 0.1 . If G is below 0.001 , the fit is evidently not representative. We can conclude that the spatial distribution of the StratoCumulus field shows scale invariance with a spectral exponent of -1.92 . The variance spectrum of the whole image (not shown) is similar to that of the StratoCumulus field and shows scale invariance over 9 octaves.

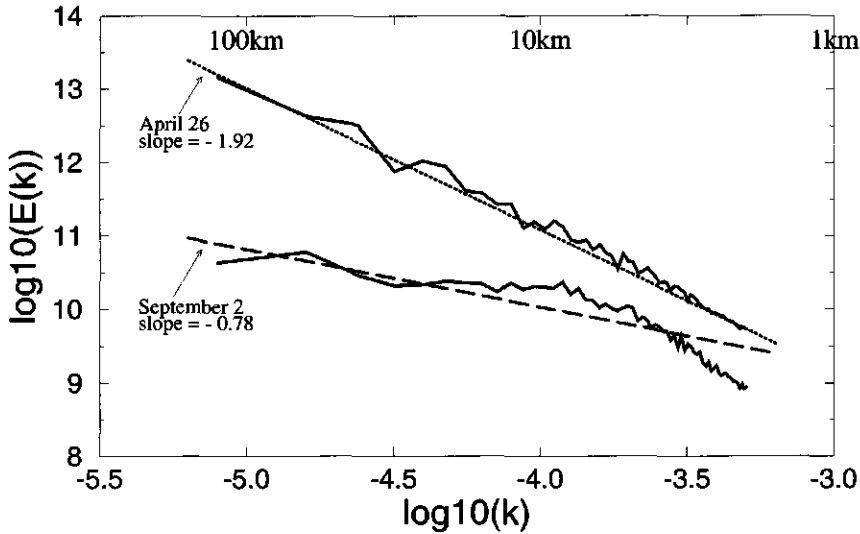


Figure 6.2: Variance spectra and the corresponding straight line fits calculated from the spatial distribution of LWP for the April 26 Stratocumulus field (upper lines) and the September 2 Cumulus field (lower lines).

In Figure 6.3 the time series of integrated liquid water column is shown. The values were sampled at a frequency of 1 Hz and show a large variability. The values range from 0 to 300 g/m^2 with an average of 38 g/m^2 . For the spectral analysis of the Stratocumulus field we use the measurements from $4:00$ until $8:45\text{ UTC}$, which consists of 16384 values. This gives us 14 octaves or 5 decades of scales. In Figure 6.4, the top solid line represents the corresponding variance spectrum. A straight line was fitted with a slope of -1.39 and G of 0.88 (grey solid line). We find that also the time series of LWP is clearly scale invariant. For the April 26 case, both the time series and the spatial distribution show scale invariance convincingly. The results are consistent with those of Lovejoy et al. [1993], Cahalan et al. [1989] and Davis et al. [1994, 1996].

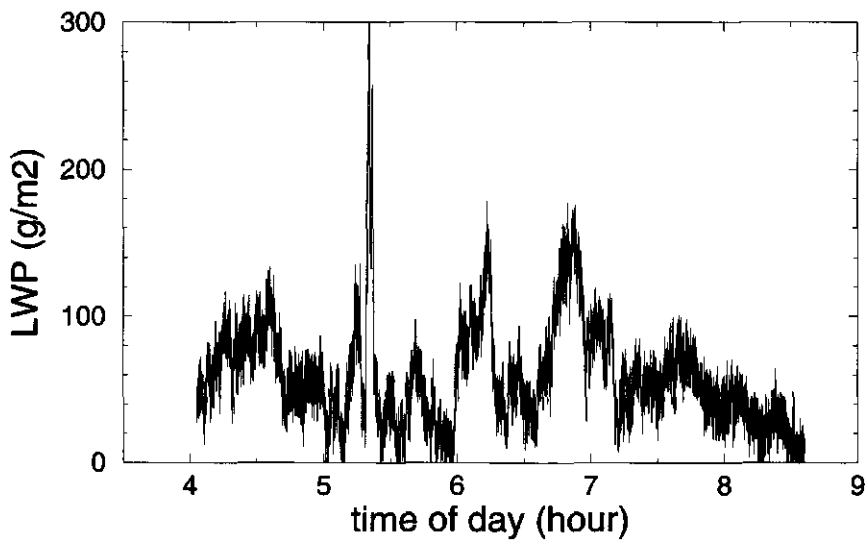


Figure 6.3: Time series of LWP as measured from ground based microwave radiometer on April 26.

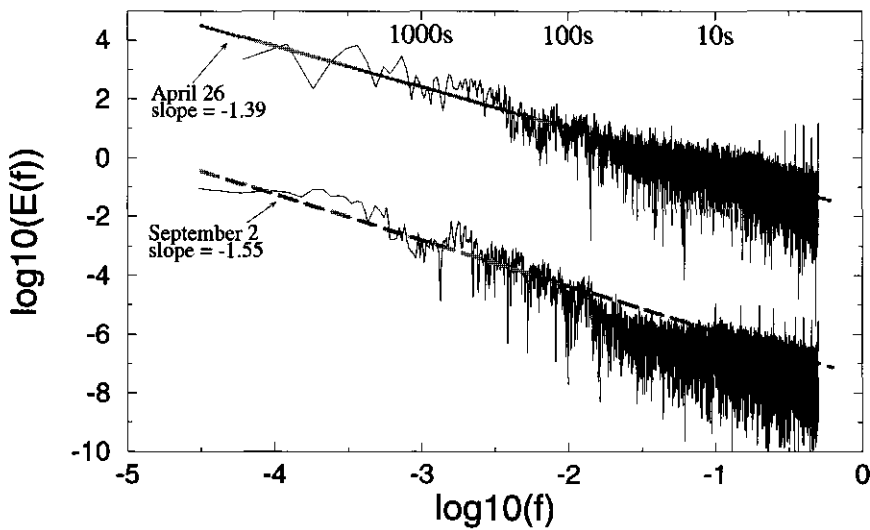


Figure 6.4: Variance spectra and the corresponding straight line fits calculated from the time series of LWP from the April 26 Stratocumulus field (upper lines) and the September 2 Cumulus field (lower lines).

6.1.2.5. September 2: Cumulus field

On this day there was a Cumulus cloud field over the Netherlands from 9 UTC until 16 UTC. Figure 6.5 shows the channel 1 image at 13:11 UTC (about 12:40 LST at Delft). Small cloud structures can be seen over Belgium in the South and large structures can be seen in the East over Germany. Over Delft, structures of intermediate size are present. Apart from the Cumulus field over land there is a StratoCumulus field over the North sea. From the lidar measurements we know that the cloud height ranged between 1000 and 1500m. Vertical profiles of the dewpoint and air temperature as measured from radiosonde, revealed the humid layer up to 1500m with very dry air above it. The wind direction at 1500m was Northeasteast.

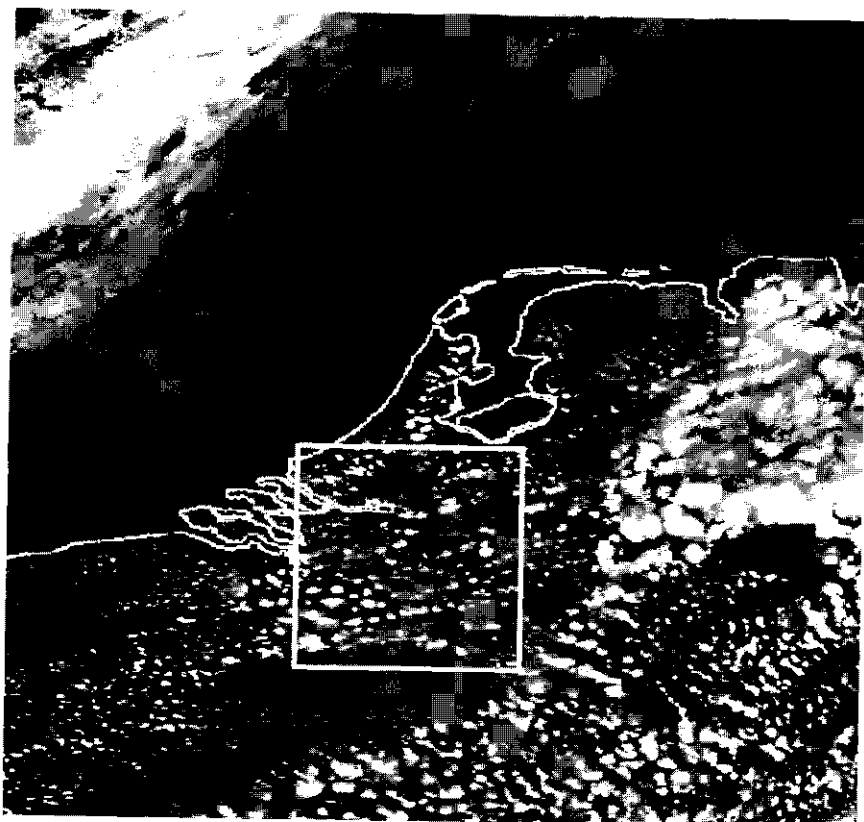


Figure 6.5: Spatial distribution of radiance at $0.6\mu\text{m}$ as measured from AVHRR image of the Netherlands on September 2 at 13:11 UTC.

The variance spectrum of the central part of the AVHRR image (indicated by a box in Figure 6.5) was calculated and is presented in Figure 6.2 as the lower solid curve. A straight line was fitted with a slope of -0.78 and G of $2 \cdot 10^{-13}$ (dashed line). The value of the G clearly indicates that the curve does not exhibit a straight line and thus we conclude there is no scale invariance over the whole range.

The time series of LWP is shown in Figure 6.6. The variability is very large. The LWP values range from 0 to 450 g/m^2 with an average of 15 g/m^2 . Note that at the time of satellite overpass (13:11 UTC) the LWP as measured from the ground is small. A direct comparison of values from the time series and spatial distribution therefore is not feasible. The variance spectrum derived from the LWP time series is shown in Figure 6.4 (lower solid curve) together with the values for the April 26 case (upper curve). A straight line was fitted with a slope of -1.55 and G of $5 \cdot 10^{-8}$ (dashed line). We conclude that also the time series clearly does not show scale invariance over the whole range. Inspection by eye seems to indicate that the variance spectrum of the September 2 Cumulus field meander around the straight line. Possibly there is a scale break or a scale of preference in this case, which we will investigate further.

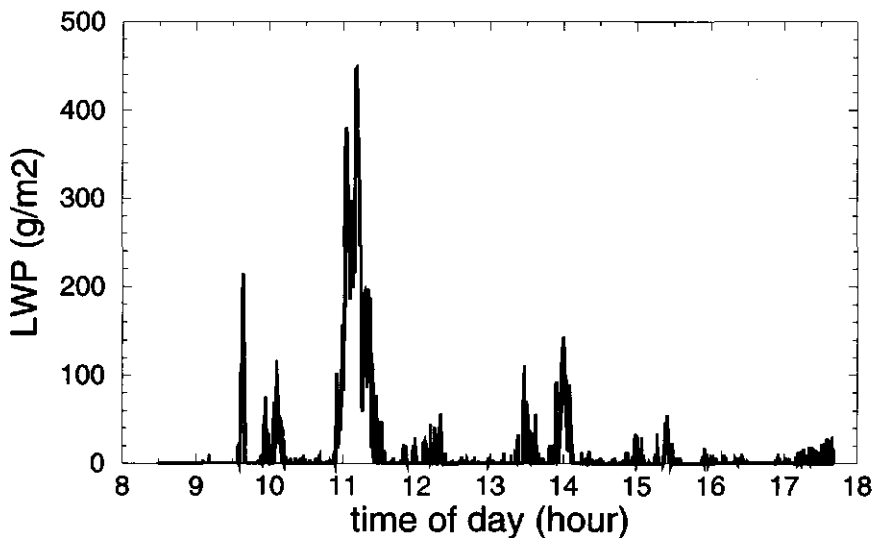


Figure 6.6: Time series of LWP as measured from ground based microwave radiometer on September 2nd.

The April 26 case shows scale invariance over the whole range for both the time series and the spatial distribution and thus both distributions have the same variability signature. Both

the spatial and the temporal LWP distributions from the September 2 case show deviations from a power law signature in a double logarithmic plot. However, from the analysis described above we cannot prove that both distributions have the same variability signature. In the following section another representation will be employed, which is more suitable for the analysis of scale breaks and scales of preference.

6.1.3. Linking temporal and spatial scale parameters

The presentation of variance spectra on double logarithmic axes, such as in Figure 6.2, is very useful in the case of scale invariant data sets, because the spectral exponent, β , can be obtained from the slope of the curve directly. The drawback, however, is that it may give a wrong impression about which scales are truly important for the variance. In many atmospheric disciplines it is therefore customary to present the spectra on log-linear axes [Stull, 1988]. On the y-axis one displays $f^*E(f)$, i.e. the spectral density multiplied by the frequency, in order to compensate for the logarithmic frequency axis, since $E(f)df = f^*E(f)d(\log f)$. The advantage of this presentation is that the area under the curve is proportional to the variance; a peak in a spectrum plotted in this way, can then correctly be interpreted as an important contribution to the variance.

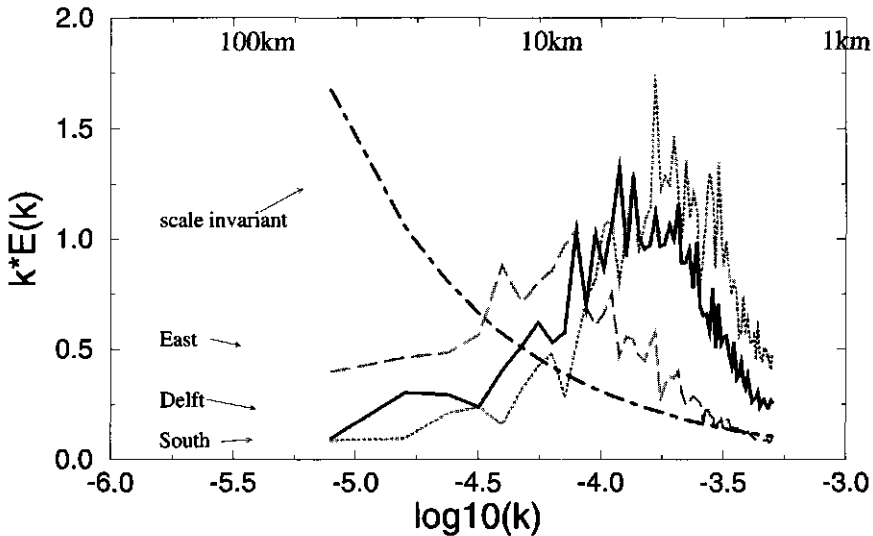


Figure 6.7: Variance spectrum calculated from the spatial distribution of LWP for September 2 from: the Southeast (dotted line), the Center (solid line) and the Northwest (dashed line). The dotted dashed line indicates a $-5/3$ power law.

In order to evaluate the sensitivity of our method to determine a scale of preference, we select three areas in the AVHRR image which, by eye, seem to differ: East over Germany (large structures), South over Belgium (small structures) and the Delft area, which is central in the image. In Figure 6.7, the contribution of the Fourier components to the variability is presented for scales from 2 to 64 pixel sizes for the three selected areas. In the prevailing viewing geometry the pixel size is about 1.2km. The dotted line represents the Southern part of the cloud field. The scale of preference (determined by smoothing the variance spectrum) is about 6.7km. The dashed line represents the Eastern part. The scale of preference is much larger: about 17.3km. The solid line represents the area near Delft. The scale of preference is about 8.9km. The dash-dot line indicates how a $k^{(-5/3)}$ dependence would look in this type of plot, showing an increase of the contribution to the variance with increasing scale. Clearly, for this Cumulus cloud field there is a scale of preference, which gradually increases from Southwest to Northeast. This result is consistent with the observation that, by eye, the structures in the Northeast indeed seem larger than in the Southwest.

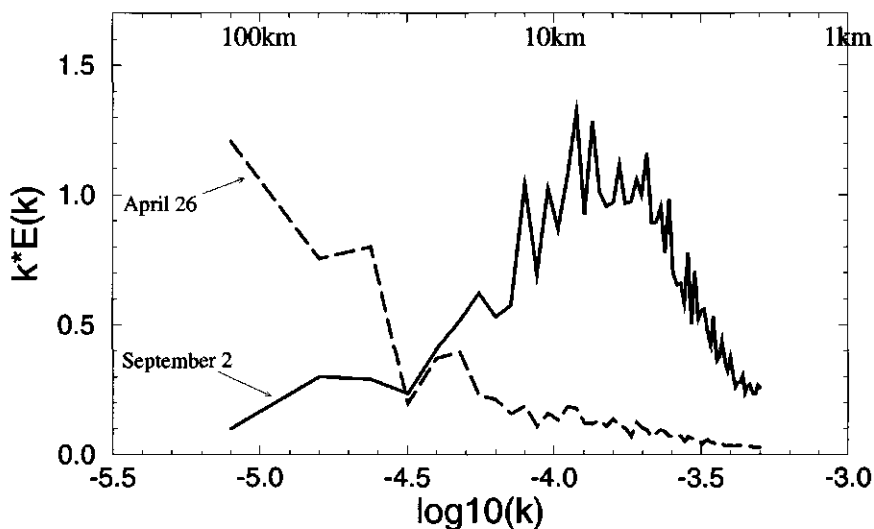


Figure 6.8: Variance spectrum calculated from the spatial distribution of LWP derived from AVHRR radiance for the September 2 Cumulus field over the Delft area (solid line) and the April 26 Stratocumulus field (dashed line).

The variance spectrum of the spatial distribution of LWP derived from the AVHRR imager for the Delft area for both April 26 and September 2 were shown in double logarithmic representation of Figure 6.2. In Figure 6.8 the same data set is shown in log-linear

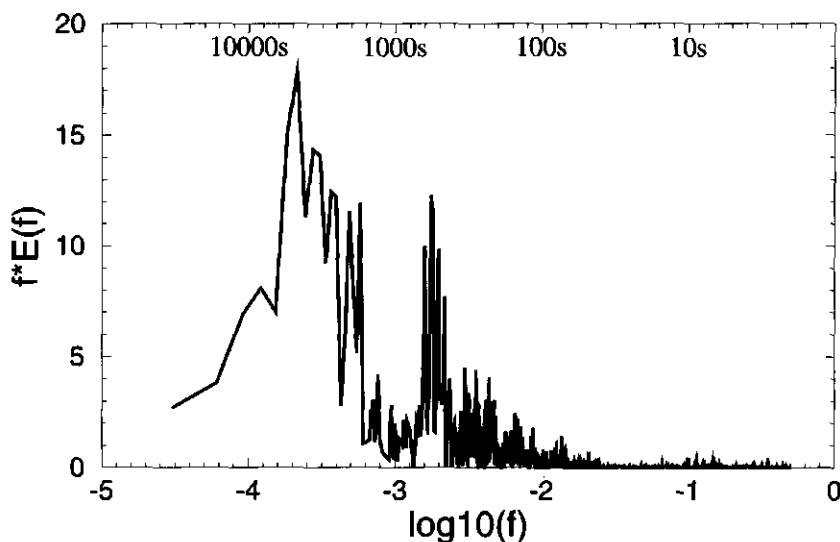


Figure 6.9: Variance spectrum calculated from the time series of LWP from September 2.

representation. The April 26 Stratocumulus field exhibits the signature of a scale invariant cloud field, which implies that the largest contribution to the variability stems from the largest scales. The September 2 Cumulus field exhibits a distinct peak at an intermediate scale in this representation. This comparison of representations clearly shows the strength of the double logarithmic representation to obtain the spectral exponent and the strength of the log-linear representation to identify a scale of preference.

The time series of LWP values was also analyzed to find scales of preference. In Figure 6.9 the contribution of Fourier components to the variability is presented for scales from 2 seconds to 4 hours. The LWP values are represented by the solid line. We identify two scales of preference: a narrow small peak at about 560s and a broad peak at about 4960s. Fair weather cumuli typically have a lifetime of the order of tens of minutes, so a preferred time scale of 560s is reasonable. The larger, 5000s, scale could be due to Mesoscale Cellular Convection [Agee et al., 1984]. The physical mechanism responsible for these large structures is still not well understood [Atkinson and Zhang, 1996].

Both the spatial analysis of a satellite image at one moment in time and the measurements of LWP values for one location continuous in time from 8:30 until 17:40 UTC show a scale of preference. We are interested in the possibility of relating the time series to the spatial distribution. Therefore we introduce a conversion factor u , which maps the variance spectrum of the temporal distribution on that of the spatial distribution with $k = f/u$. The best correlation between the variance spectra is obtained when u is 2m/s. In Figure 6.10 the time series is projected to a spatial distribution using the conversion factor. Not only the peak values coincide, but also the shape of the distributions is similar, which indicates that we do not just map the peak, but that for these scales the distributions probably stem from the same process. Furthermore, the 2m/s conversion factor maps the second scale of preference, 560s, to a spatial scale of about 1.1km. This is of the order of the boundary layer height (1500m), which is consistent with turbulence theory [Garratt, 1992; Stull, 1988]. From radiosonde launches at 6, 12 and 18UTC, we find that the wind speed at the cloud height of 1000 - 1500m, which is derived from lidar measurements, was about 2 - 3m/s throughout the day. This indicates that the conversion factor is of the same order as the wind speed at cloud height.

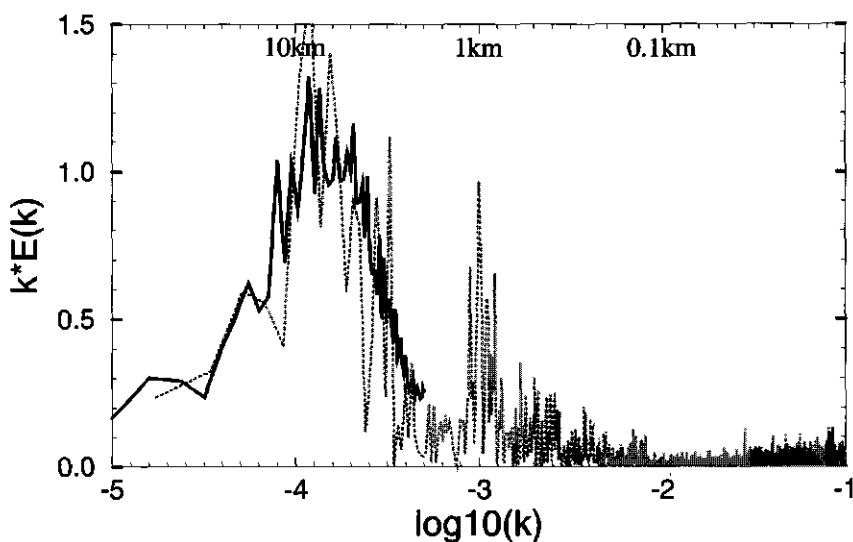


Figure 6.10: Variance spectrum calculated from the spatial distribution (solid line) and the variance spectrum calculated from the time series mapped to the spatial domain using a conversion factor $u = 2\text{m/s}$ (dotted line).

In this section we showed that the variance spectra of the time series and the variance spectra of the spatial distribution are similar statistically and the scales of preference are consistent. Therefore a statistical comparison of the signal is feasible. The time series has been projected to a spatial distribution using a conversion factor of 2m/s. In the following section possible applications are discussed.

6.1.4 Discussion

It would seem from the above that for the time scales under study the Taylor's hypothesis of an advected frozen atmosphere holds, because the multiplication of dominant time scale and wind speed yields the dominant spatial scale. If Taylor's hypothesis would hold for LWP values, we could advect the measured LWP from the time series using the prevailing wind speed and calculate the probable location of 'the advected clouds' at the time of the satellite overpass thus enabling direct comparison of values. However, the cumuli are formed through convection, which acts at the same time and space scales as the wind speed. Within the 500s that it takes to advect a 1km cloud over the microwave radiometer the cloud will have lived a full lifecycle from condensation to evaporation. This variability is fundamental to cloud processes and therefore, the concept of an advected frozen atmosphere is not valid at the scales considered here. This argument disables a direct comparison of the time series of LWP with the same cloud parameter derived from AVHRR.

However, the statistical link between the scaling properties in time and space does allow us to use high resolution time series to study the variability of the spatial distribution of cloud properties at a very high resolution. The conversion factor of 2m/s implies that the time series measurements at 1Hz may be used to study spatial variability at 2m scale. Technically it is possible to create a synthetic spatial distribution which has the same scaling properties as the time series. Such a distribution may be very helpful in the interpretation of spatial distributions of LWP values at the sub-scale of the instantaneous field of view (IFOV) of a satellite instrument, for example the AMSU or SSM/I.

There are a number of limitations to this approach. The integration area of the microwave radiometer is about 35m at 1000m height. In the 18 seconds that the cloud is over the instrument, the variability of the signal will be due to both advection and development [Stull, 1988]. Therefore, in this case we should not interpret the values below 18s. Furthermore, the

synthetic spatial distribution of LWP at 2m resolution cannot be used to create a synthetic AVHRR 0.6 μ m image of reflected sunlight at 2m resolution, due to multiple scattering of the incident sunlight. Photons may travel considerable horizontal distances and thereby violate the independent pixel approximation, which is required to make the synthetic spatial distribution [Marshak et al., 1998; Savigny et al., 1999].

6.1.5 Conclusions

A study was presented into the correlation between scaling properties of a time-series of LWP measured at one point in space, but continuous in time and a spatial distribution of LWP values at one moment in time as derived from measurements of reflected sunlight in the 0.6 μ m channel of the AVHRR. It was shown that the scaling properties of the time series and spatial distribution are similar both for a Stratocumulus field, which shows scale invariance, and for a Cumulus field for which scales of preference were identified. We show that a double logarithmic representation is most suitable to obtain the spectral exponent, while a log-linear representation is more appropriate to identify a scale of preference.

For the Cumulus field it was possible to map the variance spectrum of the time series onto that of the spatial distribution with a conversion factor of 2m/s. The conversion factor is a statistical link between time and spatial scales. This does not imply that we can directly compare LWP values in the time series and spatial distribution. However, the statistical link of the scaling properties in time and space allows us to use high resolution time series to study the variability of the spatial distribution of cloud properties at a very high resolution.

Acknowledgements

We thank the reviewers for their efforts. Their comments have significantly contributed to the paper. We thank Dr. Rose D'hopolsky, Dr. Dave Donovan, Dr. Peter Duynkerke and Dr. Aad van Ulden for valuable comments on earlier versions of this paper. We thank Dr. Marshak for his contribution in understanding the Stratocumulus case. We thank Suzanne Jongen from the Technical University Eindhoven for providing the valuable microwave radiometer measurements.

References

- Agee, E.M., Observations from space and thermal convection, A historical perspective, *Bull. Amer. Meteor. Soc.*, 63, 938-946, 1984.
- Atkinson, B.W. and J.W. Zangh, Mesoscale shallow convection in the atmosphere, *Rev. Of Geophysics*, 34, 403-431, 1996.
- Bevington, P.R., *Data reduction and Error Analysis for Physical Sciences*, McGraw-Hill, New York, 1969.
- Cahalan, R.F. and J.H. Snider, Marine StratoCumulus structure, *Remote Sens. Environ.*, 28, 95-107, 1989.
- Cahalan, R.F., W. Ridgeway, W.J. Wiscombe, S. Gollmer, and Harshvardhan, Independent pixel and Monte Carlo estimates of StratoCumulus albedo. *J. Atmos. Sci.*, 51, 3776-3790, 1994.
- Davis, A., A. Marshak, W. Wiscombe, and R. Cahalan: Multifractal characterizations of non-stationarity and intermittency in geophysical fields: observed, retrieved or simulated, *J. Geophys. Res.*, 99, 8055-8072, 1994.
- Davis, A., A. Marshak, W. Wiscombe, and R. Cahalan: Scale invariance of liquid water distributions in StratoCumulus. Part I: Spectral properties and stationarity issues, *J. Atmos. Sci.*, 53, 1538-1558, 1996.
- Deirmendjian, D., *Electromagnetic scattering on spherical polydispersions*, American Elsevier, New York, 1969.
- Feijt, A., H. ten Brink, S. Jongen, and A. van Lammeren, Validation of satellite cloud parameter retrieval methods with objective ground based measurements, *Phys. and Chem. of the Earth*, 24, 173-176, 1999.
- Garratt, J.R., *The Atmospheric Boundary Layer*. Cambridge University Press, 316 pp., 1992.
- Koelemeijer, R. P. Stammes, and A. Feijt, Cloud optical thickness retrieval from AVHRR data, paper presented at symposium on satellite remote sensing, SPIE, 2582, 284-293, 1995
- Lammeren, A.C.A.P. van, H.W.J. Russchenberg, A. Apituley, H. ten Brink, and A.J. Feijt, CLARA: a data set to study sensor synergy, paper presented at the Workshop on Synergy of Active Instruments of the Earth Radiation Mission, GKSS Research Center, Geesthacht, Germany, November 12-14, 1998
- Lovejoy, S., D. Schertzer, P. Silas, Y. Tessier, and D. Lavalée, The unified scaling model of atmospheric dynamics and systematic analysis of scale invariance in cloud radiances. *Ann. Geophys.*, 11, 119-127, 1993.

- McClatchey, R. et al., Optical properties of the atmosphere, 3-rd ed., AFCRL-72-0497, 107pp., Air Force Cambridge Research Labs., 1972.
- Marshak A., A. Davis, W. Wiscombe, and R. Cahalan, Radiative effects of sub-mean free path liquid water variability observed in stratiform clouds. J. Geophys. Res., 103, D16, 19,557-19,567, 1998.
- Saunders, R.W., An automated scheme for the removal of cloud contamination from AVHRR radiances over western Europe, Int. J. Remote Sens., 7, 867-886, 1986.
- Saunders, R.W., and K.T. Kriebel, An improved method for detecting clear sky and cloudy radiances from AVHRR data, Int. J. Remote Sens., 9, 123-150, 1988.
- Savigny, C. von, O. Funk, U. Platt and K. Pfeilsticker, Radiative smoothing in zenith-scattered skylight transmitted through optically thick clouds to the ground, Geophys. Res. Lett., 26, 2949-2952, 1999.
- Stull, R.B., An introduction to Boundary Layer Meteorology, 666 pp., Kluwer, 1988

7. Conclusions and perspective

The aim of this thesis, as described in section 1.4, includes the development and validation of cloud analysis methods for AVHRR and Meteosat and the use of these methods for detailed cloud studies.

The Meteosat cloud analysis method, Metclock, was developed and validated with synoptic observations. The use of surface temperature information from a numerical weather prediction model was found to largely improve the skill of the cloud detection tests. An AVHRR cloud analysis method, KLAROS, was developed.

A number of distinctly different cloud cases were studied using meteorological satellites and ground based remote sensing instruments. Comparisons of results show that the KLAROS analysis yields good results both for LWP in a stratocumulus case and for cloud top temperature in a cirrus case. Furthermore, it was shown that combining ground based and satellite measurements is required to get a full description of the cloud field.

The temporal and spatial variability of cloud LWP was studied in terms of scaling parameters. It was found that the scaling parameters as derived from a time series and from a spatial distribution could be linked, both for a case with scale invariance and for a case with a distinct scale of preference. In conclusion, we may state that the aims of the thesis are met.

In the following it is described how the methods which were developed in the course of this study are currently being used, both in operational meteorology and in climate research. This chapter is concluded with an outlook on future use of these methods for new space based instruments.

The TEBEX measurements from 1995 and 1996, which also includes the measurements from 10 stations for ground based remote sensing, are currently being used as to evaluate atmospheric model output (Van Lammeren et al., 2000; Van Meijgaard et al, 2000). The past few years, the Meteosat analysis environment has been employed to initialize an operational short-term cloud prediction model (Van der Veen and Feijt, 1996). The impact of this approach to the skill of the operational Numerical Weather Prediction model, HIRLAM is currently being assessed. Algorithms are developed to combine the Meteosat analysis results

with ground based lidar and infrared radiometer measurements to obtain operational automated cloud observation.

The results of the retrieval methods are satisfactory, however, still further improvements are envisaged. KLAROS is currently being expanded to include the use of the $1.6\mu\text{m}$ channel on board of NOAA-15, which was launched in May 1998. This enables an estimate of the particle size and phase of the top layer of the cloud. This also improves the estimate of LWP (Han et al., 1994; Nakajima and King, 1990). The improved LWP retrieval will be used to obtain LWP fields for the international Cloud Liquid Water Network Project (CLIWA-NET), which is co-funded by the European Union. For that purpose the derived LWP values will be combined with time series of LWP as measured from ground based microwave radiometers. The study, which was described in chapter 6, will be the basis to link the ground based and satellite data. The resulting LWP fields will be used to evaluate atmospheric model results. CLIWA-NET also includes an intensive validation campaign, similar to CLARA, but with a much larger scope of instruments. This campaign will take place in August/September 2001 and will enable detailed evaluation of the satellite retrieval methods.

An important follow-up of the research presented in this thesis, will be the analysis of measurements from the Spinning Enhanced Visible and Infrared Imager, SEVIRI, which will be on board of Meteosat Second Generation (MSG). This new geo-stationary instrument includes 11 spectral channels (see Table 7.1), of which 8 are similar to current AVHRR and Meteosat channels (Woick et al, 1997).

Each 15 minutes a new set of images will be available with a resolution of $3\times 3\text{km}^2$ at the equator. The 11 spectral channels can be used to obtain a full scope of cloud and surface parameters. The cloud field properties will include: fraction, thermodynamic phase, optical thickness, emissivity, top temperature, liquid water path and the spatial variability of these parameters. The 11 spectral channels and stable viewing geometry will enable the retrieval of surface parameters, which currently are derived from Meteosat and AVHRR, however, the quality will be much higher. These parameters will include: albedo, vegetation index, temperature, moisture content and heat fluxes. This is expected to have a major impact on the meteorological practise and climate research.

Number	Wavelength	Satellite
1	0.6	AVHRR
2	0.8	AVHRR
3	1.6	AVHRR
4	3.9	AVHRR
5	6.2	Meteosat
6	7.3	Meteosat
7	8.7	-
8	9.7	HIRS
9	10.8	AVHRR
10	12.0	AVHRR
11	13.4	HIRS

Table 7.1: Severi channels

This research contributes to quantitative use of meteorological satellite data in meteorology and climate research, which will be further developed as new instruments are launched in the next few years.

References

- Han, Q., W. B. Rossow and A. A. Lacis, 1994: Near-global survey of effective droplet radii in liquid water clouds using ISCCP data. *J. of Clim.*, 7, 465 – 497.
- Lammeren A. van, A. Feijt, J. Konings and E. van Meijgaard, 2000: Combination of ground Based and satellite cloud observations on a routine basis. *Contr. Atmos. Phys.* (in press).
- Meijgaard E. van, J. Konings, A. Feijt and A. van Lammeren, 2000: Comparison of model predicted cloud cover profiles with observations from ground and satellite. *Contr. Atmos. Phys.* (in press).
- Nakajima, T. and M.D. King, 1990: Determination of the optical thickness and effective particle radius of clouds from reflected solar radiation measurements: I Theory. *J. Atmos. Sci.*, 47 (15), 1878-1893.

- Veen S. van der, and A. Feijt: Liquid water initialization in a cloud prediction model using Meteosat imagery. Proc. of the 1996 EUMETSAT Meteorological Satellite DataUsers'Conference, EUMETSAT, Darmstadt, 257-264.
- Woick H., J. Schmetz and S. Tjemkes: An introduction to Meteosat Second Generation imagery and products. Proc. of the 1997 EUMETSAT Meteorological Satellite Data Users'Conference, Brussels, EUMETSAT, Darmstadt, 395-400.

Bibliography

- Ackerman S.A., S. K. Cox, 1981, Comparison of satellite and all-sky camera estimates of cloud cover during GATE. *J. Appl. Met.*, 20, 581- 587.
- Agee, E.M., Observations from space and thermal convection, A historical perspective, *Bull. Amer. Meteor. Soc.*, 63, 938-946, 1984.
- Atkinson, B.W. and J.W. Zangh, Mesoscale shallow convection in the atmosphere, *Rev. Of Geophysics*, 34, 403-431, 1996.
- Auer, A.H. and D.L. Veal, 1970: The dimensions of ice crystals in natural clouds. *J. Atmos. Sci.*, 27, 919-926.
- Barkstrom B.R. and G.L. Smith, 1986: The Earth Radiation Budget Experiment: Science and implementation. *Rev. Geophys.* 24, 379-390.
- Barnes J. C. and D. Chang, 1968, Accurate cloud cover determinations and its effect on albedo computations . Final report, Contract No. NA55-10478, Aracon Inc., Concord, Mass., 82 pp.
- Barrett E. C. and C. K. Grant, 1979, Relations between frequency distribution of cloud over the UK based on conventional observations and imagery from Landsat 2, *Weather*, 34, 416-424.
- Bevington, P.R., *Data reduction and Error Analysis for Physical Sciences*, McGraw-Hill, New York, 1969.
- Bishop J.K.B., W.B. Rossow and E.G. Dutton, 1997: Surface solar irradiance from the International Satellite Cloud Climatology Project 1983-1991. *J.G.R.*, 102 (D2), 6883-6910.
- Bloemink, H.I., A.C.A.P. van Lammeren, A.J. Feijt and S. Jongen, 1999. Active-passive sensor synergy for cloud observation; IR cloud properties and cloud liquid water. *J.Geophys.Res.* (submitted).
- Boers, R., A. van Lammeren and A. Feijt, 2000: Accuracy of cloud optical depth retrievals from ground based pyranometers. *Atmos. and Ocean. Techn.* (accepted).
- Bordes, P., P. Brunel and A. Marsouin, 1992: Automatic adjustment of AVHRR navigation. *J. Atmos. Ocean. Techn.*, 9, 15-27.
- Bowker, D.E., R.E. Davis, D.L. Myrick, K. Stacy and W.T. Jones: Spectral reflectances of natural targets for use in remote sensing studies. NASA Rep. 1139, p181.
- Bunskoek D.A., A.C.A.P. van Lammeren and A.J. Feijt, 1998: Temperature corrections on radiation measurements using Modtran 3. KNMI Techn. Rep.-204, KNMI, De Bilt.

- Cahalan, R.F., W. Ridgeway, W.J. Wiscombe, S. Gollmer and Harshvardhan, 1994: Independent pixel and Monte Carlo estimates of Stratocumulus albedo. *J. Atmos. Sci.*, 51, 3776-3790.
- Cahalan, R.F. and J.H. Snider, 1989: Marine StratoCumulus structure. *Remote Sens. Environ.* 28, 95- 107.
- Cess, R.D. et al., 1996: Cloud feedback in atmospheric general circulation models: An update. *J. Geophys. Res.*, 101D, 12791-12794.
- Cess, R.D. et al., 1990: Intercomparison and interpretation of climate feedback processes in 19 general circulation models. *J. Geophys. Res.*, 95, 16601-16615.
- Cess, R.D. et al., 1989: Interpretation of cloud-climate feedback as produced by 14 atmospheric general circulation models. *Science*, 245, 513-516.
- Che, N and J.C. Price, 1992: Survey of radiometric calibration results and methods for visible and near infrared channels of NOAA-7, -9 and 11 AVHRR's, *Rem. Sens. Environ.*, 41, 19-27.
- Cheruy, F., and R. S. Kandel, 1991: Use of Meteosat data for validation of the diurnal variation of the outgoing longwave radiation produced by ERBE. *Dyn. Atmos. Oceans*, 16, 73-84.
- Coakley J.A. and F.P. Bretherton, 1982: Cloud cover from high-resolution scanner data: Detecting and allowing for partially filled fields of view. *J. Geophys. Res.*, 87, 4917-4932.
- Coley, P.F. and P.R. Jonas, 1996: The influence of cloud structure and droplet concentration on the reflectance of shortwave radiation. *Ann. Geophys.*, 14(8), 845-852.
- Davies, R., 1978: Effect of finite geometry on the three-dimensional transfer of solar irradiance in clouds. *J.A.S.*, 9, 1712-1725.
- Davis, A., A. Marshak, W. Wiscombe, and R. Cahalan: Multifractal characterizations of non-stationarity and intermittency in geophysical fields: observed, retrieved or simulated, *J. Geophys. Res.*, 99, 8055-8072, 1994.
- Davis, A., A. Marshak, W. Wiscombe, and R. Cahalan: Scale invariance of liquid water distributions in StratoCumulus. Part I: Spectral properties and stationarity issues, *J. Atmos. Sci.*, 53, 1538-1558, 1996.
- Deirmendijan, D., 1969: Electromagnetic scattering on spherical polydispersions. American Elsevier, New York.

- Derrien M., B. Farki, L. Harang, H. Legleau, A. Noyalet, D. Pochic and A. Sairouni, 1993: Automatic cloud detection applied to NOAA-11/AVHRR imagery. *Rem. Sens. Environ.* 46, 246-267.
- Desbois M, G. Seze and G. Szejwach, 1982: Automatic classification of clouds on METEOSAT imagery: Application to high-level clouds. *J. Appl. Meteor.*, 21, 401-412.
- Descloîtres, J. F. Parol and J. Buriez, 1995: On the validity of the plane-parallel approximation for cloud reflectances as measured from POLDER during ASTEX. *Ann. Geophys.*, 13, 108-110.
- Desormeaux, Y., W. Rossow, C. Brest and G. Campbell, 1993: Normalization and calibration of geostationary satellite radiances for the International Satellite Cloud Climatology Project. *J. Atmos. and Ocean. Techn.*, 10, 304-325.
- Diekmann F.J. and J de Waard; 1992, New concepts of Meteosat image data resampling. *Proc. of the EUMETSAT Meteorological Satellite Data Users' Conference, Locarno, Eumetsat*, 401-407.
- EUMETSAT; 1997, MSG ground segment: Meteorological products extraction facility algorithm specification document. *Eumetsat Doc. No. EUM/MSG/SPE/022.*, EUMETSAT, Darmstadt.
- Feigelson, E.V. (editor), 1984: *Radiation in a cloudy atmosphere*, Reidel etc., Dordrecht
- Feijt, A. and H. Jonker, 2000: Comparison of scaling parameters from spatial and temporal distributions of cloud properties. *J. Geophys. Res.* (in press)
- Feijt A. and P. de Valk, 2000: The use of NWP data in cloud detection from Meteosat imagery. *Int. J. Rem. Sens.* (accepted).
- Feijt A., H. ten Brink, S. Jongen, A. van Lammeren and H. Russchenberg, 1999: Validation of cloud parameter retrieval methods with objective ground based measurements. *Phys. Chem. Earth*, 24, 173-176.
- Feijt A. and P. de Valk, 1998: Quantifying the difference between NWP surface temperatures And cloud free satellite apparent brightness temperatures. *Contrib. Atmos. Phys.*, 71, 455-460.
- Feijt A. and A. van Lammeren, 1996: Ground-based and satellite observations of cloud fields in the Netherlands. *Monthly Weather Review*, 124, 1914-1923.
- Feijt, A.J., 1992: The Earth Radiation Budget Experiment: Overview of data-processing and error sources. *KNMI TR-162, KNMI, De Bilt*, 36pp.

- Frohlich, C. and J. Lean, 1998: The Sun's total irradiance: Cycles, Trends, Related Climate Change Uncertainties since 1976. *Geophys. Res. Lett.*, 25, 4371-4380.
- Garratt, J.R., *The Atmospheric Boundary Layer*. Cambridge University Press, 316 pp., 1992.
- Gates, W.L. et al., 1999: An overview of the results of the atmospheric model intercomparison project (AMIP I), *Bull. Amer. Meteor. Soc.*, 80, 29-55.
- Gesell G., T. Konig, H. Mannstein, and K. T. Kriebel, 1993: SHARK-APOLLO quantitative satellite data analysis based on ESRIN/SHARP and DLR/APOLLO. *Proc. of the Sixth AVHRR European Data Users' Meeting*, Belgirate, Italy, Eumetsat, 583-587.
- Gesell. G, 1989: An algorithm for snow and ice detection using AVHRR data: An extension to the APOLLO software package, *Int. J. Rem. Sens.*, 10, 897-905.
- Gtopo30, 1998: Gtopo30: Description of world topography data set. On Internet:
- Gustafsson N., 1993: HIRLAM 2 Final Report. SMHI Technical Report 9., 129pp.
- Haan, J.F. de, P.B. Bosma and J.W. Hovenier, 1987: The adding method for multiple scattering calculations of polarized light. *Astron. Astrophys.*, 183, 371-391.
- Han, Q., W. B. Rossow and A. A. Lacis, 1994: Near-global survey of effective droplet radii in liquid water clouds using ISCCP data. *J. of Clim.*, 7, 465 - 497.
- Harrison, E.F., P. Minnis, B.R. Barkstrom, V. Ramanathan, R.D. Cess and G. Gibson, 1990: Seasonal variation of cloud radiative forcing derived from the Earth Radiation Budget Experiment. *J. Geophys. Res.*, 95, 18687-18703.
- Henderson-Sellers A. and K. McGuffey, 1991: An investigation of the burger distribution to characterize cloudiness. *J. of Clim.*, 4, 1181-1209.
- Hess, M., R.B.A. Koelemeijer and P. Stammes, 1998: Scattering matrices of imperfect hexagonal ice crystals. *J. Quant. Spectrosc. Radiat. Transfer*, 60, 301-308.
- Hess, M., P. Stammes and R. Koelemeijer, 1997: Scattering matrices of ice crystals. KNMI Scientific Rep. 97-07, KNMI, Bilthoven
- Hess, M. and M. Wiegner, 1994: COP: A data library of optical properties of hexagonal ice crystals. *Appl. Opt.*, 33, 7740-7746.
- Heymsfield, A.J. and C.M.R. Platt, 1984: A parametrization of the particle size spectrum of ice clouds in terms of the ambient temperature and the ice water content, *J. Atm. Sci.*, 41, 846-855.
- Hulst van der, 1963: A new look at multiple scattering, *Tech. Rep.*, Institute of Space Studies NASA, New York.
- Intergovernmental Panel on Climate Change, 1995: IPCC Second Assessment Report Climate Change, UNCEP/WMO.

- Jolivet, D., 1999: Etude de l'influence de l'heterogeneite des nuages sur le champ de rayonnement solaire reflechi vers l'espace. Univ. of Lille, France.
- Jonas P., 1991: Cloud cover distributions and correlations. *J. Appl. Met.*, 31, 732-741.
- Karlsson, K-G.; 1996: Cloud classification with the SCANDIA model. SMHI report RMK 67., SMHI, Norrkoping.
- Karlsson K-G., 1993: Comparison of operational AVHRR-based cloud analysis with surface observations. *Proc. 6th AVHRR data users'meeting, EUMETSAT, Darmstadt*, 223-229.
- Kastner, M., K. T. Kriebel, and H. P. Schickel, 1993: Alpine cloud climatology--First results. *Proc. Sixth AVHRR European Data Users' Meeting, Belgirate, Italy, Eumetsat*, 253-257m
- Klein, S.A. and D.L. Hartmann, 1993: Spurious changes in the ISCCP data set. *Geophys. Res. Letters*, 20, 455-458.
- Knap, W.H., M. Hess, P. Stammes, R.B.A. Koelemeijer and P.D. Watts, 1999: Cirrus optical thickness and crystal size retrieval from ATSR-2 data using phase functions of imperfect hexagonal ice crystals. *J. Geophys. Res.*, 104 (D24), 31, 721-31,730.
- Kneizys, F. X., E. P. Shettle, W. O. Gallery, J. H. Chetwynd, L. W. Abreu, J. E. A. Selby, S. A. Clough, and R. W. Fenn, 1988: Users guide to Lowtran-7. Air Force Geophysics Laboratory AFGL-TR-88-0177, 200 pp.
- Koelemeijer R. B. A., P. Stammes and A. Feijt, 1995: Cloud optical thickness retrieval from AVHRR-data. *Proc. Symposium on Atmospheric Sensing and Modelling II, SPIE vol. 2582*, 284-293.
- Koelemeijer, R., A. Feijt, A. Hulshof and A. van Lammeren, 1995: Cloud properties from the KNMI cloud detection system compared with LITE observations. *Proc. of the 1995 EUMETSAT Meteorological Satellite Data Users'Conference, EUMETSAT, Darmstadt*
- Koelemeijer, R.B.A., 1995: Calibration of AVHRR channels 1 and 2, KNMI Memo number AO-95-02, De Bilt.
- Koelemeijer, R.B.A., 1994: Nadir reflectivity of a stratocumulus cloud deck at 630nm: a sensitivity study. KNMI report: AO-94-08.
- Koepke, P., 1982: Vicarious calibration of the Meteosat visible channel. *Appl. Opt.*, 21(15), 2845-2854.
- Koepke P. and K.T. Kriebel, 1978: Influence of measured reflection properties of vegetated surfaces on atmospheric radiance and its polarization. *Appl. Optics*, 2, 260-264.

- Kriebel, K.T. and V. Amann, 1993: Vicarious calibration of the Meteosat visible channel. *J. Atmos. and Ocean. Techn.*, 10(2), 225-232.
- Kriebel, K.T., R.W. Saunders and G. Gesell, 1989: Optical properties of clouds derived from fully cloudy AVHRR pixels. *Contrib. Atmos. Phys.*, 62, 165-171.
- Kriebel K.T., 1978: Measured spectral bidirectional reflection properties of four vegetated surfaces. *Appl. Optics*, 2, 253-259.
- Labeled J. and M.P. Stoll, 1991: Spatial variability of land surface emissivity in the thermal Infrared band: spectral signature and effective surface temperature. *Rem. Sens. Environ.*, 38, 1-17.
- Lacis, A.A. and J.E. Hansen, 1974: A parametrization of the absorption of solar radiation in the earth's atmosphere. *J. Atmos. Sci.*, 31, 118-133.
- Lammeren A. van, A. Feijt, J. Konings and E. van Meijgaard, 2000a: Combination of ground Based and satellite cloud observations on a routine basis. *Contr. Atmos. Phys.* (in press).
- Lammeren, A. van , H. Russchenberg, A. Apituley, H. ten Brink and A. Feijt, 1998: CLARA a data set to study sensor synergy. *Proc. 'Synergy of Active instruments of the Earth Radiation Mission'*, nov. 12-14, GKSS, Geesthacht, Germany.
- Lammeren A.C.A.P. van, and A.J. Feijt, 1997: Cloud research in the Netherlands: CLARA, *Change*, 34, NRP, Bilthoven, 10-13.
- Lammeren, A. van and A. Feijt, 1997: Cloud research in the Netherlands: CLARA. *Change*, 34, NRP, Bilthoven, 10-13.
- Lammeren, A.C.A.P. van and A.J. Feijt, 1997: The emissivity of Cirrus clouds derived from LITE and Meteosat measurements. *Selected Papers of the 18th International Laser Radar Conference (ILRC)*, Berlin 22-26 July 1996, published by Springer Verlag New York Berlin-Heidelberg (ISDN 3-540-61887-2) pp. 201-204.
- Lovejoy, S., D. Schertzer, P. Silas, Y. Tessier, and D. Lavalée, 1993: The unified scaling model of atmospheric dynamics and systematic analysis of scale invariance in cloud radiances. *Ann. Geophys.*, 11, 119-127.
- Lovejoy, S., and D. Schertzer, 1990: Multifractals, universality classes and satellite and radar measurements of cloud and rain fields, *J. Geophys. Res.*, 95, 2021-2034.
- Macke, A., 1994: Modellierung der optische Eigenschaften von Cirruswolken, Ph. D. Thesis, 98pp. Univ. Of Hamburg, Germany
- Macke, A., J. Muller and E. Raschke, 1996: Single scattering properties of atmospheric ice crystals. *J. Atmos. Sci.*, 53, 2813-2825.

- Marshak A., A. Davis, W. Wiscombe and R. Cahalan, Radiative effects of sub-mean free path liquid water variability observed in stratiform clouds. *J. Geophys. Res.*, 103, D16, 19,557-19,567, 1998.
- McClatchey, R. et al., 1972: Optical properties of the atmosphere, 3-rd ed., AFCRL-72-0497, Air Force Cambridge Research Labs., 107pp.
- Meijgaard E. van, J. Konings, A. Feijt and A. van Lammeren, 2000: Comparison of model predicted cloud cover profiles with observations from ground and satellite. *Contr. Atmos. Phys.* (in press).
- Minnis, P., D. Graber, D. Young, R. Arduini and Y. Takano, 1998: Parametrizations of reflectance and effective emittance for satellite remote sensing of cloud properties. *J. Atmos. Sci.*, 55(22), 3313-3339.
- Minnis P., W.L. Smith Jr., D. P. Garber, J.K. Ayers and D.R. Doelling, 1995: Cloud properties derived from GOES-7 for the spring 1994 ARM intensive observing period using version 1.0.0 of the ARM satellite data analysis program. NASA RP 1366, pp 59.
- Minnis P., K-N Liou and Y Takano, 1993a: Inference of cirrus cloud properties using satellite -observed visible and infrared radiances. Part I: Parametrization of radiance fields, *JAS*, 50, 1279-1304.
- Minnis P., P.W. Heck and D.F. Young, 1993b: Inference of cirrus cloud properties using satellite-observed visible and infrared radiances. Part II: Verification of theoretical cirrus radiative properties, *J. Atmos. Sci.*, 50, 1305-1322.
- Minnis P., 1991: Inference of cloud properties from satellite-observed visible and infrared radiances. Thesis. Univ. Of Utah.
- Minnis P. and E.F. Harrison, 1984c: Diurnal variability of regional cloud and clear sky radiative parameters derived from GOES data. Part III: November 1978 radiative parameters. *J. Climate Appl. Meteor.*, 23, 1032-1051.
- Minnis P. and E.F. Harrison, 1984a: Diurnal variability of regional cloud and clear sky radiative parameters derived from GOES data. Part I: Analysis method, *J. Climate Appl. Meteor.*, 23, 993-1011.
- Minnis P. and E.F. Harrison, 1984b: Diurnal variability of regional cloud and clear sky radiative parameters derived from GOES data. Part II: November 1978 cloud distributions, *J. Climate Appl. Meteor.*, 23, 1012-1031.
- Mischenko, M.I., J.W. Hovenier and L.D. Travis (editors), 2000: Light scattering by nonspherical particles. Academic Press, San Diego.

- Moene A., 1998: Personal communication.
- Moulin, C., C.E. Lambert, J. Poitou and F. Dulac, 1996: Long term (1983-1994) calibration of the Meteosat solar (VIS) channel using desert and ocean targets. *Int. J. Rem. Sens.*, 17, 6, 1183-1200.
- Nakajima, T. and M.D. King, 1990: Determination of the optical thickness and effective particle radius of clouds from reflected solar radiation measurements: I Theory. *J. Atmos. Sci.*, 47 (15), 1878-1893.
- Olesen, F.S. and H. Grassl, 1985: Cloud detection and classification over oceans at night with NOAA-7. *Int. J. Rem. Sens.*, 6, 8, 1435-1444.
- Parol, F., J.C. Buriez, D. Cretel and Y. Fouquart, 1994: Cloud optical thickness retrieval from POLDER measurements during ASTEX. *Atmospheric Sensing and Modeling*, R.P. Santer ed., Proc. SPIE 2311, 90-100.
- Peixoto, J.P. and A.H. Oort, 1992: *The physics of Climate*, American Institute of Physics, N.Y.
- Planet, W.G. (editor), 1988: Data extraction and calibration of TIROS-N/NOAA radiometers. NOAA Techn.Mem NESS 107.
- Price, J.C., 1991: Timing of NOAA afternoon passes. *Int. J. Rem. Sens.*, 12, 193-195.
- Pruppacher, H.R. and J.D.Klett, 1978: *Microphysics of clouds and precipitation*, D. Reichel Publ. Co, Dordrecht, Holland, 714pp.
- Ramanathan, V., R.D. Cess, E.F. Harrison, P. Minnis, B.R. Barkstrom, E. Ahmad and D. Hartmann, 1989: Cloud radiative forcing and climate: Results from the Earth Radiation Budget Experiment. *Science*, 243, 57-63.
- Rao, N.C.R. and J. Chen, 1996: Post launch calibration of the visible and near-infrared channels of the Advanced Very High Resolution Radiometer on the NOAA-14 spacecraft. *Int. J. Rem. Sens.*, 17, 14, 2743-2747.
- Rooij, W.A. de, and C.C.A.H. van der Stap, 1984: Expansion of Mie scattering matrices in generalized spherical functions, *Astron. Astrophys.*, 131, 237-248.
- Rossow, W.B. and R.A. Schiffer, 1999: Advances in understanding clouds from ISCCP. *B.A.M.S.*, 80, 11, 2261-2288.
- Rossow W.B. and L.C. Garder, 1993a: Cloud detection using satellite measurements of infrared and visible radiances for ISCCP, *J. Climate*, 6, 2341-2369.
- Rossow W.B. and L.C. Garder, 1993b: Validation of ISCCP cloud detection, *J. Climate*, 6, 2370-2393.

- Rossow W.B., A.W. Walker and L.C. Garder, 1993c: Comparison of ISCCP and other cloud amounts, *J. Climate*, 6, 2394-2418.
- Rossow W.B. and R.A. Schiffer, 1991: ISCCP cloud data products. *B.A.M.S.*, 72, 2-20.
- Rossow W.B., F. Moshier, E. Kinsella, A. Arking, M. Desbois, E. Harrison, P. Minnis, E. Ruprecht, G. Seze, C. Simmer and E. Smith, 1985: The ISCCP cloud algorithm intercomparison, *J. Climate Appl. Meteor.*, 24, 877-903.
- Salisbury J.W. and D.M. D'Aria, 1992: Emissivity of terrestrial materials in the 8-14 μ m atmospheric window. *Rem. Sens. Environ.*, 42, 83-106.
- Saunders R.W. and K.T. Kriebel, 1988: An improved method for detecting clear sky and cloudy radiances from AVHRR-data, *Int. J. Remote Sensing*, 9, 123-150.
- Saunders, R.W., 1986: An automated scheme for the removal of cloud contamination from AVHRR radiances over western Europe. *Int.J.Remote Sens.*, 7, 867-886.
- Savigny, C. von, O. Funk, U. Platt and K. Pfeilsticker, Radiative smoothing in zenith scattered skylight transmitted through optically thick clouds to the ground, *Geophys. Res. Lett.*, 26, 2949-2952, 1999.
- Schiffer, R.A. and W. B. Rossow, 1983: The International Satellite Cloud Climatology Project (ISCCP): The first project of the World Climate Research Program. *Bull. Amer. Meteor.Soc.*, 64, 779-784.
- Schmetz, J., P. Menzel, C. Velden, X. Wu, L. van de Berg, S. Nieman, C. Hayden, K. Holmlund, 1995: Monthly mean large-scale analyses of upper-tropospheric humidity and wind field divergence derived from three geostationary satellites. *Bull. Amer. Meteor. Soc.*, 76(9), 1578-1584.
- Schmetz J. and L. van de Berg, 1994: Upper tropospheric humidity observations from Meteosat compared with short-term forecast fields. *Geophys. Res. Letters*, 21, 573-576.
- Schreiner A.J., D.A. Unger, W.P. Menzel, G. P. Ellrod, K.I. Strabala and J.L. Pellet, 1993, comparison of ground and satellite observations of cloud cover. *B.A.M.S.*, 74, 1851-1861.
- Seze G. and W.B. Rossow, 1991a: Time-cumulated visible and infrared histograms used as description of surface and cloud variations, *Int. J. Remote Sensing*, 12, 877-920.
- Seze G. and W.B. Rossow, 1991b: Effects of satellite data resolution on measuring the space/time variations of surfaces and clouds, *Int. J. Remote Sensing*, 12, 921-952.
- Simmer C., E. Raschke and E. Ruprecht, 1982: A method for determination of cloud properties from two-dimensional histograms. *Ann. Meteor.*, 18, 130-132.

- Singh S.M., A.P. Cracknell and A. F. G. Fiuza, 1985: The estimation of atmospheric corrections to one-channel (11 μ m) data from the AVHRR; simulation using AVHRR/2. *Int. J. Rem. Sens.*, 6, 927-945.
- Stammes, P. and A.J.M. Piers (Eds.), 1996: GOME validation at KNMI and collaborating institutes, KNMI Scientific Report WR 96-08, De Bilt
- Stammes, P., 1994: Errors in UV reflectivity and albedo calculations due to neglecting polarisation. *SPIE*, 2311, 227-235.
- Stammes, P., A. Feijt, A. van Lammeren and G. Prangsma, 1994: TEBEX observations of clouds and radiation - potential and limitations. KNMI TR-162, KNMI, De Bilt.
- Stephens, G.L., 1984: The parametrization of radiation for numerical weather prediction and climate models., *Mon. Weath. Rev.*, 112, 826-866.
- Stephens G.L., 1978: Radiation profiles in extended water clouds. Part II: Parametrization schemes. *J.A.S.*, 35, 2123-2132.
- Stull, R.B.: An introduction to Boundary Layer Meteorology. Kluwer, 666 pp., 1988.
- Suttles et al., 1989: Angular radiation models for the Earth-atmosphere system. Vol I: Shortwave radiation. NASA Ref. Publ. RP-1184, Vol I, 147 pp.
- Suttles et al., 1988: Angular radiation models for the Earth-atmosphere system. Vol II: Longwave radiation. NASA Ref. Publ. RP-1184, Vol II, 87 pp.
- Taylor V. and L. L. Stowe, 1984a: Atlas of reflectance patterns for uniform earth and cloud Surfaces from Nimbus-7 ERB. *J. Geophys. Res.*, 89, 5345-5363.
- Taylor V. and L. L. Stowe, 1984b: Atlas of reflectance patterns for uniform earthh and cloud Surfaces (NIMBUS-7 61 days). NOAA Tech. Rep. NESDIS 10, 66 pp.
- Valk de P., A. Feijt and Roozkrans H., 1998: Cloud field characterization based on meteosat imagery and NWP model data. Proc. of the 1998 EUMETSAT Meteorological Satellite Data Users'Conference, EUMETSAT, Darmstadt,
- Valk de P, Feijt A. and Roozkrans H.; 1997, The application of NWP data and Meteosat imagery in the retrieval of cloud parameters. Proc. of the EUMETSAT Meteorological Satellite Data Users' Conference, Brussels, Eumetsat, 139-146.
- Veen S. van der, and A. Feijt: Liquid water initialization in a cloud prediction model using Meteosat imagery. Proc. of the 1996 EUMETSAT Meteorological Satellite Data Users'Conference, EUMETSAT, Darmstadt, 257-264.
- WCRP, 1988: International Satellite cloud Climatology Project (ISCCP) - Documentation of cloud

- WMO, 1996: Guide to meteorological instruments and methods of observations. WMO 8, WMO Geneve.
- WMO, 1989: Guide on the global observing system. WMO 488, WMO, Geneve.
- Weare, B. A., 1992: A comparison of ISCCP C1 cloud amounts with those derived from high resolution AVHRR images. *Int. J. Rem. Sens.*, 13, 11, 1965-1980.
- Wielicki, B.A., B.R. Barkstrom, E.F. Harrison, R.B. Lee III, G.L. Smith and J.E. Cooper, 1996: Clouds and the Earth's Radiant Energy System (CERES); An Earth observing system experiment. *Bull. Am. Meteorol. Soc.*, 77853-77868.
- Wielicki B.A. and L. Parker, 1992: On the determination of cloud cover from satellite sensors: The effect of sensor spatial resolution, *J. Geophys. Res.*, 97, D12, 12799-12823.
- WMO; 1996, Guide to meteorological instruments and methods of observations, WMO 8, WMO, Geneve.
- Wielicki B. and R. Green, 1989: Cloud identification for ERBE radiative flux retrieval. *J. Appl. Meteorol.*, 28, 1133-1146.
- Winker, D.M., R.M. Couch and M.P. McCormick, 1996: An overview of LITE: NASA's lidar in-space technology experiment. *Proc. IEEE*, 84, 164-180.
- Woick H., J. Schmetz and S. Tjemkes: An introduction to Meteosat Second Generation imagery and products. *Proc. of the 1997 EUMETSAT Meteorological Satellite Data Users'Conference*, Brussels, EUMETSAT, Darmstadt, 395-400.
- World Climate Program, 1988: International Satellite Cloud Climatology Project (ISCCP) documentation of cloud data. WMO/TD-No. 266, 76 pp.
- <http://edcwww.cr.usgs.gov/landdaac/gtopo30/gtopo30.html>, EROS data center, Sioux Falls, SD

Acronyms

APOLLO	AVHRR Processing over Land Cloud and Ocean
ATSR	Along Track Scanning Radiometer
AVHRR	Advanced Very High Resolution Radiometer
BCRS	Beleidscommissie Remote Sensing
CDS	Cloud Detection Sysytem
CERES	Clouds and the Earth's Radiant Energy System
CLARA	Clouds and Radiation
CLIWA-NET	Cloud Water Network
DAK	Doubling Adding KNMI
ECMWF	European Center for Midrange Weather Forecasting (ECMWF)
ERBE	Earth Radiation Budget Experiment
ERS	Earth Remote Sensing
EUMETSAT	Europe's Meteorological Satellite Organisation,
GOME	Global Ozone Monitoring Experiment
GPS	Global Positioning System
HIRLAM	High Resolution Limited Area Model
IFOV	Instantaneous Field of View
IPCC	International Panel on Climate Change
IR	Infra-red
ISCCP	International Satellite Cloud Clkimatology Project
KLAROS	KNMI Local implementation of APOLLO Retrievals in an Operational System
KNMI	Koninklijk Nederlands Meteorologisch Instituut
LITE	Lidar in Space Technology Experiment
LOWTRAN	Low resolution transmissittance
LST	Local Solar Time
LW	Long wave
LWP	Liquid Water Path
MLS	Mid Lattitude Summer
MSG	Meteosat Second Generation
Metclock	Meteosat Cloud Detection and Characterization KNMI
Meteosat	Meteorological Satellite

Modtran	Moderate resolution transmissittance
NESDIS	National Environmental Satellite Data, and Information Service
NOAA	National Oceanic and Atmospheric Administration
NWP	Numerical Weather Prediction Model
POLDER	Polarization and directionality of the Earth's reflectances
SW	Short wave
SZA	Solar Zenith Angle
TEBEX	Tropospheric Energy Budget Experiment, TEBEX
TOA	Top of the Atmosphere
UTC	Universal Time Coordinated
VIS	Visible
VZA	Viewing Zenith Angle
WCP	World Climate Program
WCRP	World Climate Research Program
WMO	World Meteorological Organization
WV	Water-Vapor

List of journal papers and selected reports

- Bloemink, H.I., A.C.A.P. van Lammeren, A.J. Feijt and S. Jongen, 2000: Active passive sensor synergy for cloud observation; IR cloud properties and cloud liquid water. *J.Geophys.Res.* (submitted).
- Boers R, A. Van Lammeren and A. Feijt, 2000: Accuracy of cloud optical depth retrievals from ground based pyronometers. *J. of Atmos. and Ocean. Techn.* (accepted).
- Bonapart, M., A. Bos, F. Debie and A. Feijt, 1994: Cloud classification in Meteosat data using an artificial Neural Network. BSO techn.rep 1702394, BSO, Nieuwegein
- Feijt A., D. Jolivet, S. Dewitte, N. Clerbaux and A. Ipe, 2000: The ERM passive instrument synergy study, ESA Techn. Rep., ESA, Noordwijk.
- Feijt A.J. and H. Jonker, 2000: Comparison of scaling parameters of cloud properties from spatial and temporal distributions, *J.Geophys.Res.* (accepted)
- Feijt, A. and P. de Valk, 2000: The use of NWP surface temperatures in cloud detection from satellite. *Int. J. Remote Sensing* (accepted)
- Feijt A., P. de Valk and S. van der Veen, 2000: Cloud detection using Meteosat imagery and numerical weather prediction model data. *J. Applied. Met.*, Vol. 39, No. 7, 1017-1030.
- Feijt, A., H. ten Brink, S. Jongen, and A. van Lammeren, 1999: Validation of satellite cloud parameter retrieval methods with objective ground based measurements. *Phys. and Chem. of the Earth*, 24, 173-176, 1999.
- Feijt, A. and P. de Valk, 1998: Quantifying the difference between NWP surface temperatures and cloud free satellite apparent brightness temperatures. *Contrib. Atmos. Phys.* , 71, 455-460
- Feijt, A.J. and A.C.A.P. van Lammeren, 1996: Ground-based and satellite observations of Cloud fields in the Netherlands. *Monthly Weather Review*. 124, 9: 1914-1923.
- Feijt A.J. and W. Kohsiek , 1995: The effect of emissivity variations on surface temperature determined by infrared radiometry, *B.L.M.*, 72, 322-327.
- Feijt, A.J., 1992.: The Earth Radiation Budget: overview of data-processing and error sources. *KNMI TR-146*.
- Hanssen, R., A. Feijt, and R. Klees, 2000: Comparison of water vapor column derived from radar interferometry and Meteosat WV channel analysis. *J. of Atmos. and Ocean. Techn.* (accepted).

- Lammeren, A.C.A.P. van, A.J. Feijt, J.A. Konings, E. van Meijgaard en A.P. van Ulden, 2000: Combination of ground based and satellite cloud observations on a routine bases. *Contrib. Atmos. Phys.* (accepted).
- Lammeren, A.C.A.P. van, and A.J. Feijt, 1997: The emissivity of Cirrus clouds derived from LITE and Meteosat measurements. *Selected Papers of the 18th International Laser Radar Conference (ILRC)*, Berlin 22-26 July 1996, published by Springer Verlag New York-Berlin-Heidelberg (ISDN 3-540-61887-2) pp. 201-204.
- Meijgaard, E. van, J.A. Konings, A.J. Feijt en A.C.A.P. van Lammeren, 2000: Comparison of model predicted cloud cover profiles with observations from ground and satellite. *Contrib. Atmos. Phys.* (accepted).
- Veen, S.H. van der and A.J. Feijt, 1996. Liquid water initialization in a cloud prediction model using Meteosat imagery. *Proceedings of the Meteosat Data Users' Meeting*, Vienna, EUMETSAT, Darmstadt

(Co-)author of another 35 papers.

Summary

This thesis is about observations of clouds from satellite and ground based instruments. The aim is to reconstruct the three dimensional cloud distributions. This information is used both in climate research and operational meteorological applications. In climate research, cloud observations provide a reference to atmospheric models, which enables optimization of cloud parameterizations. For operational meteorologists clouds are symptoms of atmospheric conditions. Cloud observations therefore are helpful in understanding the current weather (nowcasting) and improving the estimates of how of the atmospheric conditions will evolve (forecasting).

In order to obtain cloud field characteristics, analysis environments were developed for the interpretation of meteorological satellite measurements in terms of cloud properties. A large effort was put in the evaluation of the results with synoptic observations and measurements from two measurement campaigns. As a result this thesis is composed of three major research topics: Meteosat analysis, AVHRR analysis and combined analysis of ground and satellite observations.

Meteosat analysis

A new cloud detection scheme was developed that includes the use of the surface temperature fields of a Numerical Weather Prediction (NWP) model as a threshold value to distinguish cloudy and cloud free areas. It is shown that also for cloud free conditions, the equivalent black body temperature as measured from satellite is different from the model surface temperature. An innovative part of the scheme is the quantification of this temperature difference, which is used to improve the skill of the cloud detection method. The improvement of the detection efficiency was quantified over land and ocean for 1997 on a 3 hourly basis in a semi-operational setting. As the method optimizes the use of the infrared information it is relatively insensitive to changes of insolation conditions with time of day, location, or season.

AVHRR analysis

The NWP model surface temperatures are also used in the AVHRR analysis environment. For the interpretation of the $0.6\mu\text{m}$ channel reflectivities, extensive radiative transfer calculations

were done with the Doubling-Adding KNMI (DAK) radiative transfer code. The results were put in Look-up tables (LUT). The LUTs are used to obtain the following cloud field properties: cloud cover fraction, cloud top temperature, optical thickness and liquid water path. In order to assess the quality, the retrieved properties were compared to measurements from two campaigns: the Tropospheric Budget Experiment, TEBEX, and the Clouds and Radiation intensive measurement campaigns, CLARA. The comparison shows that the retrieval algorithms yield results that agree with independent ground based measurements for the cases studied.

Combined analysis of satellite and ground observations

Combined analysis of satellite and ground based observations from the TEBEX and CLARA data sets yields information on the quality of the satellite retrieval, but also on the merits of the ground based remote sensing instruments. The study shows that both observational sets have strong points, but a combination is preferred to obtain a good definition of the cloud field. In all comparisons the problem of collocation occurs. The ground based instruments measure continuously in time at one location, while satellites measure a spatial distribution at one moment in time. When comparing ground and satellite derived cloud products it is always questionable which part of the time series corresponds to which part of the spatial distribution. This correlation is studied by comparing variance spectra of time series and spatial distributions of liquid water path derived from microwave radiometer and AVHRR data respectively. It is shown that for two cases with different scaling properties the variance spectrum is similar for a part of the time-series and for a part of the AVHRR image.

This thesis contributes to quantitative use of meteorological satellite data in meteorology and climate research. Furthermore, it advances combined analysis of space-borne and ground based remote sensing measurements of clouds for routine applications.

Samenvatting

Dit proefschrift betreft wolkenwaarnemingen vanaf meteorologische satellieten en vanaf de grond. Het doel van het onderzoek is om met een combinatie van deze metingen de driedimensionale verdeling van wolken te reconstrueren. Toepassingsgebieden zijn het klimaatonderzoek en de operationele meteorologie. In het klimaatonderzoek wordt gebruik gemaakt van atmosfeermodellen, waarin de bewolking gebrekkig beschreven is. De wolkenwaarnemingen kunnen dienen als referentie ter verbetering van de wolkenparametrizaties. Wolken zijn onderdeel van atmosferische processen. Aan de soort bewolking en de structuur van wolkenvelden kan de meteoroloog deze atmosferische processen herkennen. Wolkenwaarnemingen dragen daarom bij aan het begrijpen van het huidige weer (nowcasting) en daarmee kan beter worden ingeschat hoe de atmosferische omstandigheden zich zullen ontwikkelen (weersverwachting).

Gedurende het onderzoek zijn er analyse-methoden ontwikkeld voor de interpretatie van metingen van meteorologische satellieten in termen van wolkenkarakteristieken. Er is veel aandacht besteed aan de vergelijking van de resultaten met de synops rapporten van menselijke waarnemers en de meetgegevens van twee meetcampagnes. Het proefschrift bestaat uit drie onderzoeksonderwerpen: Meteosat analyse, AVHRR analyse en gecombineerde analyse van grond en satellietwaarnemingen.

Meteosat analyse

Een nieuw wolkendetectie schema is ontwikkeld dat de oppervlakte-temperaturen van een weermodel gebruikt als drempelwaarde om bewolkte en onbewolkte gebieden te onderscheiden. Uit het onderzoek blijkt, dat de model oppervlakte temperaturen niet direct toegepast kunnen worden. De model oppervlakte-temperaturen verschillen namelijk ook in wolkenvrije situaties van de door de satelliet gemeten temperatuur. Dit temperatuurverschil is gekwantificeerd. Een innovatief onderdeel van het detectie-schema is, dat dit gegeven gebruikt wordt om de drempelwaarde aan te passen en daarmee de kwaliteit van de wolkendetectiemethode te verbeteren. De detectie-efficiëntie is voor land en zeeoppervlak iedere 3 uur voor geheel 1997 bepaald op semi-operationele basis. De methode is relatief ongevoelig voor verandering in zonne-instraling met tijd van de dag, geografische plaats of seizoen.

AVHRR analyse

De oppervlakte temperaturen van het weermodel worden ook gebruikt in de analyse van AVHRR metingen. Om het gemeten gereflecteerde zonlicht in het 0.6 μ m kanaal te kunnen interpreteren zijn uitgebreide stralingstransportberekeningen gedaan met de Doubling-Adding KNMI (DAK) stralingstransportcode. De resultaten zijn in zoektabellen geplaatst. Deze tabellen worden gebruikt om de volgende wolkenveld eigenschappen te bepalen: bedekkingsgraad, top temperatuur, optische dikte en vloeibaar water pad. De kwaliteit van de methode is bepaald door vergelijking van de afgeleide wolkeneigenschappen met metingen van twee meetcampagnes: het "Tropospheric Energy Budget Experiment" (TEBEX) en de "Clouds and Radiation Intensive Observational Campaign" (CLARA). De vergelijking laat zien dat, voor de bestudeerde gevallen, de methoden resultaten opleveren die in overeenstemming zijn met onafhankelijke grondwaarnemingen.

Gecombineerde analyse van satelliet en grondmetingen

De vergelijking van satelliet- en grondmetingen van TEBEX en CLARA levert informatie over de kwaliteit van de waarnemingen vanuit de satelliet en vanaf de grond. Uit het onderzoek blijkt dat beide soorten waarnemingen hun sterke kanten hebben, maar een combinatie de voorkeur verdient om wolkenvelden te definiëren. Echter, in alle vergelijkingen doet zich het probleem van collocatie voor: de grond- en satellietinstrumenten bemeten niet precies hetzelfde wolkenvolume. De grondinstrumenten meten doorlopend in de tijd op één plaats, terwijl satellieten een ruimtelijke verdeling meten op één moment in de tijd (instantaan). Bij de vergelijking van grond- en satellietwaarnemingen is het altijd de vraag, welk deel van de tijdreeks hoort bij welk deel van de ruimtelijke verdeling. Deze correlatie is onderzocht met behulp van variantie-spectra van vloeibaar water. Tijdreeksen van vloeibaar water zijn afgeleid uit metingen van een microgolf radiometer. Ruimtelijke verdelingen zijn afgeleid uit metingen van de AVHRR. Voor twee gevallen van wolkenvelden met verschillend schalingsgedrag wordt aangetoond dat het variantie-spectrum van een deel van de tijdreeks en een deel van het AVHRR beeld overeenkomen.

Dit proefschrift draagt bij aan het kwantitatieve gebruik van meteorologische satellieten in de meteorologie en het klimaatonderzoek. Tevens bevordert het de gecombineerde analyse van satelliet- en grondmetingen voor routine-toepassingen.

Curriculum Vitae

Arnout Feijt is geboren op 9 mei 1959 te Rotterdam. Hij volgde zijn middelbare school opleiding aan de Wolfert van Borselen openbare scholengemeenschap, waar hij in 1978 . het Atheneum diploma behaalde. Hierna volgde hij de kandidaatsopleiding Natuurkunde met bijvak Sociologie aan de Rijksuniversiteit Utrecht. In 1985 studeerde hij af in de experimentele Natuurkunde met bijvakken Thermodynamica en Milieukunde. Het klein onderzoek betrof meetmethoden aan aerosolen en werd uitgevoerd bij het Energie Centrum Nederland. Het grootonderzoek vond plaats bij de vakgroep Medische Fysica en betrof het kleuronderscheidendvermogen van de perifere retina.

Na de studie werkte hij korte tijd bij Ecofys u.a. te Utrecht aan het ontwerp van een meetinstrument voor kolenstof. Ecofys u.a. adviseert en initieert projecten op het gebied van duurzame energievoorziening.

Daarna volgde een 3 jarig werkverband met Developmental Technologies b.v. te Kerkrade. Developmental Technologies b.v. beoogde de ontwikkeling van nieuwe productieprocessen voor high-technology producenten zoals de vliegtuigindustrie. In deze tijd heeft hij onder andere ervaring opgedaan met grafische interfaces, structured programming, Finite Element Analysis, robot aansturingen, neurale netwerken, fractals en non-destructive testing methoden.

Na de geboorte van zijn eerste kind, Mark, verhuisde hij naar de provincie Utrecht. Waar hij 3 jaar heeft gewerkt als systeemontwerper bij softwarehouse Turnkiek b.v. te Amersfoort. Als gedetacheerd technisch automatiseerder heeft hij veel geleerd over het financieel en technisch plannen van projecten en van de methoden en technieken die bij de verschillende bedrijven gebruikt werden.

Na de geboorte van een tweeling, Luuk en Milou, in april 1991 keerde hij terug naar de natuurkunde in een tijdelijke functie als wetenschappelijk onderzoeker bij het KNMI. Het onderzoek betrof de evaluatie van twee veel gebruikte klimaat meetsets afkomstig van: de Earth Radiation Budget Experiment (ERBE) en het International Satellite Cloud Climatology Project (ISCCP). Beide meetsets komen voort uit satellietmetingen. In de loop van de jaren heeft hij programmatuur geschreven voor kwantitatieve verwerking en analyse van Meteosat en AVHRR metingen. De automatiseringservaring kwam daarbij goed van pas. Deze verwerkingsomgevingen zijn gebruikt als basis voor onderzoek. Het KNMI heeft veel ruimte gegeven voor de bestudering van atmosferische processen en de theorie van atmosferisch stralingstransport. In 1996 was hij technisch coordinator van de Clouds and Radiation

(CLARA) meetcampagnes en werd het tijdelijk dienstverband omgezet in een vaste baan. Daarna kon meer aandacht besteed worden aan het schrijven van publikaties. Tevens werd het mogelijk projectvoorstellen te doen bij externe financiers, waarvan er tot op heden 4 zijn gehonoreerd. De afgelopen 3 jaar is hij gelouterd door de combinatie van het projectleiderschap van deze projecten, het ouderschap en het schrijven van wetenschappelijke artikelen. Eind 1999 waren er genoeg publicaties om een proefschrift te rechtvaardigen. Het resultaat ligt nu voor u.